RELIABILITY AND SENSITIVITY ANALYSIS OF CIVIL AND MARINE STRUCTURES USING MACHINE-LEARNING-ASSISTED SIMULATION

By

MOHAMMAD FIRAS TAMIMI
Bachelor of Science in Civil Engineering
Yarmouk University
Irbid, Jordan
2016

Master of Science in Civil Engineering
Jordan University of Science and Technology
Irbid, Jordan
2018

Submitted to the Faculty of the
Graduate College of the
Oklahoma State University
in partial fulfillment of
the requirements for
the Degree of
DOCTOR OF PHILOSOPHY
December, 2022

RELIABILITY AND SENSITIVITY ANALYSIS OF

CIVIL AND MARINE STRUCTURES USING

MACHINE-LEARNING-ASSISTED SIMULATION

Dissertation Approved:

Dr. Mohamed Soliman

Dissertation Adviser

Dr. Bruce W. Russell

Dr. Robert N. Emerson

Dr. Sabit Ekin

ACKNOWLEDGEMENTS

This endeavor would not have been possible without the help and encouragement from many great people that I would like to take this opportunity to acknowledge their help and support. First and foremost, I am deeply indebted to my advisor, Dr. Mohamed Soliman for his unwavering support and belief in me, whose tireless efforts in supporting my career goals have forever changed how I see the world. I would not be where I am today if not for his enormous passion, energy, and time he spent helping me through my Ph.D. journey. I would also like to extend my deepest gratitude to my committee members, Dr. Bruce Russell, Dr. Robert Emerson, and Dr. Sabit Ekin, not only because of providing invaluable feedback and insight but also for their constant encouragement and profound belief in my work. I gratefully acknowledge the support of scholarship and grants from (a) Yarmouk University -Jordan, (b) Office of Naval Research (ONR), (c) American Institute of Steel Structures (AISC), and (d) School of Civil and Environmental Engineering of Oklahoma State University.

I am thankful to many colleagues who I have had the pleasure of working with over the course of these years. I would like to thank Dr. Omid Khandel, Christopher Waite, Dr. Leon Shen, Imran Ahmad, Ethan Stinger, Cody James, Aws Idris, Alaaeldin Soliman, and Aditya Nayak. I would be amiss if I did not thank my friends who never let me down and always nurtured me throughout my endeavors. I am blessed to have great friends all over

the world, and luckily, I got to know many amazing people here in Stillwater with whom we spent a wonderful time and shared special moments and memories that I will always keep in my heart and mind.

Finally, yet importantly, my warm and heartfelt thanks go to my family for their unconditional love and tremendous support and the hope and confidence they have constantly given me. To my dearest parents, Dr. Firas and Entesar, who have stood by me and supported my decisions creating an environment for pursuing my dreams. To my grandmothers, thank you for your sacrifices, your love, and everything that you have done for me. Also, to my loving brothers and sister, Loai, Rami, Samer, Ammar, and Shreen, for their love and support over the years and for being a great source of encouragement helping me sail through all the challenges.

Name: MOHAMMAD FIRAS TAMIMI

Date of Degree: DECEMBER 2022

Title of Study: RELIABILITY AND SENSITIVITY ANALYSIS OF CIVIL AND MARINE STRUCTURES USING MACHINE-LEARNING-ASSISTED SIMULATION

Major Field: CIVIL ENGINEERING

Abstract: Civil and marine structures are subjected to various deterioration mechanisms due to aggressive environmental effects or mechanical loads. In order to maintain an acceptable performance level of these structures, previous research have focused on developing methodologies to quantify their reliability and provide optimized management plans that can reduce the life-cycle cost and failure risk. However, the successful implementation of these methodologies is contingent upon the ability to consider various uncertainties associated with structural performance. These include uncertainties associated with environmental and human-induced stressors, as well as those affecting material and geometrical characterization as well as performance prediction models. Monte Carlo simulation (MCS) with a sufficient number of samples can provide accurate quantification of the structural performance under uncertainty. However, for complex problems that require detailed finite element (FE) modeling to predict the system performance, the computational cost can be very high. This problem can be addressed by using advanced sampling techniques that can provide an accurate estimation of the reliability with a significantly lower number of samples. Another approach is to use surrogate models to establish an accurate approximation of the complex system behavior. These models can provide statistically equivalent results of a complex simulation model, with no known closed-form solution, through a limited number of original model executions.

The proposed research focuses on developing probabilistic approaches for the performance assessment of civil and marine structures using machine-learning-assisted MCS. In this approach, machine learning is used to generate a surrogate model of the system response and is next integrated into the MCS to quantify the failure probability of the structure. Sensitivity analysis is conducted to identify the key contributing variables that significantly affect the system response. This process helps reduce the number of random variables associated with the problem resulting in a more efficient probabilistic simulation process. The developed approach was applied to solve two major research problems in civil and marine engineering: (a) reliability quantification of eccentrically loaded steel connections employing both welds and bolts for force transfer and (b) characterizing the crack propagation in stiffened panels and quantifying the reliability of ship hulls under realistic loading conditions.

TABLE OF CONTENTS

Chapter Page

LIST OF TABLES

Table Page

.

LIST OF FIGURES

Figure Page

CHAPTER I

INTRODUCTION

1.1. Introduction

Civil and marine structures are subjected to various mechanical and environmental stressors throughout their service life. Some of these stressors may induce sudden strength failure (e.g., yielding or buckling), while others can cause gradual deterioration (e.g., fatigue and corrosion). As a result, it is essential to develop proper assessment techniques that can help to restore or strengthen structural resistance to extreme or progressive events, as well as extend the service life of deteriorating structures. Despite the long history of research to understand the behavior of steel components in civil and maritime constructions, many knowledge gaps still exist. The research conducted herein integrates experimental test findings, FE modeling, sensitivity analysis, surrogate modeling, and probabilistic approaches to address two of these knowledge gaps: (a) quantifying the behavior and reliability of eccentrically loaded steel connections made with bolts and welds in combination and (b) characterizing the crack propagation behavior in stiffened panels and quantifying the reliability of ship hulls under realistic loading conditions.

Eccentrically loaded connections are commonly used in steel construction to transfer loads between structural elements in steel buildings and bridges. Examples of these connections include bracket-type connections and web splices in beams and girders. Combining welds

and bolts may be an appealing practical solution to improve the capacity of an existing steel connection. In many situations, it may be desirable to add welds to a bolted connection to resolve construction errors or to retrofit existing connections. Despite the long history of research on the behavior of steel connections made with bolts and welds in combination, the review of available literature indicates that the behavior of eccentrically loaded connections made by combining fillet welds and high-strength pretensioned bolts is still limited to few studies. Furthermore, the reliability of combinational connections was never investigated in the literature. This research addresses these needs by using experimental testing results and numerical analysis to develop a deeper understanding of the behavior of eccentrically loaded connections made with high-strength pretensioned bolts and longitudinal fillet welds. Numerical models are established and used to characterize the load transfer mechanisms within these combination connections. The numerical analysis assisted in investigating the load-carrying capacity and the load sharing between the bolts and welds in the single load resisting system. The dissertation also investigates the probabilistic behavior of these connections by integrating the FE models, machine learning, and MCS. The reliability of the connections is quantified, and a calibration process is conducted to establish the resistance factors necessary to maintain the reliability level above prescribed thresholds.

The fatigue crack propagation behavior in stiffened ship hulls under realistic loading conditions has been investigated in the second part of this dissertation. Fatigue cracking has been recognized as one of the main deterioration mechanisms that can affect the safety of ship structures. The ships are generally exposed to millions of load cycles during their service life. This large number of load cycles can lead to fatigue crack

propagation which may cause a drop in structural reliability. Most of the fatigue crack growth results available in the literature have been obtained through tests performed under constant amplitude loading. However, marine structures, such as ships and offshore structures, experience wave conditions that result in variable amplitude load cycles (VAL). This can lead to fatigue crack growth acceleration or retardation, which interacts and affect the fatigue causing significant changes in the crack growth behavior and subsequently fatigue service life. Therefore, a comprehensive evaluation of the effect of variable amplitude loading on the crack propagation is necessary to ensure an acceptable level of safety of ships throughout their service life. Although numerous studies have been reported on the fatigue behavior of steel structures under constant amplitude loading, there is a very limited understanding of the crack growth behavior in ships under realistic sea loading conditions.

Moreover, the variable amplitude loads induced by the waves are among the stressors that are significantly affected by sea conditions. A comparison of recent climate trends to average historical conditions has shown considerable differences in various wave parameters and storm characteristics in different locations around the world. Despite the significant effort in literature aiming at quantifying the effects of climate change on wave characteristics, to the best of the author' knowledge, none of the available studies quantified the effect of climate change on the fatigue crack propagation in ship hulls under uncertainty. Such quantification is essential to develop effective long-term life-cycle management procedures capable of maintaining the reliability of the ships above acceptable thresholds. This dissertation presents an innovative simulation-based framework for predicting the fatigue crack propagation in ship hulls in light of climate

change. The dissertation also discusses the impact of climate change on wave parameters and storm characteristics across the Atlantic Ocean and principal shipping routes. A numerical model for a ship hull is established and used to extract essential parameters used to model crack propagation under variable sea loading. An analytical crack advancement rule is used in conjunction with the numerical analysis to quantify the crack propagation characteristics.

The third part of the dissertation is dedicated to quantifying the influence of various sources of uncertainty, including those associated with mechanical properties and geometric parameters, on the fatigue service life of welded stiffened panels. Predicting the fatigue service life of marine structures is affected by significant uncertainties arising from randomness in loading conditions and environmental factors. In addition, the variability in material and geometrical properties, and the presence of residual stresses add to the challenges associated with the service life prediction. Therefore, the accurate quantification of uncertainties associated with these parameters and their effect on the behavior is crucial for the accurate prediction of the fatigue service life and for ensuring structural integrity and operational reliability throughout the service life. This dissertation addresses these needs and quantifies the influence of relevant input parameters, covering geometric and mechanical properties, on the crack propagation behavior and fatigue service life of welded stiffened panels.

A similar research routine has been applied for evaluating the reliability of ships subjected to aggressive environmental conditions under growing crack. Traditional approaches for reliability assessment of ship hulls under propagating cracks mostly rely on comparing the value of a certain fracture mechanics parameter calculated at the crack tip

to the fracture toughness of the material. This assumption may not accurately represent the failure event since the fracture resistance is not only affected by the material properties but also by the component geometry. Furthermore, this approach may not properly account for the possibility of elastic-plastic fracture in the ship hull. This dissertation addresses these needs and proposes a novel approach for quantifying the fatigue reliability of stiffened ship hull under propagating fatigue crack utilizing the failure assessment diagrams (FAD) to define the performance function of the hull. The proposed performance function considers realistic loading conditions, the occurrence probability of relevant failure modes, and the resistance of the hull girder to sudden fracture. MCS is used to quantify the failure probability and reliability index of the ship hull under realistic conditions. This dissertation discusses available literature, provides solutions, and presents results related to the identified knowledge gaps under the following chapters:

Chapter 2. Investigating the Behavior and Reliability of Eccentrically Loaded Steel Connections Made with Bolts and Welds in Combination

Chapter 3. Quantifying Fatigue Deterioration of Ship Structures Under Changing Climate Conditions

Chapter 4. Sensitivity Assessment of the Crack Propagation Behavior in Welded Stiffened Panels

Chapter 5. Comprehensive Quantification of the Reliability of Ship Hulls Under Propagating Fatigue Cracks

Chapter 6. Conclusions and Recommendations for Future Work

1.2. Research Objectives

The overall objective of this research is to establish a probabilistic framework for the performance assessment of civil and marine structures using machine-learning-assisted MCSs. This framework is utilized to:

(a) Evaluate the behavior and reliability of welded-bolted combination connections under eccentric loading conditions.

(b) Investigate the fatigue crack growth behavior in ship hulls under realistic random sea loading where the stress and the stress ratio (positive or negative) may vary from cycle to cycle.

(c) Quantify the long-term effects of climate change on the fatigue crack propagation in ship hulls

(d) Evaluate the influence of relevant input parameters, covering geometric and mechanical properties, on the crack propagation behavior and fatigue service life of welded stiffened panels.

(e) Quantify the reliability of ship hull structures under propagating fatigue cracks while accounting for realistic loading conditions, the occurrence probability of relevant failure modes, and the resistance of the hull girder to sudden fracture.

1.3. Technical Contributions of the Research

- Quantifying the reliability of bolted-welded combination connections under eccentric loading is considered a main contribution of this research. This study provides an in-depth characterization of the behavior of eccentrically loaded steel connections combining fillet welds and high-strength pretensioned bolts. It develops, for the first time in literature, a new analytical load-deformation model

to describe the evolution of the force with respect to deformation for slip-resistant connections. This model allows the proper quantification of the force carried by the connections and improves the design process of bolted-only or combination connections under eccentric loads. The study also represents the first effort in literature to analytically predict the capacity of eccentrically loaded combination connections when connecting elements are considered as a part of a single load resisting system. Finally, the dissertation quantifies the reliability of these connections and provides the appropriate resistance factors to be employed for the design process.

- Developing an innovative simulation-based framework to quantify the crack prorogation characteristics under realistic sea conditions is the second contribution. This framework accounts for future changes in the wave parameters and storm characteristics due to climate variability and evaluates their effect on crack propagation. The results of this process have been published in Tamimi et al. (2022).
- The third contribution of this research is quantifying the influence of various sources of uncertainty, including those associated with mechanical properties and geometric parameters, on the crack propagation behavior and fatigue reliability of welded stiffened panels. The available sensitivity and reliability analysis in literature considered the uncertainty associated with the loads, mechanical properties, and residual stresses. However, less focus has been placed on integrating the uncertainties associated with the geometric parameters in the probabilistic crack propagation prediction process and fatigue reliability quantification. On the

contrary, this dissertation conducts a sensitivity analysis to evaluate the effect of relevant input parameters, covering geometric and mechanical properties, on crack propagation behavior. Furthermore, the effect of the geometric uncertainties on the fatigue reliability of these panels is also quantified.

- The final contribution of this research is establishing a comprehensive approach for quantifying the reliability of ship hull structures under propagating fatigue cracks. Existing reliability quantification approaches in literature account only for the possibility of brittle fracture failure and may not be valid when considerable plastic deformation may occur. Furthermore, the resistance to sudden fractures is not properly quantified. The proposed reliability quantification approach utilizes the failure assessment diagram to develop a performance function. This performance function enables the assessment of different failure modes ranging from full plastic collapse to brittle fracture. In addition, the proposed approach properly quantifies the fracture resistance of the structure to represent the actual geometry and mechanical characteristics of the hull girder.

CHAPTER II

INVESTIGATING THE BEHAVIOR AND RELIABILITY OF ECCENTRICALLY LOADED STEEL CONNECTIONS MADE WITH BOLTS AND WELDS IN COMBINATION

2.1. Overview

This chapter investigates the behavior of eccentrically loaded connections made by combining fillet welds and high-strength pretensioned bolts. New models are introduced for characterizing the load-deformation behavior of slip-resistant bolted connections with different faying surface conditions. These models are utilized to improve the ability of the instantaneous center of rotation (ICR) method to predict the capacity of eccentrically loaded connections utilizing friction as a load transfer mechanism including bolted-only and/or bolted-welded combination connections. Experimental results are used to quantify the accuracy of the ICR method in predicting the capacity of these combination connections considering different connecting elements to be participating in a single load resisting system. FE analysis is conducted to investigate the load transfer mechanisms within the combination connections. Reliability analysis is conducted using FE analysis assisted by machine learning to quantify the reliability level of the investigated connections and establish the resistance factors necessary to maintain the reliability level above prescribed

thresholds. The reliability analysis shows that using the ICR method for designing these combination connections leads to a highly reliable connection when a resistance factor of 0.75 is used. Higher resistance factors can also be used based on the condition of the faying surface.

2.2. Background

Eccentrically loaded connections are commonly used in steel construction. Examples of these connections include bracket-type connections and web splices in beams and girders (Lue et al., 2017). The load-carrying capacity of bolts group or welds subjected to an eccentric load may be computed by several methods including the elastic method and the instantaneous center of rotation (ICR) method, also referred to as the ultimate strength method (AISC, 2017; Lue et al., 2017). The elastic method assumes perfect elastic conditions and neglects the ductility of individual connecting elements (i.e., bolts and welds) resulting in conservatism in predicting the connection capacity (AISC, 2017; Lue et al., 2017). Although the elastic method is still included in the design specifications, the ICR method provides a more realistic estimate of the ultimate capacity and is considered superior over the elastic method (AISC, 2017).

The current AISC *Steel Construction Manual* (2017), hereafter referred to as the AISC *Manual*, adopts the ICR method to estimate the capacity of bearing-type bolted connections under eccentric loads. This approach assumes that the connection reaches its ultimate capacity when the bolt furthest from the ICR reaches its ultimate deformation. At this stage, the deformation in other bolts is assumed to be proportional to their distance from the ICR. The force in the bolts is computed based on the load-deformation relationship developed in Fisher (1964). Kulak (1975) applied the ICR method to predict

the capacity of eccentrically loaded slip-resistant connections made with high-strength pretensioned bolts. In contrast to the bearing-type connections, each bolt in the slip-resistant connection was assumed in Kulak (1975) to carry the same resistive force independent of its distance from the ICR. This force was considered equal to the slip resistance provided by the bolt. Kulak (1975) indicated that utilizing the ICR method along with the load-deformation model for bearing-type bolted connections provides a highly conservative capacity prediction for eccentrically loaded slip-resistant bolted connections.

Butler et al. (1972) implemented the ICR method to estimate the capacity of eccentrically loaded weld groups and used experimentally derived load-deformation relationships to predict the force in different weld elements. A similar approach has been adopted by the AISC *Manual* (AISC 2017) to compute the capacity of eccentrically loaded weld groups utilizing the load-deformation relationship derived in Lesik & Kennedy (1990) for fillet welds under different loading angles. For many practical situations, it may be desirable to supplement a bolted connection with welds in order to strengthen the connection and increase its ultimate capacity. This may be needed while retrofitting existing structures or resolving construction errors. Despite the history of research on the behavior of steel connections made with bolts and welds in combination (Holtz & Kulak, 1970; Jarosch & Bowman, 1986; Manuel & Kulak, 2000; Shi et al., 2011; Kim & Lee 2020; Khandel et al., 2021; Waite et al., 2022), very few studies investigated the behavior of combination connections that are loaded eccentrically.

In Soliman et al. (2021), the authors conducted an experimental study aiming at investigating the behavior of steel connections combining high-strength pretensioned bolts and welds in a single load-resisting system under eccentric loading. The effect of various

critical variables on the capacity of eccentrically loaded connections was investigated. These variables include bolt pattern, faying surface condition, the ratio between the strength of the welded- and bolted-only connections (referred to later as weld-to-bolt strength ratio), and load eccentricity. The results in Soliman et al. (2021) concluded that the weld attributes (e.g., weld size, length, and location) have a significant effect on the behavior of an eccentrically loaded combination connection. Furthermore, Soliman et al. (2021) showed that the ICR method can be used to predict the capacity of eccentrically loaded combination connections using AISC (2017) formulations and assuming that both connecting elements participate in a single load resisting system; however, this approach still requires significant refinements to improve its accuracy in predicting the connection capacity. In particular, more realistic load-deformation models are needed to properly capture the frictional resistance induced by the pretensioned bolts. Additionally, detailed numerical investigations are needed to investigate the load sharing and transfer mechanisms within these combination connections.

On another front, due to the presence of high variability in the geometrical and mechanical properties of welds and bolts, it is essential to utilize probabilistic approaches to quantify the capacity of these connections under uncertainty. These uncertainties can be found in the friction characteristics of the faying surface, weld dimensions, and mechanical properties of different connecting elements, among others. Although steel connections represent a critical component of steel structures, research aiming at evaluating the reliability of steel connections is still limited. Grondin et al. (2007) evaluated the reliability of slip-resistant bolted connections using experimental data reported in literature. The faying surface condition and the bolt pretension force were considered the main random

variables governing the behavior of these connections. Li (2007) evaluated the reliability of concentrically loaded connections utilizing fillet welds and designed using AISC (2006) formulations. Abbasianjahromi & Shojaeikhah (2021) investigated the reliability of unstiffened extended end-plate connections using MCS assisted by ANNs. Khandel et al. (2022) evaluated the reliability of concentrically loaded steel connections made by combining fillet welds and slip-resistant bolted connections using MCS that integrates FE modeling.

Based on this review, it is apparent that there is a general knowledge gap with respect to the reliability of connections that are loaded eccentrically; this is especially true for connections combining bolts and welds. Such quantification is essential to ensure that the reliability level of these connections is above target thresholds. This chapter provides a comprehensive investigation on the behavior of eccentrically loaded connections made by combining fillet welds and high-strength pretensioned bolts. The ability of the ICR method to predict the capacity of these connections is enhanced through the application of newly developed load-deformation models for the slip resistance introduced by the pretensioned bolts. Numerical models are established and used to characterize the load transfer mechanisms within these combination connections. The numerical analysis assisted in investigating the load-carrying capacity, location of the ICR, and the load sharing between the bolts and welds in the single load resisting system. Finally, the chapter investigates the probabilistic behavior of these connections by integrating the FE models, machine learning, and MCS. The reliability of the connections is quantified, and a calibration process is conducted to establish the resistance factors necessary to maintain the reliability level above prescribed thresholds.

2.3. Predicting the Strength of Eccentrically Loaded Connections: The ICR Model

2.3.1. Bolted Connections

The ICR method can be utilized to predict the capacity of eccentrically loaded, bearing-type bolted connections. Due to the load eccentricity, the force carried by each bolt will be different at the ultimate capacity of the connection. The connection reaches its ultimate strength when the farthest bolt from the ICR reaches its maximum deformation, Δ_{max} (i.e., deformation at fracture of the bolt). At this stage, the deformation of the other bolts is assumed to be proportional to their distance from the ICR. The nominal shear strength of a bolt R_{nb} at deformation Δ is calculated as (Fisher, 1964; Crawford and Kulak, 1971; AISC 2017):

$$R_{nb} = R_{ult}(1.0 - e^{-10\Delta})^{0.55} \tag{2-1}$$

where R_{ult} is the ultimate shear strength of the bolt. Once the load-deformation relationship is established and the connection geometry is defined, an iterative procedure is implemented to find the position of the ICR. At each iteration, the location of the ICR is assumed and the distance between each bolt and the ICR is calculated. The farthest bolt from the ICR is assumed to reach Δ_{max} and the deformation in other bolts varies linearly with their distance from the ICR. The resisting force in each bolt is calculated using Equation (2-1). Static equilibrium between bolt forces and applied load is checked. If equilibrium is not satisfied, another iteration is executed with a new location of the ICR.

Although the load-deformation model in Equation (2-1) was developed for bearing-type bolted connections, the AISC (2017) allows its use to predict the capacity of eccentrically loaded slip-resistant bolted connections. In this case, the value or R_{ult} is replaced by the friction capacity provided by the pretensioned bolt. However, this

assumption may provide a highly conservative estimate of the capacity since the normalized force calculated using the load-deformation of a bearing-type connection is significantly lower than the force calculated using the actual frictional load-deformation behavior of slip-resistant bolted connections at the same deformation level (Soliman et al., 2021). To improve the accuracy of the ICR method in predicting the capacity of slip-resistant connections, it is essential to utilize a load-deformation model that reflects the realistic load-deformation behavior of these connections. Soliman et al. (2021) tested several slip-resistant bolted connections under concentric axial loading and reported their experimental load-deformation behavior. A total of 23 bolted-only connections were tested in Soliman et al. (2021) with different bolt grades (i.e., A325 or A490), pretensioning methods (i.e., turn of nut or tension control), and faying surface conditions (i.e., clean mill scale or blast cleaned surface). Test data from Soliman et al. (2021) is utilized herein to develop a load-deformation model for slip-resistant bolted connections.

The criteria for selecting the analytical best-fit expression are based on satisfying the experimental test data, as well as specific boundary conditions. The following boundary conditions are considered based on the behavior observed during the experimental results; (a) the deformation is equal to zero when the load is zero, (b) an approximately linear relationship between the load and the deformation Δ at small deformation levels, and (c) as Δ approaches Δ_{max}, the load increases with the deformation at a decreasing rate for surfaces with a clean mill scale, whereas a drop in the force occurs for connections with blast-cleaned surfaces. The following expression is selected for faying surfaces with clean mill scale condition (denoted herein as Class A surfaces following the AISC (2017) designation) since it satisfies these conditions and the experimental data

$$R_{nb_A} = R_{ult}(1.0 - e^{-0.62\Delta})^{0.22} \quad (2\text{-}2)$$

where R_{nb_A} is the nominal friction resistance, for Class A faying surface, provided by a single bolt at deformation Δ. A double exponential expression is adopted to describe the relationship between the deformation and normalized load for blast cleaned faying surfaces (denoted herein as Class B surfaces following the AISC (2017) designation) to capture the drop in force that may occur after the initial slip event (see Soliman et al., 2021). This load-deformation relationship is expressed as

$$R_{nb_B} = R_{ult}(1.21(e^{-0.42\Delta} - e^{-11.62\Delta})) \quad (2\text{-}3)$$

where R_{nb_B} is the nominal friction resistance, for Class B faying surfaces, provided by a single bolt at deformation Δ. Figures 1(a) and 1(b) depict the load-deformation behavior derived from the test data for the slip-resistant bolted connections with Class A and B faying surfaces, respectively, and the best-fit curves given by Equations (2-2) and (2-3). The optimum values of parameters of these best-fit expressions were obtained using the NSGA-II genetic algorithms optimization approach (Deb et al., 2002) with the objective function of minimizing the mean squared error between the fit function and the experimental data. The Global Optimization Toolbox of MATLAB (MathWorks, 2020) was utilized to perform the optimization process. The best-fit curves shown in Figure 2-1 (and given by Equations (2-2) and (2-3)) result in a coefficient of determination (R^2) of 0.977 and 0.9855, for Class A and B, respectively.

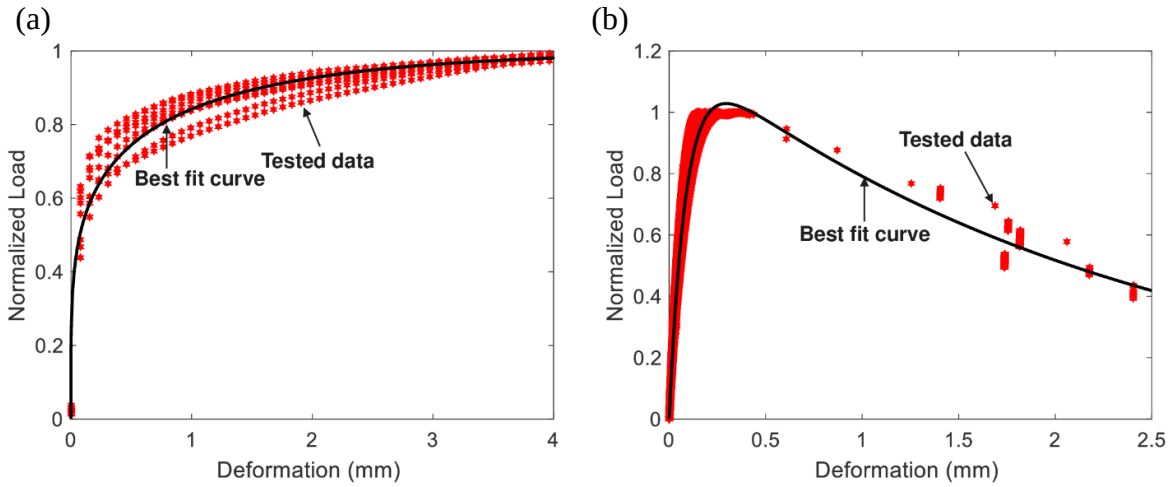

Figure 2-1. The load-deformation behavior of slip-resistant bolted connections utilizing (a) Class A and (b) Class B faying surfaces.

2.3.2. Welded connections

A similar iterative procedure can be used to predict the capacity of welded connections under eccentric loading. In this case, the weld lines are discretized into small elements and the nominal capacity F_{nwi} of the ith weld element subjected to eccentric loading F_{nwi} is calculated using the following load-deformation relationship (AISC, 2017)

$$F_{nwi} = 0.6F_{EXX}(1.0 + 0.5sin^{1.5}\theta_i)[p_i(1.9 - 0.9p_i)]^{0.3} \quad (2\text{-}4)$$

in which F_{Exx} is the weld electrode strength, θ_i is the angle between the direction of applied load on the element and the longitudinal axis of the weld, and p_i is the ratio of the weld element deformation at intermediate stress Δ_i to its deformation at ultimate stress Δ_{mi}. The deformation of the ith element at intermediate stress level is assumed to be

linearly proportional to the deformation of the critical element. The critical element is the one with the lowest ratio between deformation at failure load Δ_{fi} to the distance from the ICR (r_i). Once the resisting force of each weld element is calculated, all weld force vectors are added to the system, and the static equilibrium of the system is checked against applied loads. Another iteration is executed if the equilibrium is not satisfied.

2.3.3. Combination Connections

The load-carrying capacity of eccentrically loaded combination connections is computed herein using the ICR method coupled with the load-deformation expressions for the slip resistance defined by Equations (2-2) and (2-3). All connecting elements (i.e., bolts and welds) are considered to be participating in a single load-sharing mechanism. Figure 2-2 shows, conceptually, the ICR force diagram for combination connections under eccentric load. After establishing the load-deformation behavior of the utilized connecting elements (i.e., bolts or welds) and defining their geometry, the location of the ICR of the whole system is assumed. Forces resisted by different connecting elements within the system are computed and their direction of application is assumed to be perpendicular to the line connecting the centroid of each fastener to the ICR. Once all the forces are computed and directions are assigned, equilibrium is checked and iterations over the location of the ICR are executed until equilibrium is attained.

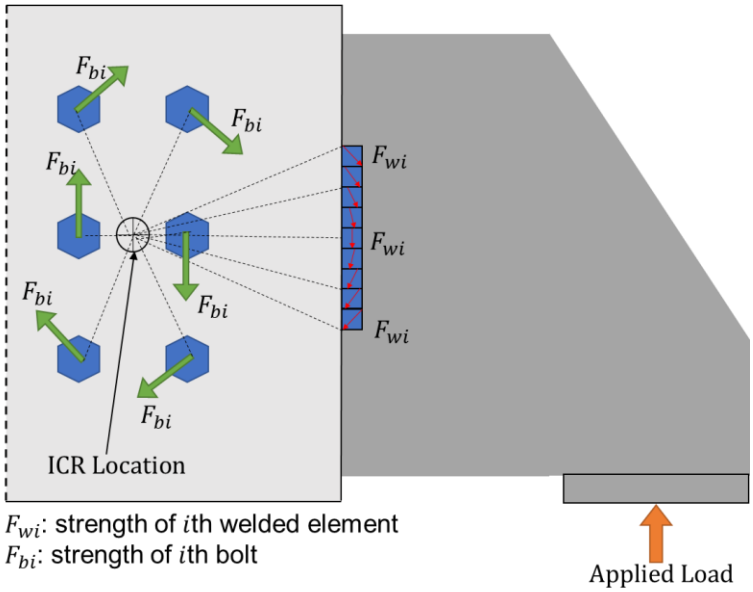

Figure 2-2. Force diagram for utilizing the ICR method for combination connections under eccentric load.

2.4. Experimental Testing Program

The behavior of combination connections under eccentric loading was evaluated experimentally as reported in Soliman et al. (2021). The experimental testing program included two main bolt patterns and load eccentricities. The bolt patterns are 2×3 and 1×6 and the corresponding load eccentricity is 165 mm and 127 mm, respectively. The specimens were composed of three components: the anchorage zone, the grip plates, and the test plate. Figure 2-3(a) shows a 3-Dimensional (3-D) rendering of the tested 1×6 connection, whereas Figures 3(b) and 3(c) show the connection details. All plates are made of A572 Gr. 50 steel and were designed such that connecting elements would fail before the occurrence of plate failure.

Both Class A and Class B faying surfaces were included in the test matrix. Six 19 mm diameter bolts were utilized in all tests and installed in short-slotted holes. Two 38 mm thick grip plates and a 76 mm thick test plate were used to construct the connections. Multiple specimens of each configuration were tested in the Bert Cooper Engineering

Laboratory at Oklahoma State University to better characterize the statistical variability in the behavior.

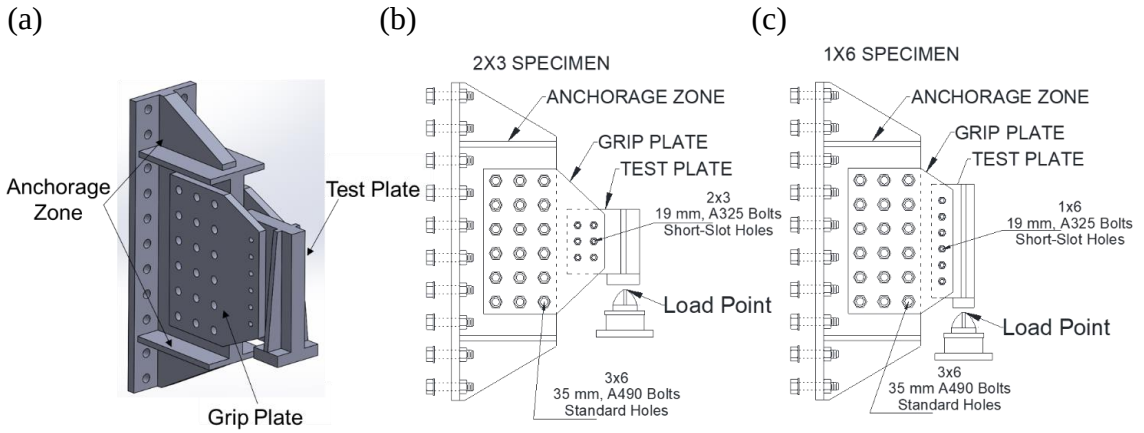

Figure 2-3. The tested eccentrically loaded connections: (a) 3-D rendering of a typical 1×6 connection tested in Soliman et al. (2021), (b) configuration of tested 2×3 connections, and (c) configuration of tested 1×6 connection.

Two fillet welds were placed longitudinally relative to the direction of the applied load to supplement the bolted connections. The fillet weld size was 8 mm while and length varied from 57 mm to 250 mm. The test matrix covered in the experimental program is shown in Table 2-1. More details about the test procedures, specimen design, detailed results, and research findings can be found in Soliman et al. (2021). The collected experimental results are utilized in this chapter to validate the ICR prediction approach and the FE model presented later in this chapter.

2.5. ICR Method Prediction Results

The maximum strength of connections under eccentric loading conditions depends on their load-rotation behavior. The AISC (2017) defines the maximum strength as the peak load that the connection can carry. If the load-rotation behavior does not show a peak, the strength of the connection can be defined as the maximum load achieved at rotations equal to or less than 0.02 radians (Leon et al., 1996). In general, the specimens tested within the experimental program reached their ultimate load at rotation less than 0.02 radians, except

for the bolted-only connections, which showed an increasing trend until bolt bearing condition was achieved. Accordingly, the experimental capacity of the tested connection R_{Test} is defined herein as the maximum load achieved at rotations equal to or less than 0.02 radians.

Table 2-1. Test matrix of eccentrically loaded connections and ICR prediction results using proposed formulations

Experimental Test Matrix							Results		
	Test No.	**Bolt Pattern**	**Bolt Type**	**Faying Surface**	**Weld Geometry (mm)**	**No. of tested Samples**	**ICR R_n (kN)**	**Test R_n (kN)**	**Strength Ratio (R_{Test} / R_{ICR})**
Bolted-Only	1	2×3	A325	A	-	2			
	2	2×3	A490	A	-	2			
	3	2×3	A325	B	-	2			
Welded-Only	4	-	-		8×114	3			
Bolted and Welded	5	2×3	A325	A	8×57	2	445	543	1.22
	6	2×3	A325	A	8×115	2	738	762	1.03
	7	2×3	A325	A	8×140	2	787	854	1.08
	8	2×3	A325	A	8×165	2	876	1026	1.17
	9	2×3	A490	A	8×114	2	694	824	1.19
	10	2×3	A325	B	8×70	2	685	717	1.05
	11	2×3	A325	B	8×152	2	1028	1108	1.08
	12	2×3	A325	B	8×191	2	1201	1272	1.06
	13	2×3	A325	B	8×230	2	1332	1503	1.13
	15	1×6	A325	A	8×76	1	780	984	1.26
	16	1×6	A325	A	8×160	1	1010	1192	1.18
	17	1×6	A325	A	8×203	1	1223	1319	1.08
	18	1×6	A325	A	8×250	1	1299	1633	1.25
									AVG = 1.14 STD = 0.076

The capacity of tested connections is predicted using the ICR method utilizing the as-built weld dimensions, measured pretension force, and faying surface characteristics acquired during the testing program. The mean values associated with different material properties required to calculate the capacity of the connection are summarized in Table 2-2. This capacity obtained using the ICR method is denoted R_{ICR}. The connecting elements (i.e., bolts and welds) are considered to be participating in a single load-sharing mechanism

and the frictional load-deformation behavior of the bolted connections given by Equations (2-2) and (2-3) are utilized. The R_{ICR} for each connection is plotted in Figure 2-4(a) against the corresponding experimental capacity R_{Test} to validate the accuracy of the ICR model. The strength ratio, calculated as R_{Test}/R_{ICR}, is also computed and reported in Table 2-1. Using Equations (2-2) and (2-3), the mean value of the computed strength ratio associated with the ICR method prediction (μ_{ICR}) is 1.14 with a standard deviation (σ_{ICR}) of 0.10 considering all combination tests. This is in contrast to the average value of the strength ratio of 1.29 reported in Soliman et al. (2021). These results indicate that the accuracy of the ICR model is enhanced when the proper load-deformation models of connecting elements are utilized.

Table 2-2. Statistical characteristics of considered random variables.

Variable	Best-fit Distribution	Mean	Standard Deviation	Reference
Friction Coefficient (Class A)	Lognormal	0.353	0.085	(Grondin et al., 2007)
Friction Coefficient (Class B)	Normal	0.545	0.113	(Grondin et al., 2007)
Load Eccentricity Ratio Bias (Actual/Nominal)	Normal	0.992	0.028	(Hess et al., 2002)
Weld Length Ratio Bias (Actual/Nominal)	Lognormal	0.95	0.044	(Soliman et al., 2021)
Weld Size Ratio Bias (Actual/Nominal)	Lognormal	0.83	0.12	(Soliman et al., 2021)
Weld Electrode Strength	Lognormal	540 MPa	50 MPa	(Hess et al., 2002)
Modules of Elasticity	Normal	200000 GPa	14 GPa	(Kwan et al., 2010)
Dead Load Uncertainty Factor	Normal	1.05	0.105	(Melchers & Beck., 2018)
Live Load Uncertainty Factor	Gumbel	1.0	0.25	(Melchers & Beck., 2018)
FE Bias Factor (Experimental /FE)	Normal	1.025	0.013	Derived
ANN Bias Factor (FE/ANN)	Normal	1.011	0.009	Derived

For each of the tested connections, the capacity is also estimated as the summation of the individual capacities of the welded connection and the slip-resistant connection, defined here as R_{sum}, $R_{sum}$and plotted against its matching R_{Test} in Figure 2-4(b). These

individual capacities are computed based on the ICR method using the same dimensions and material properties adopted for the computing R_{ICR}. As seen in the figure, the test capacity exceeded the summation with an average strength ratio (μ_{SUM}) of 1.55 and a standard deviation (σ_{SUM}) of 0.23. Accordingly, estimating the capacity of combination connections under eccentric loading using the ICR method, considering all connecting elements to participate in a single load-sharing system, is shown to be more rational and accurate than the summation. Therefore, the ICR method is recommended for designing these connections.

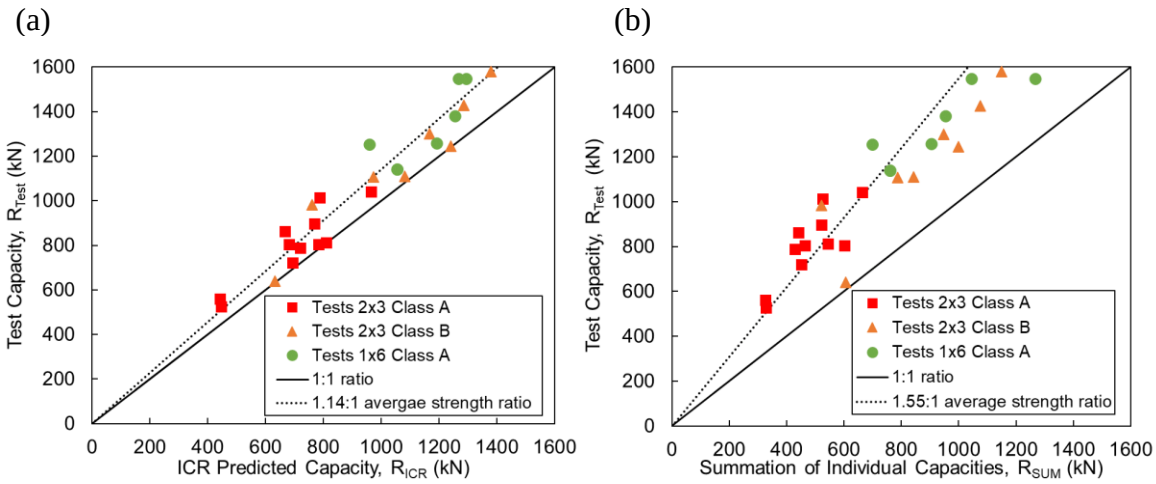

Figure 2-4. Strength ratio plot for eccentrically loaded combination connections based on (a) ICR method and (b) summation of the individual capacities.

2.6. Numerical Analysis

The experimental test results showed that the behavior of the combination connections is strongly influenced by the load eccentricity and weld attributes (Soliman et al., 2021). To develop a better understanding of the load transfer mechanisms through the combination connections, 3-D nonlinear FE models were developed and analyzed in ABAQUS software environment (Simulia, 2018). The FE models are also used later in this chapter to quantify

the effect of key input variables on the behavior of the investigated combination connections and to evaluate their reliability.

Eight-node continuum hexahedral solid element (C3D8R element) is utilized to model all structural components. To ensure simulation accuracy and minimize computational cost, a small mesh scale with a size of 2.0 mm is adopted for the contact regions (i.e., around the bolt holes and the weld region), while a coarse mesh with a size of 5.0 mm is used elsewhere. Figure 2-5(a) shows the finite element models corresponding to the 2×3 configuration with 150 mm long fillet welds. The welds are attached to the plates by using the ABAQUS tie constraint option. Loading and boundary conditions are defined to ensure that the modeled assemblies are subjected to similar conditions as the test specimens. As shown in Figure 2-5(a), a fixed boundary condition is applied to the end surface of the grip plates and the load is applied to the bottom surface of the test plate at 50 mm from the free end. The deformed shape and the von Mises stress distribution at the ultimate capacity of Test 8 are depicted in Figure 2-5(b).

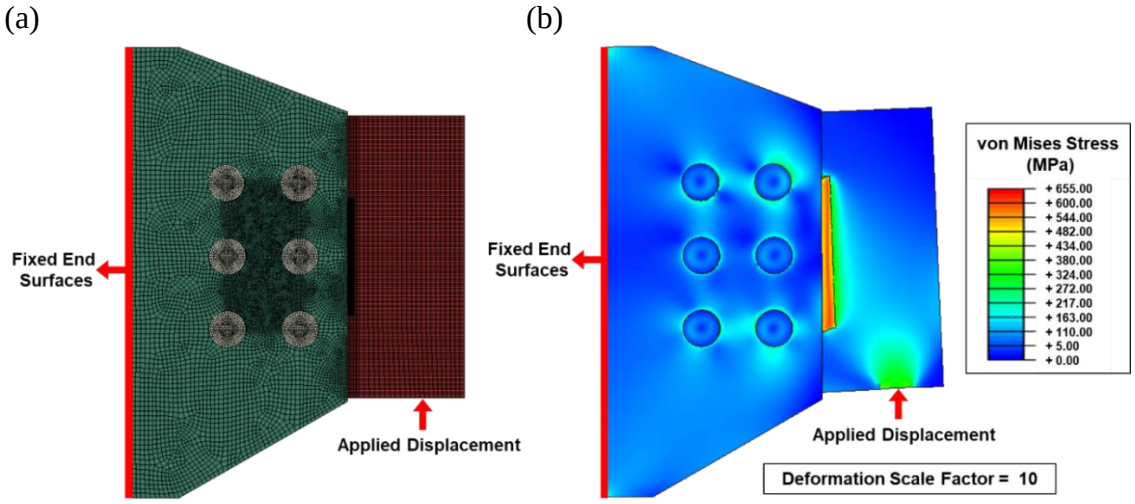

Figure 2-5. The finite element model corresponds to Test 8: (a) meshed model, applied loads, and boundary conditions and (b) the von Mises stress distribution and magnified displacements at the ultimate capacity of the connection.

The load in these simulations is applied on two steps; the pretensioning bolt forces are applied in the first step, then the bottom surface of the test plate is subjected to an upward displacement in the second step. The surface-to-surface contact in ABAQUS is utilized to model the frictional resistance of the faying surface. A nonlinear slip-dependent friction coefficient for Class A and B faying surfaces is defined based on Equations (2-2) and (2-3), respectively, for Class A and B faying surfaces. This slip-dependent friction coefficient is obtained by dividing the profiles in Equations (2-2) and (2-3) by the average pretensioning force recorded in Soliman et al. (2021) and listed in Table 2-2. Data for friction coefficient versus slip distance is tabulated and utilized to define the surface-to-surface contact characteristics in ABAQUS.

The FE model was validated based on the experimental load-rotation test results reported in Soliman et al. (2021). Eighteen FE models were constructed to cover the different experimentally tested configurations. Figures 2-6(a) to 2-6(f) show the experimental and numerically obtained load-rotation curves of different connection configurations. These include bolted- and welded-only connections, in addition to three different combination connection configurations. As shown, the FE model is able to capture the load-deformation behavior of the connection; especially with respect to the ultimate capacity and its associated rotation level.

The FE modeling results will be used later in this chapter to represent the real capacity of these connections in order to evaluate their reliability levels. Accordingly, it is essential to quantify the uncertainty associated with the FE model prediction. The bias factor associated with the FE model prediction was calculated to represent this uncertainty based on the ratio between the load-carrying capacity obtained experimentally and the

corresponding numerically obtained one (Hess et al., 2002). It was found that the bias factor follows a lognormal distribution with a mean and standard deviation of 1.012 and 0.025, respectively. Figure 2-7 depicts the lognormal probability plot for the bias factor associated with the FE capacity prediction compared to the experimental results. In summary, the presented FE model can be utilized to predict the ultimate capacity of eccentrically loaded combination connections with an average prediction error lower than 5%.

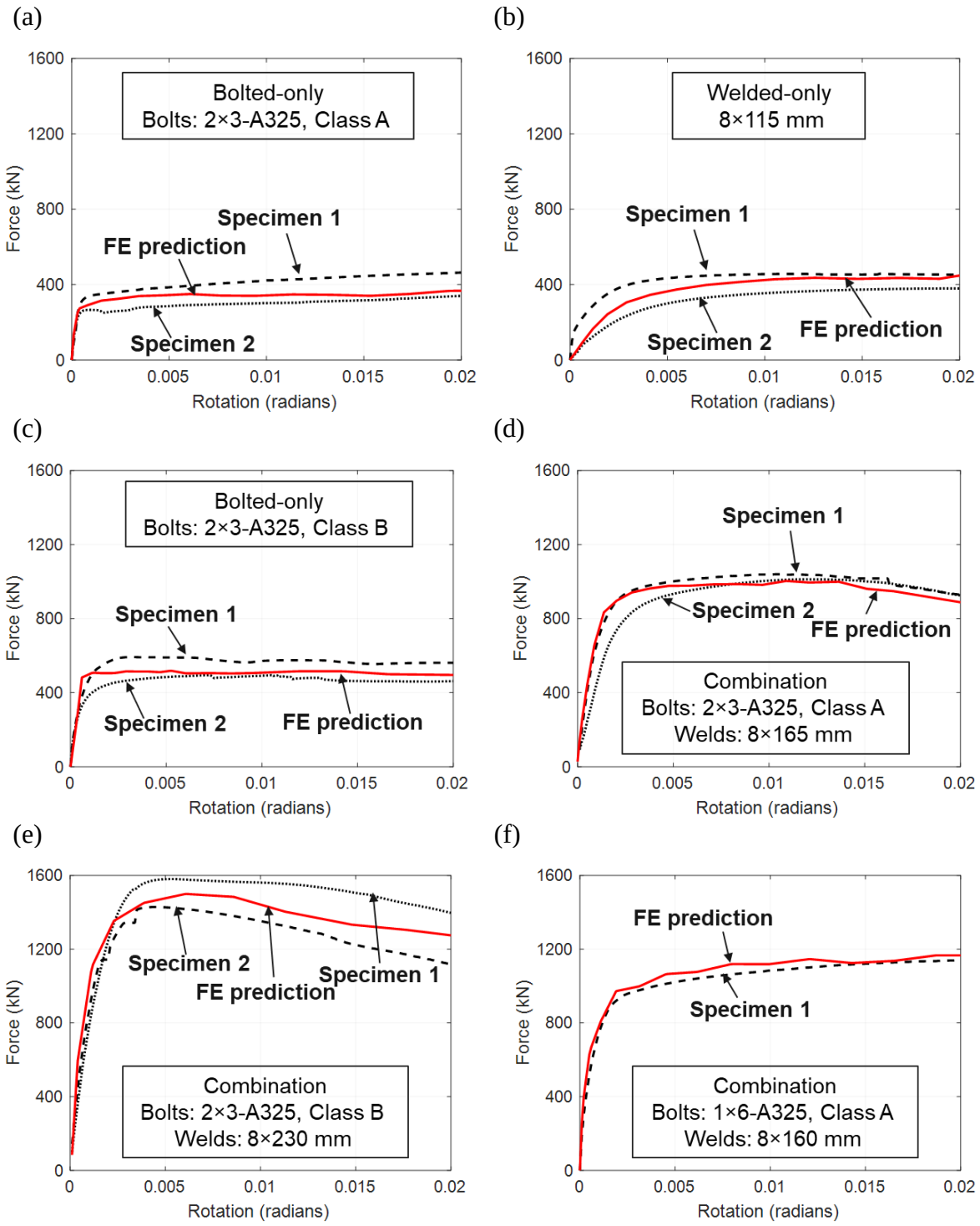

Figure 2-6. The force-rotation curves obtained from the FE model and experimental tests for the following connections (a) bolted only 2×3-A325-Class A, (b) welded only 8×115 mm, (c) bolted only 2×3-A325-Class B, (d) combination of bolts (2×3-A325-Class A) and welds (8×165 mm), (e) combination of bolts (2×3-A325-Class B) and welds (8×230 mm) and (f) combination of bolts (1×6-A325-Class A) and welds (8×160 mm).

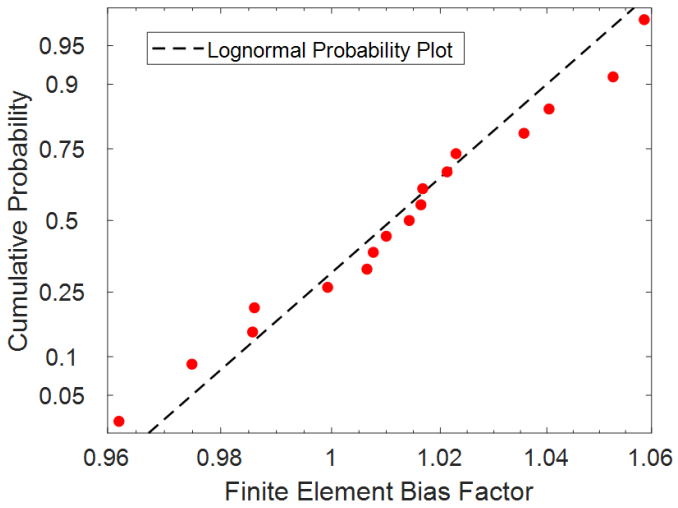

Figure 2-7. Lognormal probability plot of the finite element bias factor with respect to the mean value of the experimental capacity.

2.7. Load Sharing Behavior in Eccentrically Loaded Combination Connections

The experimental results indicated that the load-rotation behavior of these combination connections depends, to a great extent on the weld dimensions. Accordingly, it was of interest to the authors to investigate, utilizing the established FE modeling procedure, the load sharing behavior and how it is affected by weld dimensions. To assist in quantifying the contribution of different connecting elements to the overall capacity, multiple FE models are constructed and used to generate the load-rotation curves of the connections. The generated profiles included (a) bolted-only, (b) welded-only, (c) summation of bolted-only and welded-only profiles, and finally (d) combination connections with the same characteristics of the bolted and welded connections. The results are shown in Figures 2-8(a) and 2-8(b) for weld lengths of 125 mm and 225 mm, respectively. As shown in these figures, combining slip-resistant bolted connections and fillet welds that are loaded eccentrically led to an increase in capacity compared to the summation of the forces carried by their bolted- and welded-only counterparts. For the connections in Figures 2-8(a) and 2-8(b), this increase in the capacity is 3.5% and 10%, respectively. The increase in the

capacity can be related to the dimensions of the weld lines used to supplement the connection.

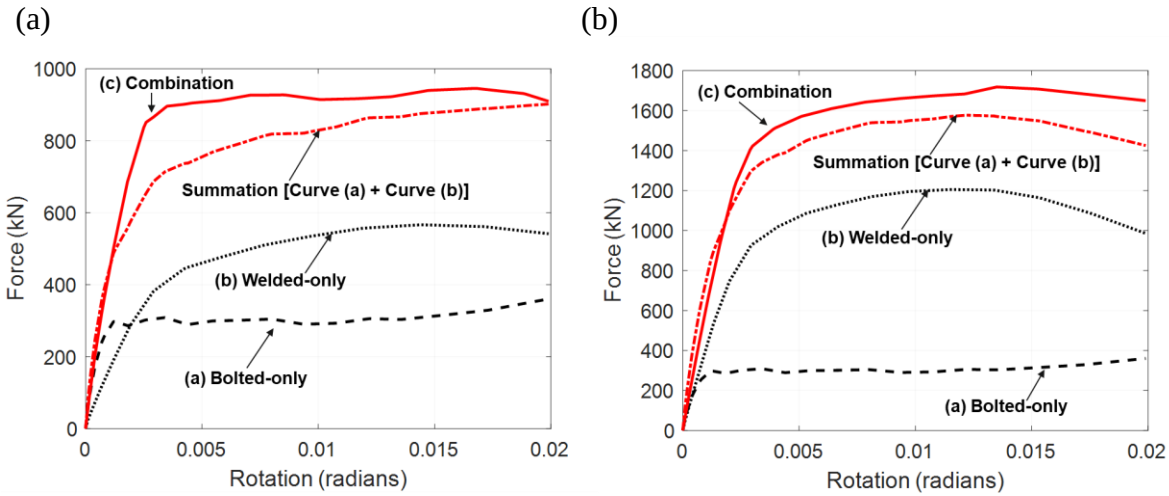

Figure 2-8. Load-rotation behavior of (a) combination of bolts (2×3-A325-Class A) and welds (8×125) mm and (b) combination of bolts (2×3-A325 Class A) and welds (8×225 mm).

This behavior can be attributed to the load distribution between the bolts and welds in the shared load system due to the change in the ICR location in the combined mechanism compared to that of the bolted- and welded-only counterparts. The distance between the location of the applied load and the ICR (denoted ICR distance thereafter) is visually depicted in Figure 2-9 for two combination connections discussed in Figure 2-8 and the corresponding bolted- and welded-only connections. As shown in Figure 2-9, when weld lines with a length of 125 mm are used to supplement the bolted connection, the ICR distance for the combination connection is higher than that of the welded-only but slightly lower than that of the bolted-only. Therefore, compared to weld-only connections, the contribution of welds to the combined force resisting mechanism is expected to be higher, but the contribution of bolts can be lower than that of the bolted-only connection. However, when 225 mm weld lines are used, as illustrated in Figure 2-9, the ICR distance for the combination connection exceeds that of welded- and bolted-only cases. This causes the

contribution of both bolts and welds to the combined force resisting mechanism to be higher than the corresponding bolted- and welded-only connections.

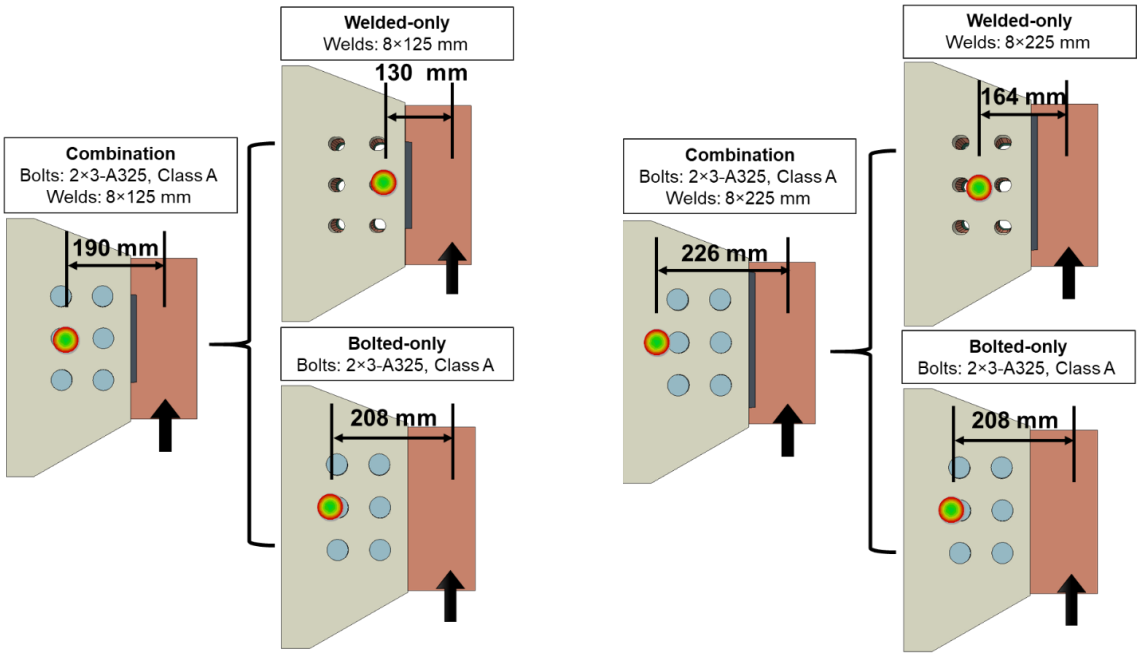

Figure 2-9. The ICR location for two configurations of combination connections and the corresponding bolted- and welded-only.

The analysis in Figure 2-8 is conducted on more connection configurations with various weld lengths. The analysis included 2×3 bolt patterns and weld lengths ranging from 25 mm to 250 mm. For each weld length case, the ratio between the maximum load obtained from the combination connection and the summation of the individual capacities of bolted- and welded-only connections is computed. Figure 2-10 depicts this ratio for connections with different weld lengths. As shown in the figure, the summation model slightly overpredicts the capacity for short weld lengths and underpredicts it for longer weld lengths. Again, this is attributed to the change in the ICR distance in the combination connections compared to the corresponding bolted- and welded-only cases.

Next, the contribution of the resistances provided by the bolts and the welds to the combined force-sharing mechanism is evaluated using the FE models. Figure 2-11(a)

shows, for different weld lengths, the ratio between the force carried by the welds in the combination connections to the capacity of the welded-only connection. As shown, for the considered configurations, the weld carries a higher force compared to the welded-only connection. Figure 2-11(b) shows the ratio between the force resisted by the bolts (i.e., the frictional resistance) in the combined mechanism to the bolted-only connection. At small weld lengths, this ratio is less than one, indicating that bolt contribution is less than the bolt-only capacity. However, for longer weld lengths, this ratio exceeds one. Accordingly, combining bolts and welds in a single load-sharing mechanism to resist eccentric loads can increase the efficiency of individual connecting elements.

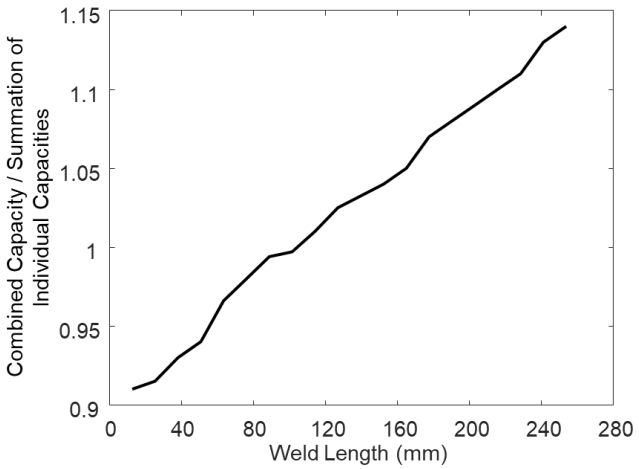

Figure 2-10. The ratio between the maximum capacity obtained from the combination connection and the summation of separate capacities of bolted- and welded-only counterparts.

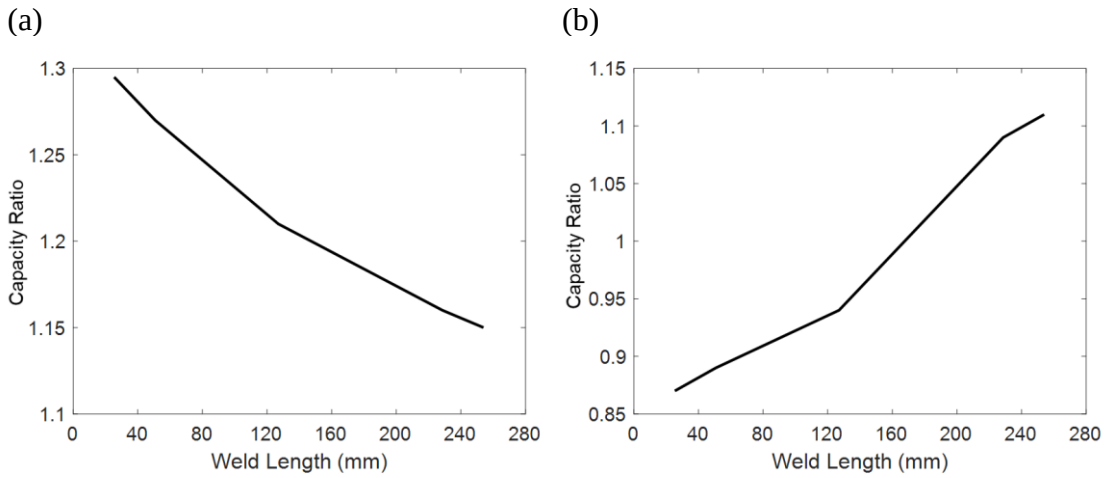

Figure 2-11. The ratio between the force carried by the welds or bolts in the combination connections to the corresponding (a) welded-only and (b) bolted-only connections.

2.8. Reliability Analysis

The reliability index provides insight into the ability of the component to function under the stated design parameters and loading conditions. This performance indicator can be computed using approximate numerical methods, including the First- and Second-Order Reliability Methods (Cornell, 1969; Der Kiureghian et al., 1987), and simulation methods, such as the MCS. Simulation methods are based on sampling a large number of realizations, then evaluating the failure probability from these samples. Simulation methods are commonly used due to their capability of addressing a wide range of structural reliability problems with non-linear performance functions and a large number of random variables (Shittu et al., 2020). Accordingly, MCS is employed in this chapter to compute the reliability index for eccentrically loaded combination connections under different weld lengths and load eccentricities. The capacity of the connection should be obtained from the FE model for each of the considered samples. To reduce the computational cost associated with the simulation, it is desirable to evaluate the uncertainty associated with each of the input parameters and treat only the key contributing variables that have an impact on the

capacity as random variables. This is accomplished in this chapter following Sobol's approach (Sobol, 2001) for variance-based sensitivity analysis.

2.8.1. Sensitivity Analysis of the Capacity of Combination Connections

In the sensitivity analysis, the geometrical properties (i.e., weld length, weld size, load eccentricity), material properties (i.e., Young's modulus and electrode strength), pretensioning force, and friction coefficient are considered as input parameters. The probabilistic descriptors associated with weld length, weld size, and pretensioning force are considered based on data reported in Soliman et al. (2021). Figures 12(a) and 12(b) show the histograms of the bias ratio associated with the weld length and weld size, respectively, as well as the best-fit probability distribution function (PDF). The values in these histograms represent the ratio between the as-built weld length or size and the nominal values. Figure 2-12(c) shows the histogram and the best-fit PDF of the pretension force. The data provided by Grondin et al. (2007) is used to find the probabilistic descriptors of the friction coefficient for Class A and B surfaces. The probabilistic distributions of material parameters (i.e., weld elastic modulus and weld electrode strength) and load eccentricity are established based on the data reported in Hess et al. (2002). The probabilistic descriptors of the adopted random variables are summarized in Table 2-2.

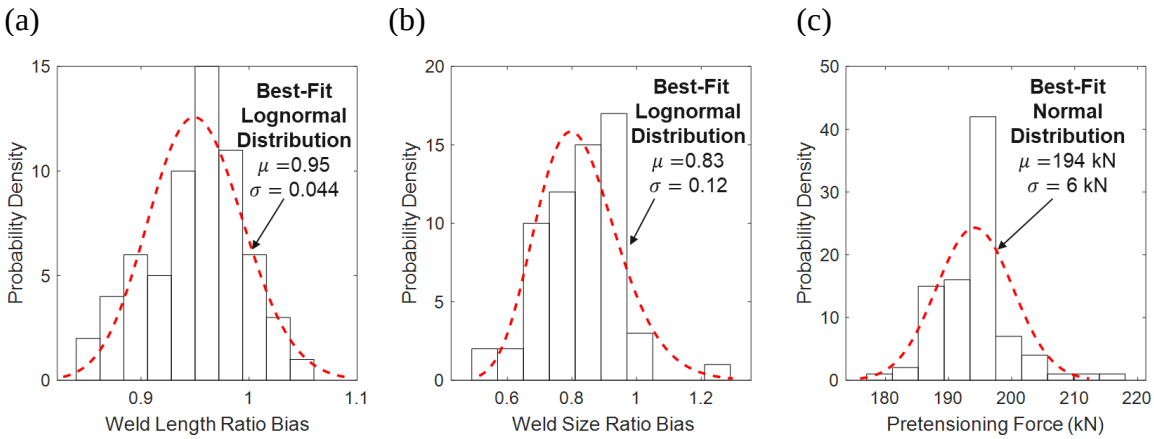

Figure 2-12. Histograms of the experimental data and best fit PDF of (a) the weld length ratio bias, (b) weld size ratio bias, and (c) pretensioning force.

The validated FE model is used to conduct a variance-based sensitivity analysis given the marginal distribution of the selected random variables. Partial and total Sobol's indices (Sobol 2001) are computed next. Sobol's approach decomposes the response function $F(\boldsymbol{X})$ into summands of increasing dimensionality, such that each successive dimension represents increasing degrees of interaction among the parameters. This decomposition is expressed as (Sobol, 2001):

$$F(\mathbf{X}) = F_0 + \sum_{1\le i\le n} F_i(X_i) + \sum_{1\le i\le j\le n} F_{ij}(X_i, X_j) + \cdots + F_{1\,2\ldots n}(X_1, \ldots, X_n) \qquad (2\text{-}4)$$

where $\mathbf{X}$ is the input vector having n random parameters, F_o is the mean value of the response function, F_i is a function representing the portion of $F(\mathbf{X})$ affected by parameter X_i, F_{ij} is the portion of $F(\mathbf{X})$ resulting from the interaction between X_i and X_j. Consequently, the total variance D of $F(\boldsymbol{X})$ is calculated as:

$$D = Var[F(\boldsymbol{X})] = \int_{k^n} F^2(\boldsymbol{X}) dX - F_0^2 \qquad (2\text{-}5)$$

where the input parameters are defined on the n-dimensional unit cube k^n. By integrating the square of Equation (2-5), it is possible to decompose the variance as:

$$D = \sum_{1\le i\le n} D_i + \sum_{1\le i\le j\le n} D_{ij} + \cdots + D_{1\,2\ldots n} \qquad (2\text{-}6)$$

where D_i is the partial variance of parameter X_i, D_{ij} represents the partial variance due to the interaction between parameters X_i and X_j, and $D_{1\,2\ldots n}$ is the partial variance due to the interaction between parameters X_1 to X_n. Sobol's sensitivity indices can then be computed as

$$S_i = \frac{D_i}{D} \tag{2-7}$$

$$S_{ij} = \frac{D_{ij}}{D} \tag{2-8}$$

where, S_i is the first-order sensitivity index which corresponds to the change in the variance of the output due to change in *i*th parameter alone, while the higher-order sensitivity indices S_{ij} express the change in the variance of the output due to the interactions among multiple variables. Next, the total Sobol's sensitivity index (S_i^T) of one parameter X_i can be expressed as the summation of the first and higher-order sensitivity indices.

The sensitivity analysis is conducted on the investigated connections with 2×3 and 1×6 bolt patterns and Class A and B faying surfaces. UQ-Lab (Marelli and Sudret, 2014) MATLAB toolbox is used to calculate the sensitivity indices associated with the variables of the investigated connections. The FE model is employed to generate the force-rotation curves given a certain set of input parameters. The maximum load attained at rotation equal to or less than 0.02 radians is designated as the response parameter of interest. Low-rank tensor approximation (LRA) (Konakli & Sudret, 2016) is used to calculate Sobol's indices associated with different input parameters.

Figures 2-13(a) and 2-13(b) present the sensitivity results for the investigated connections utilizing Class A and B faying surfaces, respectively. As shown, the mechanical properties of the weld (i.e., Young's modulus and electrode strength) have a

low effect on the system response compared to the other parameters. The system response is strongly influenced by the variability in the weld dimensions. The load eccentricity also has a significant effect on the response with indices of 0.27 for Class A and 0.24 for Class B connections. An increase in all the considered parameters led to a corresponding increase in the connection capacity except for the load eccentricity. Based on the results of this analysis, all input parameters will be considered as random variables within the reliability analysis except for Young's modulus of the welds, which is assumed deterministic.

(a) (b)

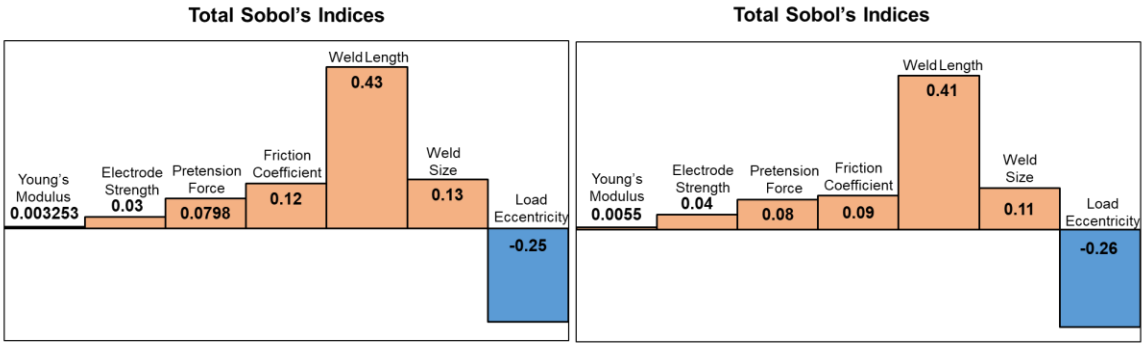

Figure 2-13. Computed total Sobol's indices for different input parameters of the investigated eccentrically loaded combination connection with (a) Class A and (b) Class B faying surfaces.

2.8.2. Performance Function for Reliability Assessment

The AISC specification adopts the Load and Resistance Factor Design (LRFD) for the design of steel structures. The basic formula in LRFD is (Galambos and Ravindra, 1981):

$$\emptyset R_n \geq \sum_{K=1}^{i} \gamma_k S_{km} \tag{2-9}$$

where the left side of this equation is known as the design strength while the right side represents the demand from applied loads. $\emptyset$ is the resistance factor, S_{km} is the load effect, while γ_k is the load factors associated with each load effect S_{km}. R_n is the nominal resistance to be calculated herein based on the ICR approach discussed above for the

combined capacity prediction. According to ASCE/SEI (2016) guidelines, the following load combination is to be used under the presence of dead and live loads:

$$\emptyset R_n \geq \left(1.2\overline{D} + 1.6\overline{L}\right) \tag{2-10}$$

where $\overline{D}$ is the mean dead load effect and $\overline{L}$ is the mean live load. Since these connections may be utilized in different structures and/or configurations, it is not possible to predict the actual loads applied to the connection. Accordingly, applied loads will be estimated by rearranging Equation (2-10) assuming that the connection will be utilized at its full nominal capacity. The mean applied dead load effect can be calculated as:

$$\overline{D} < \left(\frac{\emptyset R_n}{1.2+1.6(\bar{L}/\bar{D})}\right) \tag{2-11}$$

where $\bar{L}/\bar{D}$ represents the ratio between the mean applied live to dead loads. The mean total load effects acting on the connection ($\overline{L}_T$) is:

$$\overline{L}_T = \overline{D} + (\bar{L}/\bar{D})\,(\overline{D}) \tag{2-12}$$

The total load effect is calculated considering the uncertainty in load prediction as:

$$\overline{L}_T = \gamma_D \overline{D} + \gamma_L \overline{L} \tag{2-13}$$

where γ_D and γ_L are the uncertainty factors associated with dead and live loads, respectively. The performance function $G(\mathbf{M})$ can be defined as follows for quantifying the failure probability:

$$G(\mathbf{M}) = \lambda_R R(\mathbf{M}) - L_T \tag{2-14}$$

where λ_R represents the modeling uncertainty to cover the FE prediction and any surrogate models used, $R(\mathbf{M})$ is the actual capacity of the connection, $\mathbf{M}$ represents the vector of design variables parameters, and L_T is the total load effects calculated using

Equation (2-13). This performance function is next implemented into a MCS process to calculate the probability P_e of load effects exceeding the resistance as:

$$P_e = P[G(\boldsymbol{M}) < 0] \tag{2-15}$$

The reliability index is then calculated as a function of the probability of exceedance:

$$\beta = \Phi^{-1}[1 - P_e] \tag{2-16}$$

where Φ^{-1}denotes the inverse standard normal distribution function, and β is the reliability index based on the capacity of the connection.

2.8.3. Predicting the Capacity of Connections in the MCS

Based on the results of the sensitivity analysis, the load eccentricity and weld dimensions were found to have a significant effect on the behavior. Accordingly, it was desirable to compute the reliability for connections utilizing a wider range of these input parameters than those evaluated experimentally. For a certain combination of these design parameters, a FE model is to be constructed and executed iteratively to compute the capacity of the connection for each sample in the MCS process. As a result, it was not possible to conduct these simulations using the FE analysis directly given the computational cost involved. To address this issue, ANNs are utilized to surrogate the FE model and provide the capacity of the connection given a certain set of input parameters. Feedforward ANNs are selected due to their computational efficiency compared to the other ANN types (Mehta et al., 2019). The Levenberg–Marquardt Algorithm is utilized as the training algorithm due to its accuracy and fast convergence (Hagan & Menhaj, 1994).

Since it was desirable to compute the reliability considering various connection configurations (e.g., different load eccentricities and weld dimensions), a wide range of variation in the input parameters is considered to create the ANN training dataset. For

instance, connections with weld lengths ranging from 50 mm to 250 mm are considered. Weld sizes between 6.35 mm and 12.7 mm are also included. The training dataset covers bolt pretension forces ranging between 110 and 250 kN and load eccentricities within a range of 125 to 300 mm. Bolt patterns of 2×3 and 1×6 for connections with Class A and B faying surfaces are also included in the training dataset. The Sobol sequence experimental sampling design technique (Sobol & Levitan, 1999) is used to select the combinations of input parameter values to be used for creating the training dataset. A total of 28,000 samples are generated for training and testing the ANN. Among those, 75% is used to train the ANN, 15% is used for validation, and 10% is used for testing.

A feedforward ANN with 6 hidden layers and 5 neurons for each layer is constructed to establish a relation between the FE-obtained capacity and the associated set of input parameters. The neural network toolbox in MATLAB (MathWorks, 2020) is used to conduct this analysis. To ensure that the trained ANN model is not experiencing overfitting and eliminate the possibility of deviation when analyzing a dataset not included in the training data, a new testing dataset including 1,000 samples is selected randomly from the ranges of input parameters and tested against the FE results. Figures 2-14(a) and 2-14(b) show a comparison between the FE results and the ANN prediction for the considered Class A and Class B connections, respectively. As shown, the ANN can provide an accurate prediction of the capacity; accordingly, it will be used directly in the MCS process.

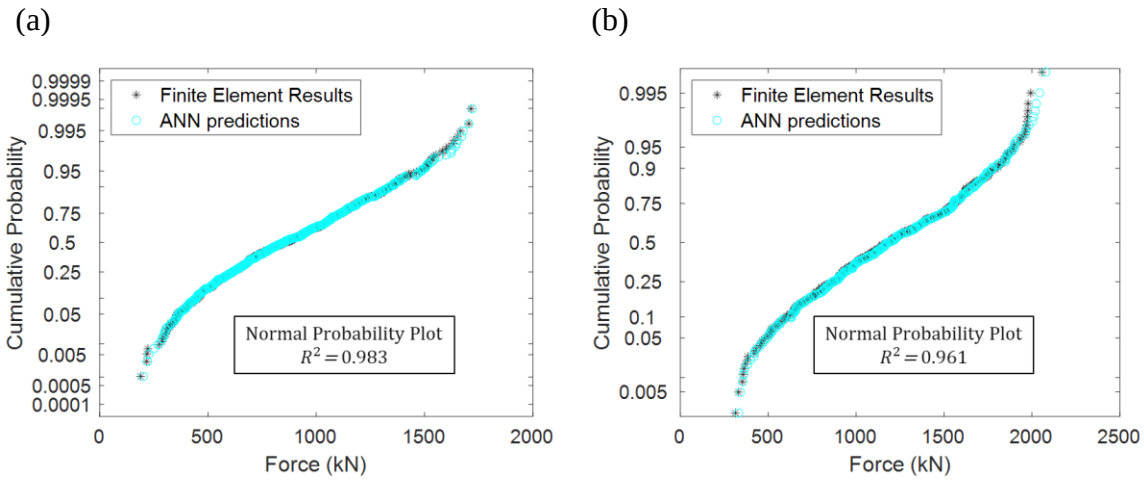

Figure 2-14. Comparison between the FE results and the ANN prediction for the investigated connections with (a) Class A and (b) Class B faying surfaces.

2.8.4. Reliability Analysis Results

Based on the results of the sensitivity analysis, for a given design configuration, the uncertainty in actual weld length, weld size, load eccentricity, pretensioning force, and friction surface coefficient is considered by treating them as random variables in the MCS. The statistical descriptors of the considered random variables are presented in Table 2-2. Based on the results of a convergence analysis, five million samples are drawn from each random variable and used to compute the failure probability using the performance function given by Equation (2-14). The capacity of the connection is calculated using the trained ANN while the load effects are computed using Equations (2-9) to (2-13). The probability of failure and reliability index are then calculated using Equations (2-15) and (2-16), respectively.

The MCS is next conducted on a large set of connections compared to those considered experimentally. The analysis included 2×3 and 1×6 bolt patterns, weld lengths ranging from 25 mm to 250 mm, weld sizes of 6.35 mm to 12.5 mm., and load eccentricities of 125 mm to 300 mm. Figure 2-15(a) shows the reliability index profile of two samples of these connections with Class A and B faying surface considering the resistance factor

$\emptyset$ =1.0. The figure shows the change in reliability with respect to the $\bar{L}/\bar{D}$ load ratio for connections with load eccentricity of 175 mm, weld length of 150 mm, and 8 mm weld size. As shown in the figure, the reliability drops with the increase in the $\bar{L}/\bar{D}$ load ratio since the variability in the live load is higher than that associated with dead loads. Furthermore, although connections with Class B faying surfaces have a higher capacity than those with Class A, they have a lower reliability index due to the difference in the ratio of the mean experimental friction coefficients reported in literature and the adopted design values.

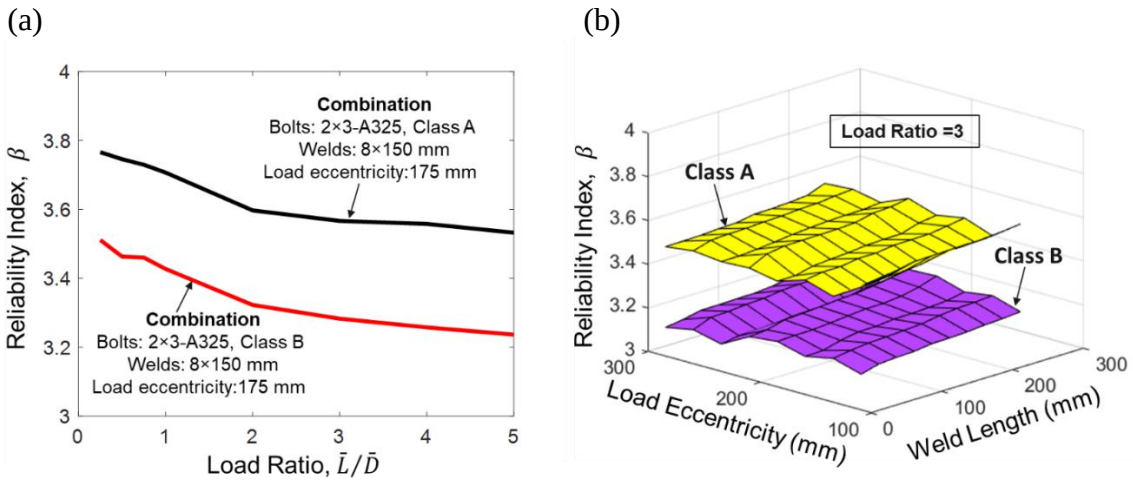

Figure 2-15. Calculated reliability indices for slip-resistant bolted connections combined with fillet welds considering (a) load eccentricity of 175 mm and two 8 mm × 150 mm fillet welds and (b) various weld lengths and load eccentricities.

To study the effect of weld length and load eccentricity on the reliability index, the analysis in Figure 2-15(a) is conducted on several combination connection configurations considering variations of these two parameters. Figure 2-15(b) depicts the resulting reliability index surfaces computed at $\bar{L}/\bar{D}$ of three. As shown, the weld length and load eccentricity do not have a significant impact on the connection reliability. From the figure, the reliability of these connections at $\bar{L}/\bar{D}$ = 3.0 ranges between 3.10 and 3.58 depending on the condition of the faying surface. The AISC *specifications* (AISC, 2016) adopts a

target reliability index of four at $\bar{L}/\bar{D}$ = 3.0 for connections. As seen in Figure 2-15, the reliability of these combination connections designed using the ICR method is lower than this target reliability index; accordingly, it is necessary to choose appropriate resistance factors to be implemented in the design. Figure 2-16 shows the average reliability index against the load ratio $\bar{L}/\bar{D}$ for various resistance factors for Class A and B connections. The figure shows that a resistance factor of 0.75 provides a high reliability level under different $\bar{L}/\bar{D}$ ratios. In addition, resistance factors of 0.85 and 0.8 can also be adequate for connections utilizing Class A and B faying surfaces, respectively.

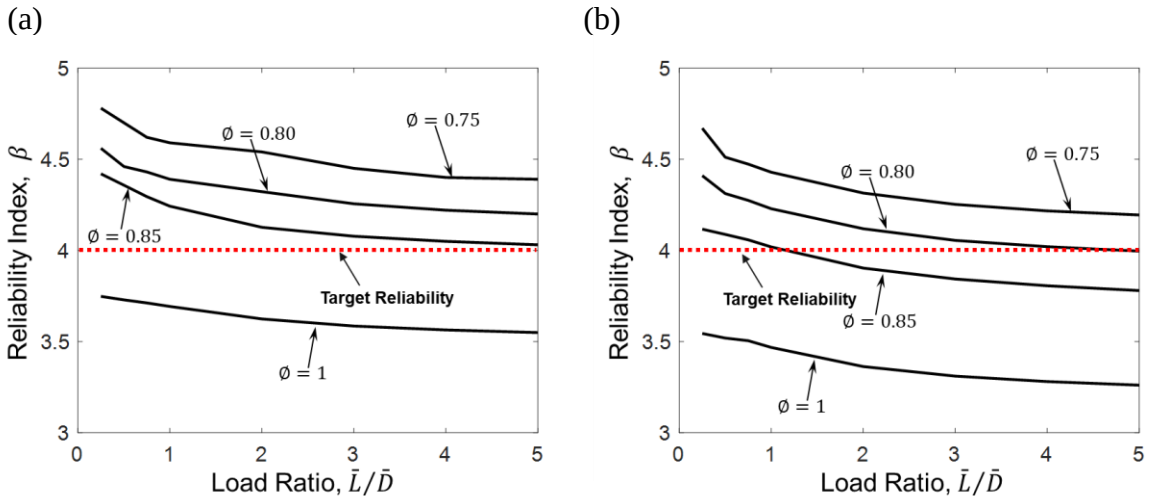

Figure 2-16. Calculated average reliability indices with respect to the resistance factor for the investigated connections with (a) Class A and (b) Class B faying surfaces.

2.9. Conclusions

This chapter provided an in-depth investigation into the behavior of eccentrically loaded steel connections combining fillet welds and high-strength pretensioned bolts. The capacity of the combination connections was calculated using the ICR method when connecting elements are considered as a part of a single load resisting system. A newly developed load-deformation model for the slip resistance introduced by the pretensioned bolts was utilized to improve the ability of the ICR method to predict the capacity. Three-dimensional

FE models representing the investigated connections were developed and validated utilizing experimental results. The load sharing and transfer mechanisms within the combination connections were studied using the validated FE models. Finally, this chapter integrated FE analysis, ANN, and MCS to evaluate the reliability level of these connections. The following conclusions can be drawn:

- The ICR method can be used to predict the load-carrying capacity of eccentrically loaded combination connections. This requires considering the connecting elements to be participating in a single load resisting system and utilizing proper load-deformation characteristics of slip-resistant bolted connections. A simple summation of individual resistances provided by the bolts and welds may not achieve accurate estimates of the combination connection capacity.
- The proposed load-deformation models for slip-resistant bolted connections enhance the ability of the ICR method to predict the load-carrying capacity of eccentrically loaded slip-resistant bolted connections combined with fillet welds. These models can also be adopted in predicting the capacity of bolted-only slip resistance connections using the ICR method.
- For the investigated combination connections, the load-rotation behavior was found to depend on the weld-to-bolt strength ratio (Rn_w/Rn_b). The improvement in the overall capacity, compared to the individual capacities provided by the bolts and welds, was relative to the ratio between welds capacity and bolts capacity.
- The efficiency of individual connecting elements in resisting eccentric loads can be improved by combining bolts and welds in a single load-resisting mechanism. Given the location of the ICR in the combined system, connecting elements can

carry more eccentric loading in the shared mechanism compared to their capacity if used separately.

- The reliability analysis conducted on the investigated connections shows that these connections, when designed using the ICR method, can achieve high reliability levels using a resistance factor of 0.75. A higher resistance factor can also be used for connections with Class A and B faying surfaces to provide an adequate reliability index under various live-to-dead load ratios.

CHAPTER III

QUANTIFYING FATIGUE DETERIORATION OF SHIP STRUCTURES UNDER CHANGING CLIMATE CONDITIONS

3.1. Overview

The randomness of sea conditions and loading sequences are among the key contributing factors that affect our ability to accurately predict the fatigue crack growth in ships. Climate change may alter the long-term characteristics of these factors along the service life of existing or newly constructed ships. Climate variability and its effect on the stochastic nature of ship loading may increase the complexity of crack growth prediction in marine structures. This chapter presents a framework for quantifying the impact of climate change on crack propagation in ship hulls. A probabilistic fatigue crack propagation approach is developed to account for uncertainties associated with material properties and loading conditions; specifically, those affected by climate change. Global Climate Models (GCMs) are used to quantify the long-term effects of climate change on the sea conditions and the resulting ship loading time histories. The proposed approach is applied to a tanker ship operating within predefined routes in the Atlantic Ocean. The results show that the effect of climate change on the crack propagation depends on the navigation route. While several routes displayed a reduction in the crack growth activity within the prediction time frame, some routes showed up to 8% decrease in the expected fatigue service life.

3.2. Background

Marine structures are generally designed with adequate reliability to resist wave loading and aggressive marine environmental conditions. These loading and environmental conditions can lead to strength failure (e.g., by yielding or buckling) or gradual deterioration due to fatigue and corrosion. Fatigue damage accumulation depends on the material and geometric characteristics of the ship, the operational profile (i.e., ship speed and heading angle), and the encountered sea environments (Mao et al., 2012). A ship is generally exposed to millions of load cycles during its service life (DNV, 2001). This large number of load cycles can lead to fatigue crack propagation which may cause a drop in the structural reliability of the vessel. To accurately predict the fatigue crack growth in ship hulls, a complete time history profile of the stress at the investigated detail is needed. Analysis of the ship operation data including navigation speed, heading angle, and encountered sea states (i.e., significant wave height and period) is required to establish a comprehensive life-cycle load profile. In traditional ship design and assessment approaches, sea state information obtained from previous operational data are considered to be representative of the sea conditions for future load prediction (Vanem et al., 2013). However, climate change can affect the frequency and intensity of average (i.e., normal) and extreme weather events as compared to historical records (Stott, 2016).

Wave-induced loads are among the stressors that are significantly affected by the climate conditions along the ship route (Bitner-Gregersen et al., 2018). However, long-term prediction of wave conditions is a complex process that represents a challenge during the life-cycle assessment and design of ship hulls (Bernard & Robinson, 2009). A comparison of recent climate trends to average historical conditions has shown

considerable differences in various wave parameters (e.g., wave height and period) and storm characteristics (e.g., duration, intensity, frequency, and affected area) in different locations around the world (Reguero et al., 2019). Global Climate Models (GCMs) can be utilized to simulate the atmosphere and project future climate variability. A GCM is a mathematical representation of the atmosphere, sea ice, land surface, and oceans that considers physical, biological, and chemical aspects of the global climate system (Williams et al., 2013). These models provide long-term projections for several variables such as precipitation, temperature, wind speed, and wind direction. GCMs have been widely used to assess the impact of climate change in various applications such as long-term flood prediction (McPherson, 2016), bridge risk analysis (Khandel & Soliman, 2019, 2021), and land cover use (Boone et al., 2016).

Several studies have investigated the effects of climate change on sea waves using available GCMs. Grabemann and Weisse (2008) employed two GCMs and two greenhouse gas (GHG) emission scenarios to study climate change effects on the mean and extreme wave conditions in the North Sea. Their study projected an increase in the frequency of severe sea states and 5-8% increase in the extreme wave height in the southern and eastern parts of North Sea by the end of the 21st century. Zacharioudaki et al. (2011) employed two climate models to conduct a similar investigation in North East Atlantic. Their projected results showed a long-term decrease in the mean wave height in most of the investigated areas. Brown et al. (2012) investigated the effect of climate change on the storm surge and wind speed in the eastern Irish Sea. Their results showed a reduction in the frequency and monthly mean of extreme wave and wind events. Nicholls et al. (2015) examined the change in the wave height in the North East Atlantic and projected a future shift in storm

track that increases the wave height in south west of the United Kingdom and decreases it in the north of Scotland. Aarnes et al. (2017) employed six climate models and two GHG emission scenarios to investigate the mean and extreme wave conditions in the North East Atlantic and projected a decrease in significant wave height by the end of 21st century. Bricheno & Wolf (2018) also projected a long-time decrease in significant wave height along the European Atlantic Coast.

Despite the significant effort in literature aiming at quantifying the effects of climate change on wave characteristics, to the best of the authors' knowledge, none of the available studies quantified the effect of climate change on the fatigue crack propagation in ship hulls under uncertainty. Such quantification is essential to develop effective long-term life-cycle management procedures capable of maintaining the ship reliability above acceptable thresholds. Although crack propagation under uncertainty has been investigated in literature (e.g., Gope, 2016; Maljaars & Vrouwenvelder, 2014; Soliman et al., 2016), the impact of climate change on the fatigue life of ship structures has not been considered.

To address this knowledge gap, this chapter presents an innovative simulation-based framework for predicting the failure probability of ships under growing cracks in light of climate change. The chapter also discusses the impact of climate change on the wave parameters and storm characteristics across the Atlantic ocean and principal shipping routes. GCMs are employed to quantify the effect of climate change on the significant wave height (SWH) and wave-induced loads. A combination of several model types and GHG emission levels are used to define several climate scenarios and project future wind speed and direction along predefined navigation routes. The Joint North Sea Wave Project (JONSWAP) spectra (Hasselmann et al., 1973) and projected wind data are used to

construct the wave-induced load profiles along the service life of the ship. A 3-D nonlinear FE model is established and used to extract essential parameters used to model crack propagation under variable sea loading. An analytical crack advancement rule based on the model proposed by Huang et al. (2008) is used in conjunction with the FE analysis to quantify the crack propagation characteristics. MCS is used to quantify the probability of fatigue failure under the projected load profiles. The proposed approach is illustrated on a tanker operating in the Atlantic Ocean.

3.3. Climate Modeling

The excessive increase in GHG emission has led to various effects on the climate (Stocker, 2014). These include sea-level rise, global temperature increase, and imbalance in precipitation and wind patterns (Meinshausen et al., 2011; Solomon et al., 2007). Several research studies have recently focused on formulating models and methodologies to better understand the future effects of climate change on atmospheric conditions around the globe. In this context, the Coupled Model Inter-comparison Project Phase 5 (CMIP5) provides a set of global climate models that project future climate conditions on two timescales, near-term (up to 2035) and long-term (up to 2100). These models are often calibrated by comparing their projections to climate data observed in the past short-term (Taylor et al., 2012). CMIP5 database consists of more than 50 different GCM models with the capability of projecting various climate-related parameters. In order to project climate conditions into the future, different climate radiative forcing scenarios are defined with respect to the level of predicted atmospheric GHG emission in 2100. CMIP5 models provide output data based on radiative forcing scenarios recommended by the Intergovernmental Panel on Climate Change (IPCC) (Stocker, 2014). These scenarios are

known as Representative Concentration Pathways (RCPs). Four RCP scenarios recommended by IPCC, and adopted in CMIP5, are RCP 2.6, RCP 4.5, RCP 6.0, and RCP 8.5. The numerical figure in these scenarios represents the amount of radiative forcing in Watts per square meter (W/m^2) in the year 2100.

Natural fluctuation of the climate system that is independent of the radiative forcing is known as internal variability (Hawkins & Sutton, 2009). To address this source of variability, different initial conditions are used to provide several output datasets associated with each GCM and radiative forcing scenario. Accordingly, to properly account for various sources of uncertainty associated with GCM projections, it is essential to consider the effect of variability in model types, GHG emission scenarios, and internal variability. A multi-model ensemble using a combination of various model types, RCP scenarios, and initial conditions (i.e., ensemble runs) is developed herein to properly account for the climate-related uncertainties involved in the fatigue propagation prediction.

3.4. Route Selection and Wind Data Analysis

As evidenced by the results available in literature, the effects of climate variability on sea conditions may not be similar across different locations around the globe. Theoretically, ships can choose infinite number of routes between the origin and destination. However, economic and physical constraints limit the number of navigation routes. Identifying the principal ship navigation routes can be achieved by analyzing available ship navigation databases such as those provided by the voluntary observing ship scheme and automatic identification system (AIS) (Kent et al., 2010). In this chapter, the principal trans-oceanic routes in the North Atlantic are identified based on data analysis of the voluntary observing ship scheme. Historical records and future climate prediction models often provide wind

speed data at specific spatial resolutions. At each of the grid points, wind speed information is generally available for west-east and south-north directions. In this chapter, the defined routes are discretized into segments enclosed by four grid points and the available wind information in these grid points is used to project the mean wind speed and wind direction for each segment. The projected wind speed and direction data are next utilized to evaluate the ship heading angle and wave-induced vertical bending moment (VBM).

3.5. Prediction of Ship Hull Loading

Ship hulls are exposed to several types of loads that include dynamic (wave-induced loads), static (still water loads), loading/unloading at harbor, and thermal loads (Decò et al., 2012). Among those, still water and wave-induced bending moments under various sea and cargo conditions are recognized as the most influential load types when evaluating the structural reliability of ship hulls (Guedes Soares & Teixeira, 2000). Accordingly, this chapter considers the effects of still water and the wave-induced dynamic loads on the investigated detail in light of climate change effects. The next subsections provide a brief discussion on the approaches implemented to quantify these loads and their interaction with the ship structure.

3.5.1. Wave-induced Vertical Bending Moment: A Brief Review

The interaction between sea waves and ship hulls can be represented in terms of several structural response parameters such as ship motions, body forces, pressure distribution, and bending moments (Decò et al., 2012). The linear strip theory is commonly used to quantify these structural response parameters (Hansen & Hansen, 1994). This two-dimensional method assumes a linear relationship between ship response and wave excitation. Although this model may not properly represent the ship response at certain sea conditions, it is

widely implemented in research and practice (Bennett et al., 2013; Chen & Zhu, 2010; Veen & Gourlay, 2012). This is mainly due to its computational efficiency and the good agreement with wave-load experimental results in regular sea conditions (Wang, 2000). This chapter adopts the linear strip theory to quantify wave-induced VBM acting on the ship hull.

The response amplitude operator (RAO) is a transfer function that establishes a relationship between the spectral density functions of sea waves and the ship response. This relationship is expressed as (Drummen et al., 2009)

$$S_Y(\omega)=|\mathrm{F}_i(\omega)|^2\, S_x(\omega) \tag{3-1}$$

where $S_Y(\omega)$ is the output spectral density function representing the response of interest, $S_x(\omega)$ is the input spectral density function of sea waves, $\mathrm{F}_i(\omega)$ is the transfer function, and ω is the frequency (rad/s). The RAO is a function of the ship geometry and operational conditions. Several variables such as the sea state, ship speed, and heading angle are involved in defining the operational conditions. To properly account for these parameters, it is essential to evaluate the encountered wave frequency defined as (ABS, 2017)

$$\omega_{e,U,H} = \left|\omega - V\frac{\omega^2}{g}\cos H\right| \tag{3-2}$$

in which $\omega_{e,U,H}$ is the encountered wave frequency (rad/s), V is the ship speed (m/s), g is the gravitational acceleration (m/s^2), and H is the heading angle. In this chapter, the computer program SPECTRA (Michaelson, 2000) is employed to generate the RAOs of the VBM. This program is capable of generating RAOs considering wave-induced (low-frequency) and slam-induced (high-frequency) bending moments associated with vertical, lateral, and torsional conditions (Sikora, 1998).

Due to the stochastic nature of wind, waves induced by wind have irregular heights and periods. A Gaussian random function can describe irregular sea surface with reasonable accuracy (Podgórski et al., 2000); accordingly, at a given location and time, the sea surface elevation may be represented by a normal distribution. Consequently, based on the theory of normal random functions, the wave height can be represented by a Rayleigh type distribution (Li & Cui, 2015; Tupper, 2013). The probability density function (PDF) of the peak wave elevation (A_w) is expressed as (Faltinsen, 1993)

$$f(A_w) = \frac{A_w}{m_o} \exp\left(-\frac{A_w^2}{2m_o}\right) \tag{3-3}$$

where m_o is the area under the spectrum (i.e., zeroth moment of the wave spectrum $S_\omega(\omega)$) given by

$$m_o = \int_0^\infty \omega S_\omega(\omega) d\omega \tag{3-4}$$

The estimation of the sea surface profile using Rayleigh distribution can yield biased results under severe sea states (Janssen, 2015). To overcome this issue, the effect of various parameters that influence the wave spectrum (e.g., wind speed, fetch length, significant wave height, and model frequency) can be incorporated into the wave spectrum as (Bretschneider, 1959)

$$S_\omega(\omega) = \frac{A}{\omega^5} \exp\left(\frac{-B}{\omega^4}\right) \gamma^\partial \tag{3-5}$$

where A and B are scale and shift parameters, respectively, γ is the peak enhancement factor accounting for peak frequency, and ∂ specifies the growth of waves with distance. Several researchers used the Bretschneider (1959) spectrum as a baseline to develop modified formulations for different sea regions. The modified Bretschneider spectrum (i.e., Pierson-Moskowitz spectrum) for fully developed seas in the North Atlantic Ocean

assumes that (a) the spectrum energy only depends on the value of B, (b) A is a function of wind speed, and (c) the peak enhancement factor is equal to one (γ = 1) (Pierson Jr & Moskowitz, 1964). Hasselmann et al. (1973) further modified the Pierson-Moskowitz model to include a new single-peak wave spectrum for fully developed sea, denoted as the JONSWAP spectrum. This spectrum aimed at representing the developing wind-wave sea state in severe conditions. Unlike Pierson and Moskowitz model, JONSWAP model forces the enhancement factor to values not necessarily equal to one. This modification is made to improve the fit to more peaked spectral shapes observed in the fetch-limited wind seas. The JONSWAP spectrum, which can describe partially developed sea states, is defined as (Hasselmann et al., 1973)

$$S_{\omega}(\omega) = \alpha \frac{g^2}{(2\pi)^4} (T)^5 \exp\left(-\frac{5}{4} (\frac{\omega_p T}{2\pi})^4\right) \gamma^{exp\left[-\frac{(\frac{2\pi}{T}-\omega_p)^2}{2\sigma^2\omega_p{}^2}\right]} \tag{3-6}$$

where T is the average wave period (s), ω_p is the frequency at the spectral peak, γ is the peak enhancement factor, σ is the peak shape parameter, α is the Philips constant and it is expressed as a function of the significant wave height (SWH) as $\alpha = 4.5\,(\frac{\omega_p}{2\pi})^4 SWH^{\,2}$ (Ochi, 2003).

After generating the RAOs and sea spectrum parameters, the response spectrum for the wave-induced load effect $S_M(\omega_{e,U,H})$ can be found as (Hughes, 1983; Sikora, 1998)

$$S_M(\omega_{e,U,H}) = \left|\mathrm{F}_i(\omega_{e,U,H})\right|^2 S_{\omega}(\omega_{e,U,H}) \tag{3-7}$$

where, $\mathrm{F}_i(\omega_{e,U,H})$ and $S_{\omega}(\omega_{e,U,H})$ represent RAO for wave-induced VBM and wave spectrum, respectively, given the encountered frequency, wind speed, and heading angle.

Quantifying the response spectrum in Equation (3-7) requires detailed information on encountered waves. However, historical and projected climate data generally provide

wind information. Accordingly, it is necessary to predict wave conditions based on available wind data. Several methods, such as in situ buoy measurements, satellite altimeters, and numerical wave models, can be used to predict wave conditions based on climate data (Agarwal et al., 2013; Kumar & Naseef, 2015; Shi et al., 2021; Stopa & Cheung, 2014). In this chapter, statistical analysis of data obtained from the fifth-generation climate reanalysis dataset (ERA5) is used to establish a relationship between wind and wave characteristics in the Atlantic Ocean. The developed relationship is then used to project wave characteristics (i.e., significant wave height, average wave period, and wave direction) based on the GCM-projected wind data. The ERA5 dataset, developed by the European center for medium-range weather forecasts (ECMWF), provides atmospheric and ocean waves data on 0.25° and 0.5° grids, respectively, with 6 hours of temporal resolution for the period 1976 to 2020 (Hersbach et al., 2019).

3.5.2. Still Water Vertical Bending Moment

In this chapter, the design values of sagging ($M_{sw,sag}$) and hogging ($M_{sw,hog}$) still water bending moments at each cross-section along the ship length are estimated based on IACS (2022) as:

$$M_{sw,sag} = 0.05185 f_{sw} C_{wv} l^2 b (C_b + 0.7) \quad (3\text{-}8)$$

$$M_{sw,hog} = 0.01 f_{sw} C_{wv} l^2 b (11.97 - 1.9 C_b) \quad (3\text{-}9)$$

where f_{sw} is the factor accounting for the variation of VBMs along the vessel length (with 1.0 at midship), C_b is the ship block coefficient, l is the ship length (m), b is the ship breadth (m), and C_{wv} is a wave coefficient calculated as follows (IACS, 2022):

$$C_{wv} = \begin{cases} 10.75 - \left(\frac{300-l}{100}\right)^{1.5} & for\ 150 \le l \le 300 \\ 10.75 & for\ 300 \le l \le 350 \\ 10.75 - \left(\frac{l-350}{150}\right)^{1.5} & for\ 350 \le l \le 500 \end{cases} \quad (3\text{-}10)$$

The still water bending moment is assumed herein to follow a normal distribution with a mean of 63% of the design still water bending moment and a coefficient of variation of 20% (Hørte et al., 2007).

3.6. Fatigue Crack Growth

Two stages are generally involved in estimating the fatigue life of structures subjected to fluctuating loads; namely, the fatigue crack initiation and propagation stages. However, the presence of large number of welded details in ship hulls creates cracks or crack-like conditions that may experience crack propagation when subjected a very low number of cycles (Andersen, 1998). Accordingly, this chapter focuses only on quantifying the effect of climate change on the fatigue crack propagation due to wave-induced loading. For quantifying the service life under propagating cracks, the crack growth rate under constant amplitude loading can be estimated as (Paris & Erdogan, 1963)

$$\frac{da}{dN} = c(\Delta K)^{m_o} \quad (3\text{-}11)$$

where a is the crack size, N is the number of cycles, c and m_o are material constants, and ΔK is the range of the stress intensity factor (SIF), the unit of c assumes units of millimeters for crack size and MPa$\sqrt{\text{m}}$ for ΔK. However, under the effect of stochastic sea waves, ship hulls will be subjected to variable amplitude loading (VAL). The geometry and the interaction between underload and overload cycles can result in a complex stress field near the crack tip (Ding et al., 2017).

Several models can be utilized for predicting crack growth under variable amplitude loading if the load history is known. These include the models proposed by Willenborg (Willenborg et al., 1971), Wheeler (Wheeler, 1972), and Newman (Newman et al., 1999), among others. Several modifications were proposed to improve the capability of Wheeler's model in predicting crack propagation. For example, Yuen & Taheri (2006) applied modifications to Wheeler's model to consider the retardation due to applied overloads, the effect of overload interaction, and the initial crack growth acceleration immediately following an overload. Mehrzadi & Taheri (2013) investigated the influence of the overload ratio on crack growth retardation. Lu et al. (2019) performed a series of experiments to investigate the effect of single tensile overload on the crack growth rate while Shakeri et al. (2021) proposed an extended model that accounts for mixed-mode loading. These models mainly focused on tensile overloading that may cause significant crack growth retardation. However, crack growth acceleration may also occur under the influence of underload and overload-underload interaction (Ding et al., 2017; Doré & Maddox, 2013; Espinosa et al., 2017). Huang et al. (2008) modified Wheeler's model to account for overload, underload, and spectrum loadings. The model also provides a mechanism to account for the effect of load ratio based on an equivalent stress intensity factor range. Hence, the resulting model accounts for the load ratio and the plastic zone size ahead of the crack tip, which makes it suitable for predicting the crack growth on a cycle-by-cycle manner. Accordingly, the model proposed by Huang et al. (2008) is adopted in this chapter to predict crack growth under wave-induced loading.

3.6.1. Fatigue Crack Propagation Model

The expanded plastic zone caused by high overload ratio (OLR) often results in crack retardation (Wheeler, 1972). In addition, in case of very high OLR (i.e., greater than 2 or 3) crack arrest may occur (Taheri et al., 2003). To account for retardation due to the application of an overload cycle within a constant amplitude load profile, the following modified Paris law formulation can be used (Wheeler, 1972)

$$\frac{da}{dN} = C_p(c\Delta K^{m_o}) \tag{3-12}$$

where C_p is a retardation parameter to incorporate the reduced crack growth rate through the expanded plastic zone.

$$C_p = \begin{cases} \left(\frac{r_y}{a_{OL} + r_{OL} - a}\right)^{n1} & a + r_y < a_{OL} + r_{OL} \\ 1 & a + r_y \geq a_{OL} + r_{OL} \end{cases} \tag{3-13}$$

$$r_y = \alpha_o \left(\frac{K_{max}}{\sigma_y}\right)^2 \tag{3-14}$$

$$r_{OL} = \alpha_o \left(\frac{K_{max}^{OL}}{\sigma_y}\right)^2 \tag{3-15}$$

in which r_y and r_{OL} are the plastic zone radii ahead of the crack tip under current maximum stress and maximum stress from prior overloading (mm), respectively, a and a_{OL} are the crack lengths at current and prior overloading events (mm), respectively, α_o is plastic zone size factor, $n1$ is the shaping exponent in Wheeler's model, K_{max}^{OL} represents the maximum SIF associated with prior overload, K_{max} is the maximum SIF at a current load cycle occurring after the overload (MPa$\sqrt{\text{m}}$), and σ_y is the tensile yield stress (MPa). Although Wheeler's Model is capable of modeling the crack growth retardation due to overloads, it

may be inadequate in dealing with the effect of underload and overload-underloads interaction. To account for these effects, Huang et al. (2008) substituted the retardation parameter C_p with a correction factor M_p to account for accelerated crack growth in case of an underload following an overload. The modified model subtracts the plastic zone size increment caused by the underload from the plastic zone size of caused by overload. Figure 3-1 shows a schematic view of the variables associated with the adopted model.

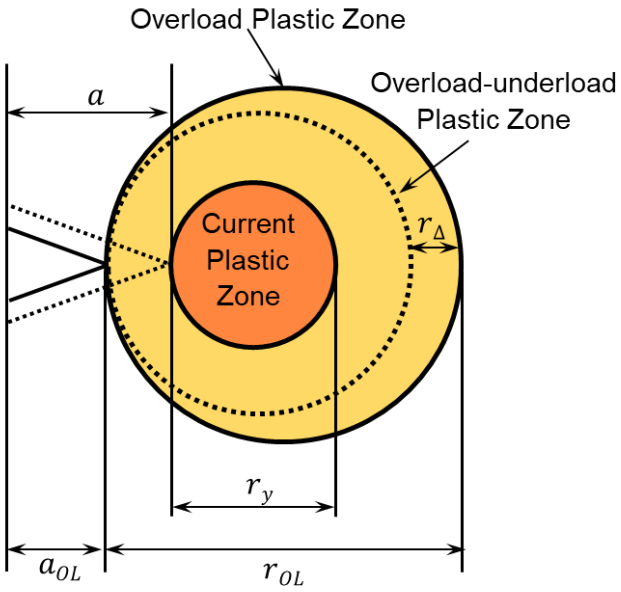

Figure 3-1. Schematic view of the variables in the adopted crack propagation model (Huang et al. 2008)

The correction factor M_p can be computed as (Huang et al., 2008)

$$M_p = \begin{cases} \left(\dfrac{r_y}{a_{OL} + r_{OL} - a - r_\Delta}\right)^n & a + r_y < a_{OL} + r_{OL} - r_\Delta \\ 1 & a + r_y \geq a_{OL} + r_{OL} - r_\Delta \end{cases} \tag{3-16}$$

$$r_\Delta = \alpha_o \left(\frac{\Delta K_u}{\sigma_y}\right)^2 \tag{3-17}$$

$$\Delta K_u = \sqrt{\pi a}\left(\sigma_{min}^{i-1} - \sigma_{min}^{i}\right) \tag{3-18}$$

where n is a shaping exponent determined experimentally, r_Δ is the increment in the plastic zone size ahead of the crack tip caused by an underload following an overload (mm), ΔK_u is the SIF range caused by an underload following an overload (MPa$\sqrt{\text{m}}$), while σ_{min}^{i-1} and σ_{min}^{i} are minimum stresses up to and following the i^{th} overload, respectively (MPa). The plastic zone size factor (α_o) is required for estimating the increment in the plastic zone size due to an underload following an overload. Conditions around the crack tip including the yield stress, maximum applied stress, and specimen thickness contribute to the plastic zone size (Shahani et al., 2020). A continuous function was proposed in Huang et al. (2008) to determine α_o for materials with insignificant hardening properties as

$$\alpha_o = 0.35 - \frac{0.29}{1+\left[\frac{1.08K_{max}^2}{e\sigma_y^2}\right]^{2.15}} \tag{3-19}$$

where K_{max} is the maximum SIF (MPa$\sqrt{\text{m}}$), σ_y is the tensile yield stress (MPa), and e is the plate thickness (mm).

In addition to load sequence effect, load ratio (R) can also affect the fatigue crack growth rate. An equivalent SIF range (ΔK_{eq}) model that converts the crack growth under different R ratios into a single curve scaled to $R = 0$ can be used to calculate crack growth rate under VAL independent of load ratio. The equivalent SIF range at $R = 0$ (ΔK_{eq0}) is calculated as (Huang et al., 2008)

$$\Delta K_{eq0} = M_R M_p \Delta K \tag{3-20}$$

where ΔK is the SIF range (MPa$\sqrt{\text{m}}$), M_p is the correction factor for the loading sequence interaction calculated using Equation (3-16), and M_R is the correction factor for the load ratio calculated as

$$M_R = \begin{cases} (1-R)^{-\beta_1} & -5 \le R < 0 \\ (1-R)^{-\beta} & 0 \le R < 0.5 \\ (1.05 - 1.4R + 0.6R^2)^{-\beta} & 0.5 \le R < 1 \end{cases} \tag{3-21}$$

where R is the load ratio, and β and β_1 are the shaping exponents. Finally, based on this model, fatigue crack propagation rate can be computed as

$$\frac{da}{dN} = c\left[\left(\Delta K_{eq0}\right)^{m_o} - \left(\Delta K_{th0}\right)^{m_o}\right] \tag{3-22}$$

where ΔK_{eq0} and ΔK_{th0} are equivalent and threshold SIF range at $R = 0$, respectively.

3.6.2. Stress Intensity Factor Calculation

The accurate prediction of the SIF range (ΔK) is crucial for properly estimating the fatigue crack growth rate. Closed-form solutions can be used to determine the SIF in simple structural details (Tada et al., 2000). However, given the complexity of ship hull details, this chapter uses the *J*-integral (Rice, 1968) to compute the work per unit fracture surface area and correlates it to the SIF. The *J*-integral can be described as a path independent contour integral in the form of (Rice, 1968)

$$J = \int_{\Gamma} \left(W dy - S_T \frac{\partial u}{\partial x}\right) ds \tag{3-23}$$

where W is strain energy density, S_T is surface tractions vector, u is the displacement vector, Γ is the curve surrounding the crack tip, x and y are the directions parallel and perpendicular to the crack plane, respectively, and ds represents an arc element along Γ.

The *J*-integral and SIF can be related for each of the three fatigue modes (i.e., opening, sliding, and tearing modes). The relationship between the *J*-integral and SIF associated with Mode I loading (i.e., opening mode), which is of interest herein, is

$$K = \sqrt{JE'} \tag{3-24}$$

in which E' is equal to the modulus of elasticity (E) for plane stress and $[E/(1-v^2)]$ for plane strain conditions and v is Poisson's ratio. In this chapter, FE modeling is employed to calculate the *J*-integral given the crack size and applied stresses.

Linear elastic fracture mechanics (LEFM) can be used in cases where the plastic zone size is sufficiently small relative to the crack length and specimens dimensions. In cases where the plastic deformation is significantly large, the effect of the plastic zone on the elastic field should be considered, and the LEFM is no longer applicable. Several approaches have been proposed in the literature to evaluate the applicability of LEFM based on the size of the plastic zone ahead of the crack tip (e.g., Ritchie 1983; François et al. 1999). Other studies utilize the crack tip opening displacement (CTOD) (e.g., Marques et al. 2021) to evaluate the applicability of LEFM assumptions. In this chapter, the approach proposed by Marques et al. (2021) was adopted to ensure that small-scale yielding conditions are applicable. Such conditions are more likely to occur in ship hulls since the crack size and the plastic zone diameter are relatively small compared to the ship dimensions (Dexter & Pilarski, 2002; Dexter et al., 2005; Nussbaumer, 1994; Nussbaumer et al., 1999).

3.7. Performance Function and Probability of Failure

After identifying the wave-induced loads considering future climate variability and conducting the fatigue crack propagation analysis, a performance function is defined to evaluate the failure probability of the ship detail with respect to fatigue. In this chapter, the critical SIF (K_c) is considered as the resistance limit given the vector of random parameters ($\mathbf{X}$), while the equivalent SIF (ΔK_{eq0}), given the vector of random variables ($\mathbf{X}$) and at time t, is considered as the load effect. It is assumed that a failure condition is reached if the

calculated equivalent SIF is larger than the critical SIF. Accordingly, the performance function G at time (t) is

$$G(t) = \Delta K_{eq0}(\mathbf{X}, t) - K_c(\mathbf{X}) \tag{3-25}$$

The performance function is then integrated into a MCS process to compute the probability of exceeding the critical SIF, denoted $P_e(t)$, as

$$P_e(t) = P[G(t) > 0] \tag{3-26}$$

3.8. The Framework for Quantifying Failure Probability Considering Climate Variability

The proposed framework establishes the time-variant failure probability profiles for ships under fatigue loads and variable climate conditions through two interconnected modules. As shown in Figure 3-2, Module I is responsible for generating the loads acting on the ship hull considering climate change. This module defines navigation routes and discretizes them. Wind speed and wind direction data associated with each segment are then adopted from global climate models and/or historical records. Several GCM models, ensemble runs, and RCP scenarios are used to account for uncertainties associated with climate model predictions. The significant wave height and average wave period are then calculated based on the established relationships between the wind and wave characteristics using the ERA5 reanalysis dataset. The sea wave spectrum associated with each climate scenario is then generated using the JONSWAP spectrum (Equation (3- 6)). Next, the RAOs are computed for different operational conditions and utilized to generate the wave-induced VBM spectrum associated with each route and each climate scenario. Finally, the total VBM induced by the waves and still water is used in crack propagation analysis.

Module II is responsible for conducting the crack propagation analysis required for quantifying the fatigue failure probability associated with each of the defined navigation routes. A FE model is developed to generate *J*-integral data given the VBM load levels and crack sizes. Uncertainties associated with material properties and fatigue model parameters are considered through MCS. The calculated SIF level is then compared to the critical SIF value based on the defined performance function (Equation (3-25)). The failure probability is then calculated using Equation (3-26). Finally, this process is iterated for different climate scenarios and the mean failure probability profile is established.

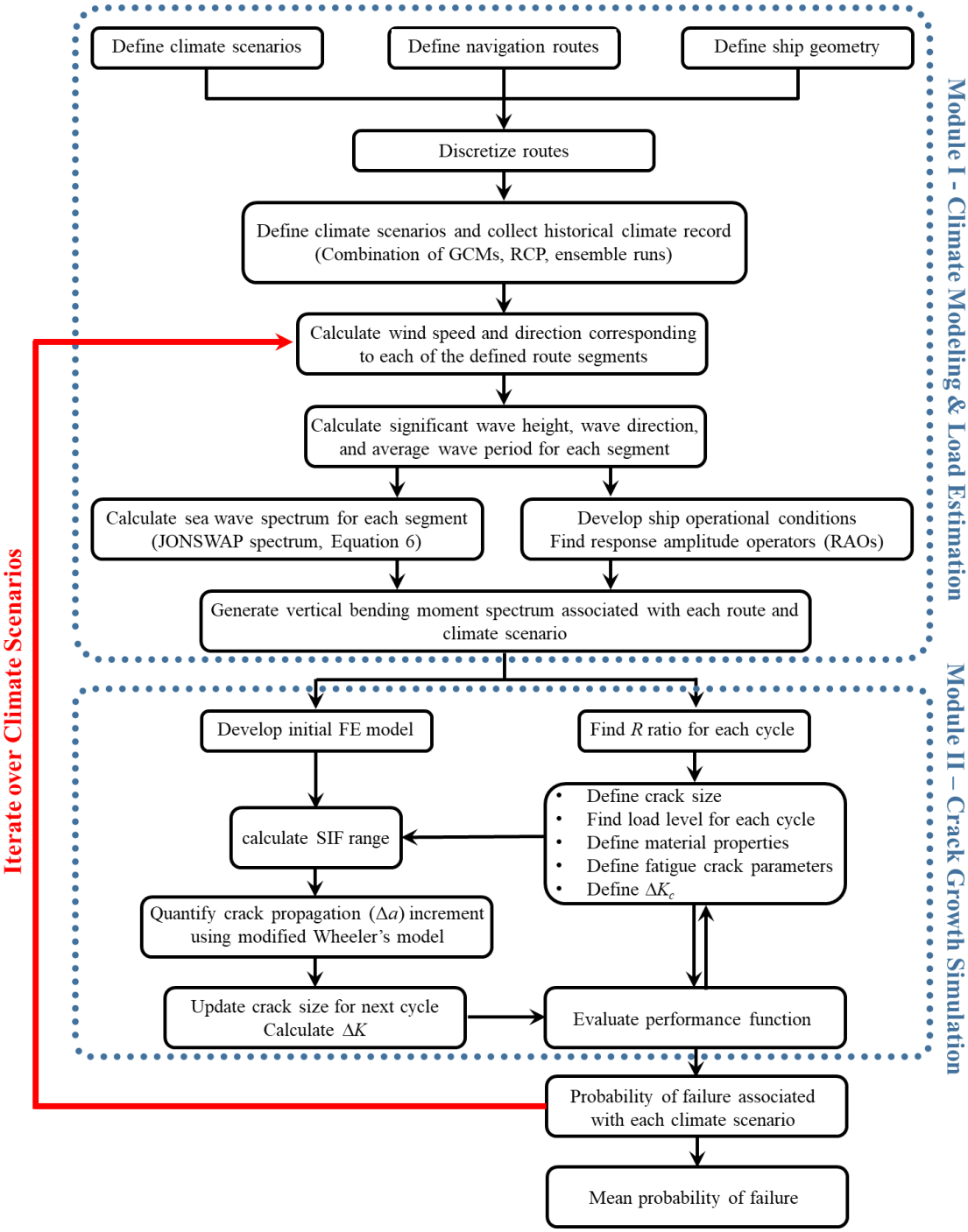

Figure 3-2. Flowchart of the proposed probabilistic approach for quantifying fatigue failure probability considering climate variability.

3.9. Illustrative Example

The proposed framework is illustrated on a tanker ship example adopted from Dinovitzer (2003). The tanker is double-hulled with a beam of 57 m, length of 324.5 m, and depth of 31.2 m. Figure 3-3 shows the mid-ship cross-section of the tanker.

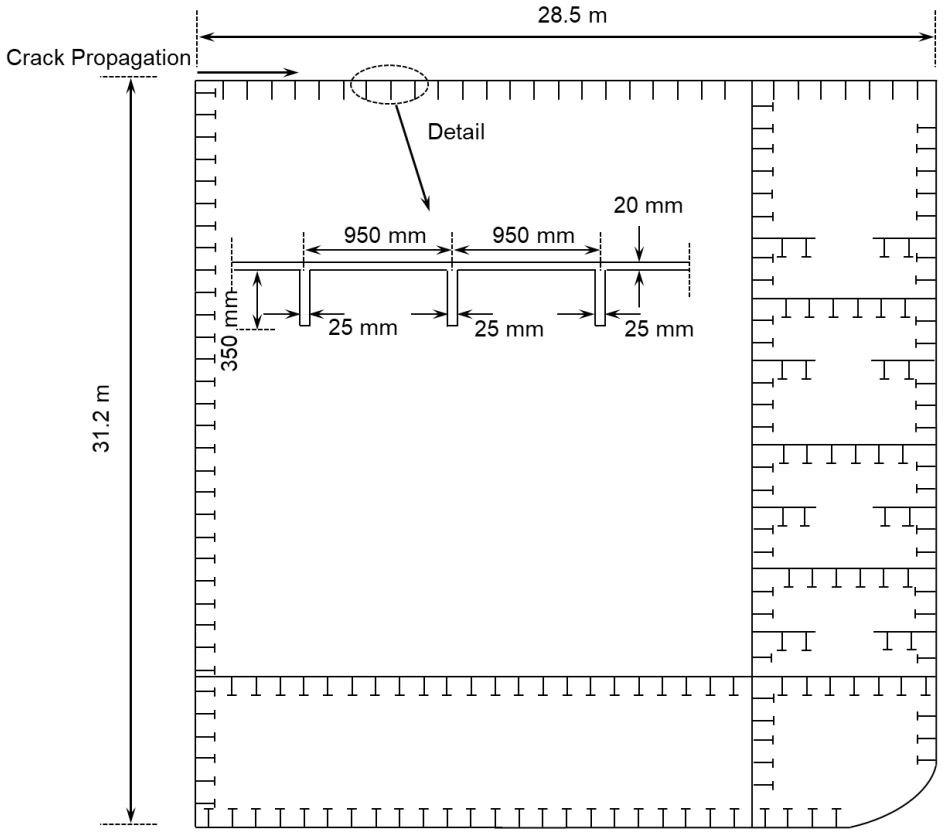

Figure 3-3. View of the midship section of the investigated tanker.

In this example, a center crack at the midsection of the tanker is assumed to propagate from an initial crack size of 2 cm. This value corresponds to the lower bound of the crack sizes that can be detected by visual inspection (Stenseng, 1996). The ship is considered to operate in the Atlantic Ocean with an average speed of 15 knots (Lindstad & Eskeland, 2015). Six principal trans-oceanic passages in the North Atlantic were identified based on data analysis of more than 850,000 ship voyages from 1990 to 2012 (Vettor & Guedes Soares, 2015). Six principal routes identified in Vettor & Guedes Soares (2015), as well as

two additional routes selected in accordance with Rodrigue et al. (2016), are considered for the analysis in this example. The first six routes, which extend from 16.875^{o} N to 47.8125^{o} N and 8.437^{o} E to 73.125^{o} W, are denoted as Routes 1 to 6 and are shown in Figure 3-4. Routes 1 and 3 are identified as the most traveled passages and represent 36% of the traffic in North Atlantic. Routes 4 and 5 carry an estimated 26% of the traffic while Routes 6 and 2 carry 19% and 10% of traffic, respectively. The first additional route (i.e., Route 7) streams between the northwestern of the Atlantic Ocean and northern Europe, while Route 8 connects South Africa to the Caribbean Sea.

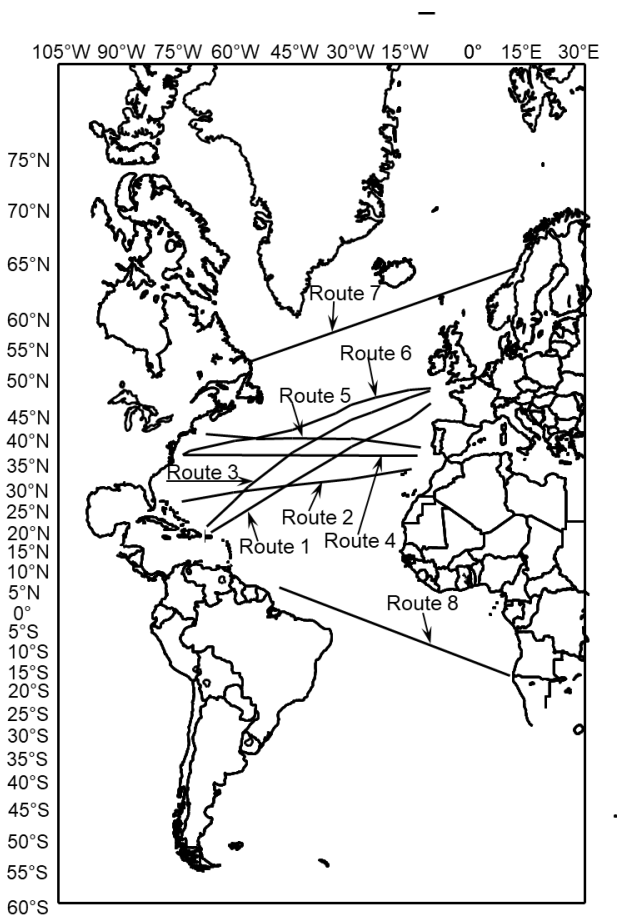

Figure 3-4. The defined ship navigation routes for evaluating the fatigue propagation under climate variability

Historical data from the ERA5 reanalysis dataset (Hersbach et al., 2019) is adopted herein to establish a relationship between the wind and wave characteristics. Recorded wind speed, wind direction, SWH, average wave period, and wave direction in grid points across the Atlantic Ocean are obtained from the ERA5 dataset. The probability density function of the SWH given different wind speeds is calculated. A similar procedure is used to quantify the probability density function of the average wave period based on the recorded SWH and the wave direction given the wind direction, respectively. Figure 3-5(a) presents the established relationship between wind speed and SWH. The PDF of the SWH corresponding to wind speed 16 m/s is shown in this figure. Figure 3-5(b) shows the relationship between the average wave period and the SWH, while Figure 3-5(c) shows the established relationship between the wave and wind directions. The mean (μ), mean minus one standard deviation (STD), and mean plus one standard deviation profiles are shown in this Figure. Based on these established relations, the wave conditions can be determined based on wind characteristics obtained from predicted climate conditions. The wave conditions are utilized next to construct the wave energy density spectrum based on Equation (3-6). For example, wind speeds of 10 and 17 m/s would lead to estimated mean SWHs of 2.2 m and 6.3 m, and average wave periods of 5.3 and 9 s, respectively. Figure 3-6 shows the wave energy density spectrum generated for each of these two wind speeds that, respectively, represent calm, and rough sea conditions defined in Tomita et al. (1995).

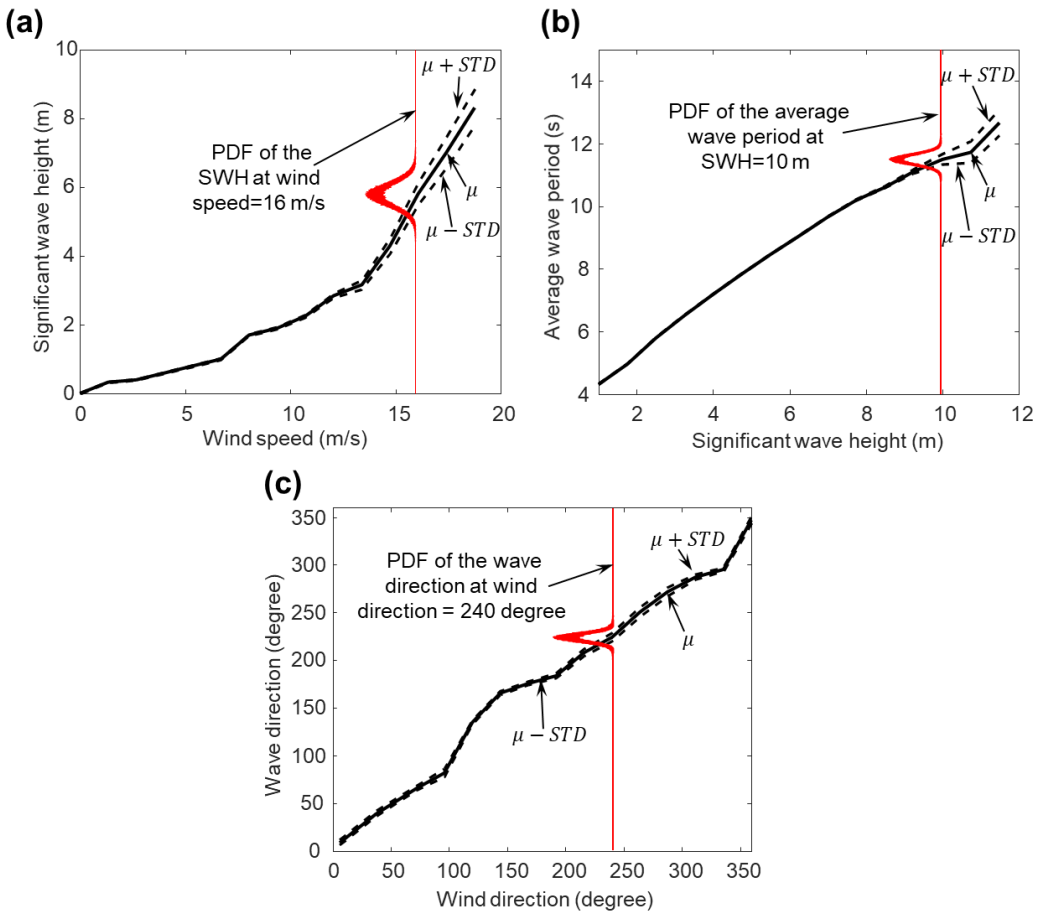

Figure 3-5. The established relationship between the (a) SWH and wind speed (b) average wave period and SWH (c) wave and wind directions

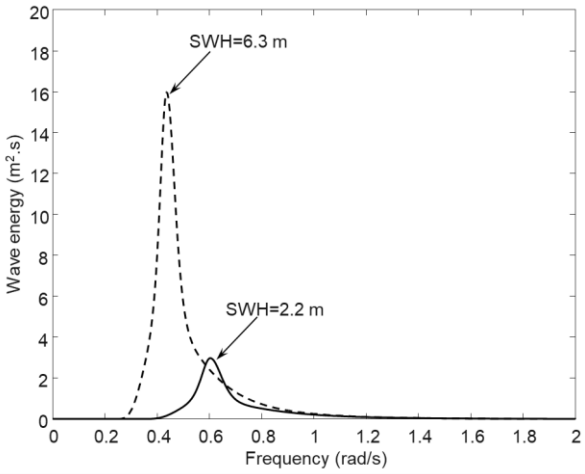

Figure 3-6. JONSWAP wave spectrum corresponding to SWHs of 2.2 m and 6.3 m

Four different GCMs along with RCP 4.5 and RCP 8.5 GHG emission scenarios are adopted from the CMIP5 dataset (Taylor et al., 2012) to project future wind data for each of the defined routes. Table 3-1 presents detailed information regarding the considered climate scenarios. The adopted scenarios provide wind speed data with 6-hours intervals in the west-east and south-north directions. Each of the GCMs provide data with a specific spatial resolution (see Table 1). The adopted wind data is then used to project wave height and period time histories associated with each of the defined routes. The projected wave height time histories along each route can be used to classify the sea condition into calm and rough sea states. Sea states can be characterized by the maximum wave height; a calm state is considered herein when the maximum wave height is lower than 6 m, while a rough state has a maximum height higher than 6 m (Tomita et al., 1995). Figure 3-7(a) depicts the projected sea elevation profile along Route 1 during 2020-2070 timespan using CanESM2 climate model with RCP 8.5. Figure 3-7(b) shows the predicted sea elevation during the year 2032 for the same route while Figure 3-7(c) shows the wave height profile for the same time period. As shown, although the wave height is generally lower than 6 m, aggressive wave conditions can be also seen; especially from February to May.

Table 3-1. adopted CMIP5 climate models

Modeling Center (or group)	Model Name	RCP (W/m^2)	Resolution (lat x lon)	Datasets
Beijing Climate Center, China Meteorological Administration	BCC-CSM1-1	4.5	64 x 128	Eastward wind speed
		8.5		Northward wind speed
Canadian Centre for Climate Modelling and Analysis	CanESM2	4.5	64 x 128	Eastward wind speed
		8.5		Northward wind speed
Model for Interdisciplinary Research on Climate, Japan	MIROC-ESM	4.5	64 x 128	Eastward wind speed
		8.5		Northward wind speed
Norwegian Climate Centre	NorESM1-M	4.5	96 x 144	Eastward wind speed
		8.5		Northward wind speed

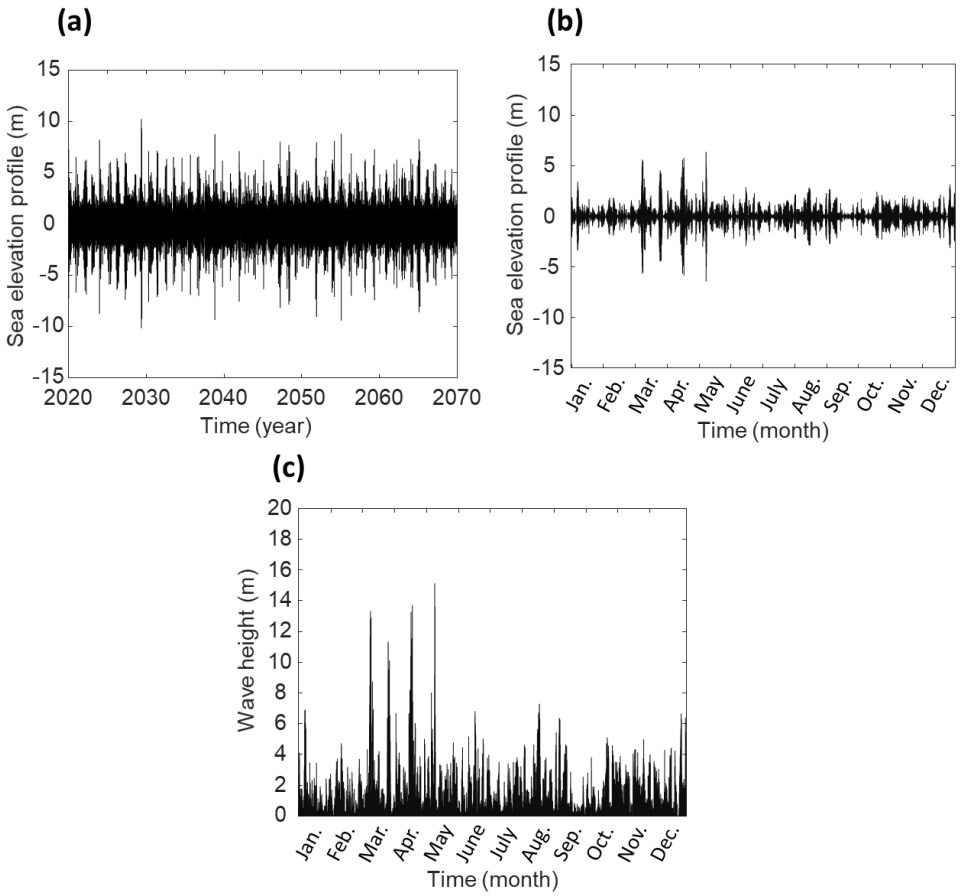

Figure 3-7. Sea conditions on Route 1 predicted using CanESM2 and RCP 8.5: (a) projected sea elevation profile along 2020-2070 timespan, (b) sea elevation during the year 2032, and (c) wave height variation during 2032

3.9.1. Impact of Climate Change on the Wave Height

In order to quantify the effect of climate change on wave conditions in the Atlantic Ocean, the mean and extreme wave heights (95th percentile) projected from 2020 to 2070 are compared to the 50-year historical data which are only available from 1956 to 2006. To better understand the effect of climate change, the ocean is divided into 28 regions extending from 60^{o} S to 80^{o} N. Each of the assumed regions covers 5^{o} of latitudes. Figure 3-8 presents the change in the mean wave height predicted by the adopted GCMs compared to historical data. Subfigures 3-8(a) and 3-8(b) present the results associated with RCP 4.5 and 8.5, respectively. As shown, most of the adopted GCMs with RCP 4.5 and RCP 8.5

project small fluctuations (in range of ±5 cm) in the mean wave height for the zones covering 40^{o} S to 35^{o} N. The considered GCMs consistently project a decrease in the mean wave heights that ranges from 0 to 15 cm for regions covering 35^{o} N to 70^{o} N. However, regions extending from 70^{o} N to 75^{o} N and 75^{o} N to 80^{o} N can experience an increase in the mean wave height that ranges from 0 to 5 cm and 5 to 10 cm, respectively. The majority of the adopted climate scenarios project an increasing trend for regions covering 40^{o} S to 60^{o} S. The increase in the mean wave height for some models can reach up to 15 cm. Figures 3-9(a) and 3-9(b) show, respectively, the projected change in the 95th percentile wave height associated with RCP 4.5 and 8.5. As shown, all GCMs with RCP 4.5 and RCP 8.5 consistently project a decreasing 95th percentile wave height for the regions covering 45^{o} S to 70^{o} N. In contrary, most of the adopted GCMs project an increase in the 95th percentile wave heights for regions covering 45^{o} S to 60^{o} S and 70^{o} N to 80^{o} N.

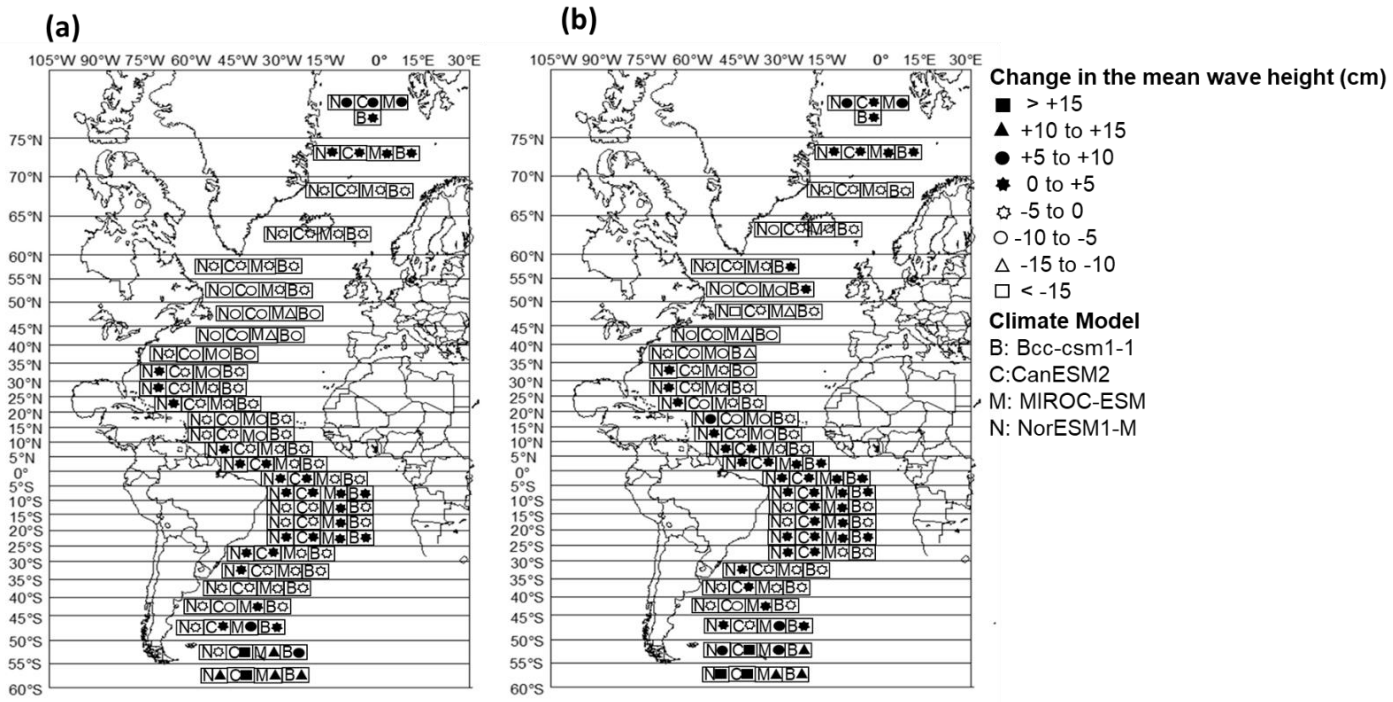

Figure 3-8. Change in the mean wave height projected for 2020 to 2070 with respect to the 50-year historical records using the forcing scenarios: (a) RCP 4.5 and (b) RCP 8.5

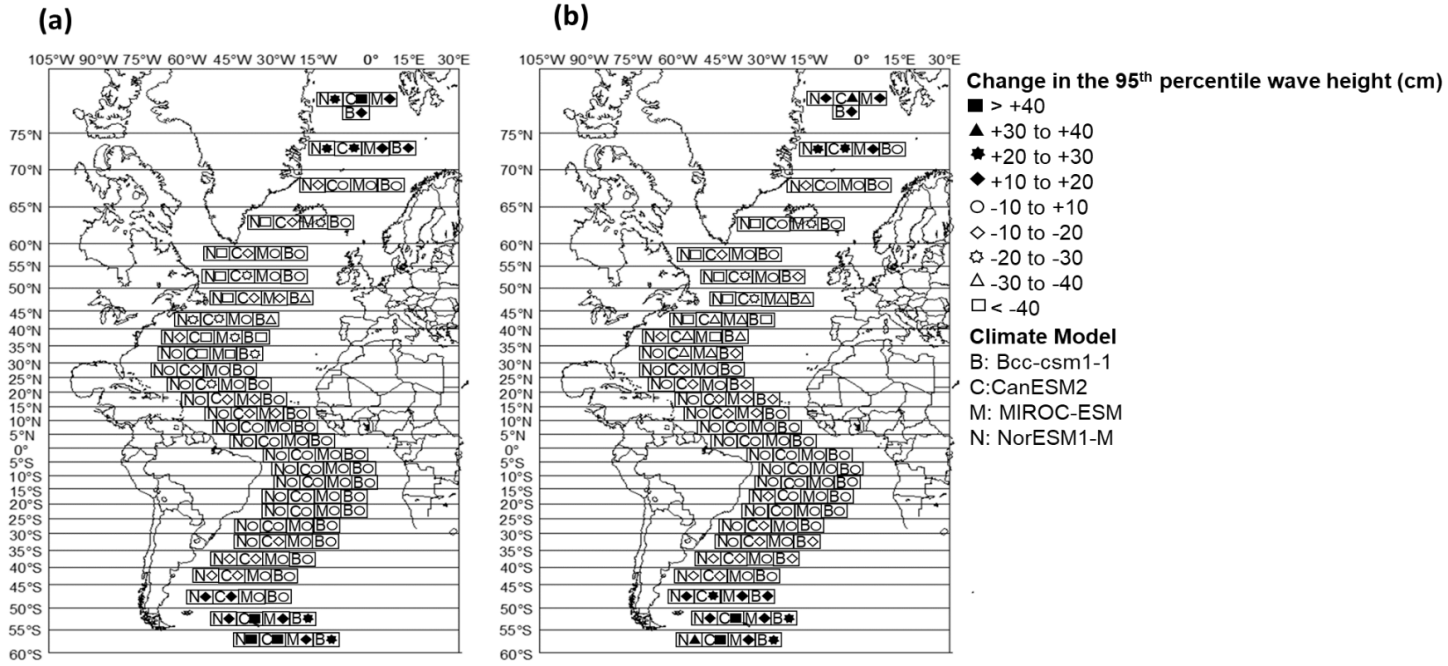

Figure 3-9. Change in the 95th percentile wave height projected for 2020 to 2070 with respect to the 50-year historical records using the following forcing scenarios: (a) RCP 4.5 and (b) RCP 8.5

3.9.2. Projected Change in the SWH and Sea Conditions

The average significant wave height and the number of days with rough sea conditions per year are next calculated for each of the defined routes. The results generated using GCM projections ranging from 2020 to 2070 are compared to those established based on the 50-year historical records collected from 1956 to 2006. As shown in Figures 3-10 and 3-11, the adopted climate scenarios project a decrease in the average SHW and the average number of days with rough sea conditions per year for Routes 1 to 6. This is also consistent with the results presented in Figures 3-8 and 3-9, where decreasing trends were observed in tropics and subtropics in the northern hemispheres. Models with both RCP 4.5 and RCP 8.5 forcing scenarios projected a decrease in the SWH and number of days with rough sea conditions along these routes. It should be noted here that models with RCP 8.5 forcing scenario consistently project a slightly larger decrease than models with RCP 4.5 forcing. In contrary, the comparison for Routes 7 and 8 shows that both RCP 4.5 and 8.5 forcing scenarios project an increase in the mean SWH and number of days with rough wave conditions. In both routes, RCP 4.5 projects the highest values for these two parameters. This projection is also consistent with the results depicted in Figures 3-8 and 3-9. In summary, it is evident that climate change may favorably affects the wave conditions along Routes 1 to 6 while Routes 7 and 8 may experience unfavorable conditions compared to historical wave data.

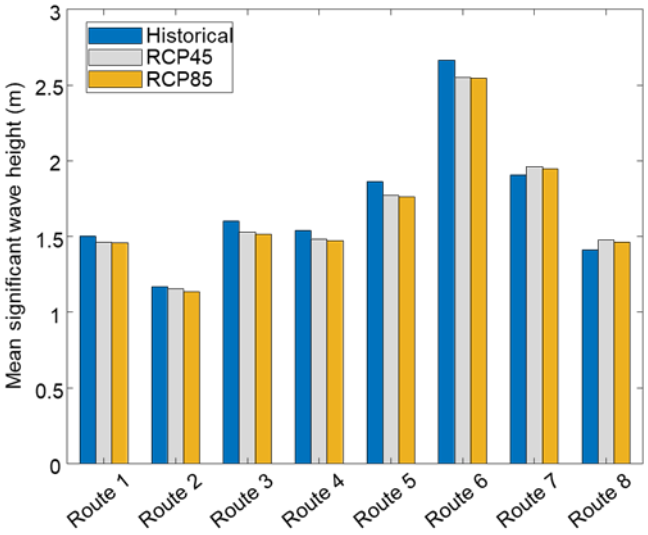

Figure 3-10. Comparison of the mean significant wave height projected using RCP 4.5 and RCP 8.5 forcing scenarios with the historical data along different routes

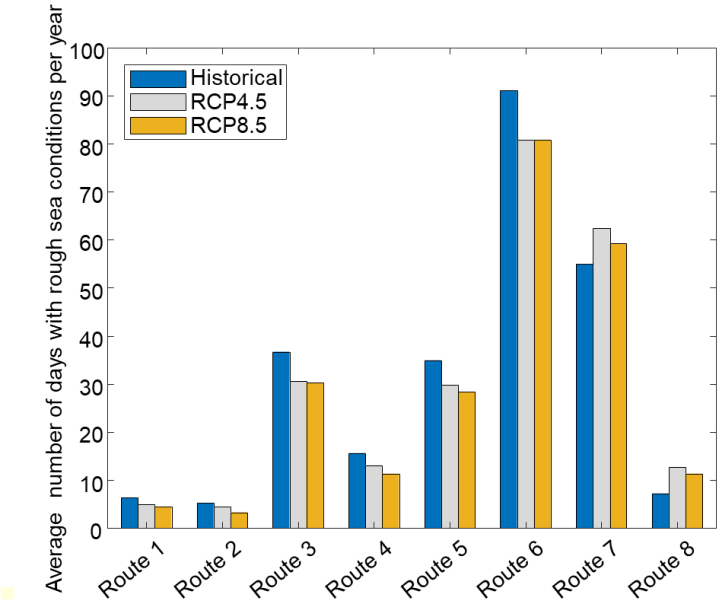

Figure 3-11. Comparison of the average number of days with rough sea conditions per year projected using RCP 4.5 and RCP 8.5 forcing scenarios with the historical data along different routes

3.9.3. Vertical Bending Moment

Three periods covering time spans 2020 to 2050, 2030 to 2060, and 2040 to 2070 are defined to evaluate the effect of climate change on the fatigue crack propagation. Available climate information for the time period 1976 to 2006 is used to generate the historical VBM profiles. These time periods are chosen to represent an average 30 years of service life. Data corresponding to each of the defined routes are extracted from the historical records and GCM predictions. The historical data are adopted in grid locations and time intervals similar to GCM data. Each route is discretized with respect to the spatial resolution of the climate data, as explained in Section 3.4 of this chapter. The west-east and south-north wind data are used to find the resultant wind speed and direction data along each route. The wind data along the navigation direction associated with each route are then used to generate the heading angles and the corresponding RAOs. Wave-induced VBM profiles are next established, as explained in Section 3.5 of this chapter. Figure 3-12(a) shows the generated wave-induced VBM along Route 1 during 2020-2050 timespan using CanESM2 climate model with RCP 8.5 while Figure 3-12(b) shows the predicted wave-induced VBM during 2032. The load effects induced by still water in terms sagging and hogging VBM are evaluated as discussed in Section 3.5 of this chapter. The total load effects are used next in the crack propagation analysis.

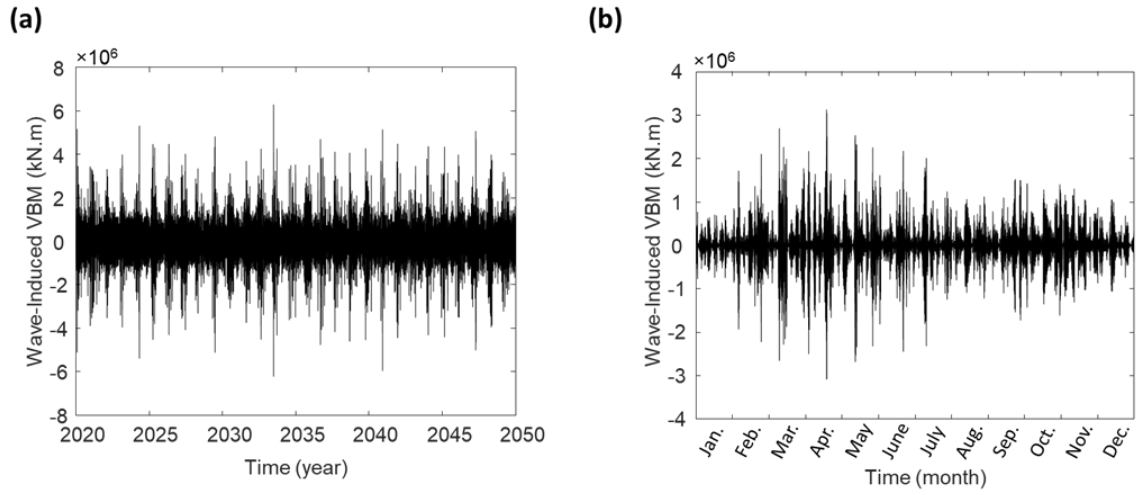

Figure 3-12. Projected wave-induced VBM along Route 1 using CanESM2 climate model with RCP 8.5 during (a) 2020-2050 timespan and (b) the year 2032

3.9.4. Fatigue Crack Propagation and Failure Probability

The crack propagation model given by Equations (3-16) to (3-22) is adopted for predicting the crack growth. The wave induced VBM profiles generated using historical wind data (1976 to 2006) and GCM data (2020 to 2050, 2030 to 2060, and 2040 to 2070 time periods) and still water VBM together are used to predict the crack propagation and quantify the probability of exceeding the critical SIF. In order to estimate the SIF corresponding to different load levels and crack sizes, the cross-section of the ship is simulated using a 3-D model in ABAQUS environment (Hibbitt et al., 2013). The geometry of the model follows the dimensions in Figure 3-3 and a view of the model is shown in Figure 3-13. The main structural components (i.e., stiffeners and plates) are modeled using reduced integration four-node shell elements (i.e., S4R element). The loading (i.e., VBM) and boundary conditions are applied as shown in Figure 3-13. The boundary conditions are applied at two points (i.e., Point A and Point B on Figure 3-13) along the neutral axis of the cross-sections (Decò, 2013). The translation about *x*, *y*, and *z* directions, as well as the rotation around the *z*-axis are prevented at point A, while only translation about *x* and *y* axes is

prevented at point B. The VBM is applied about the x-axis at point B as shown in Figure 3-13. Elastic-perfectly plastic behavior is assumed for the high strength steel material (350WT) (CSA, 2004) with the properties given in Table 3-2.

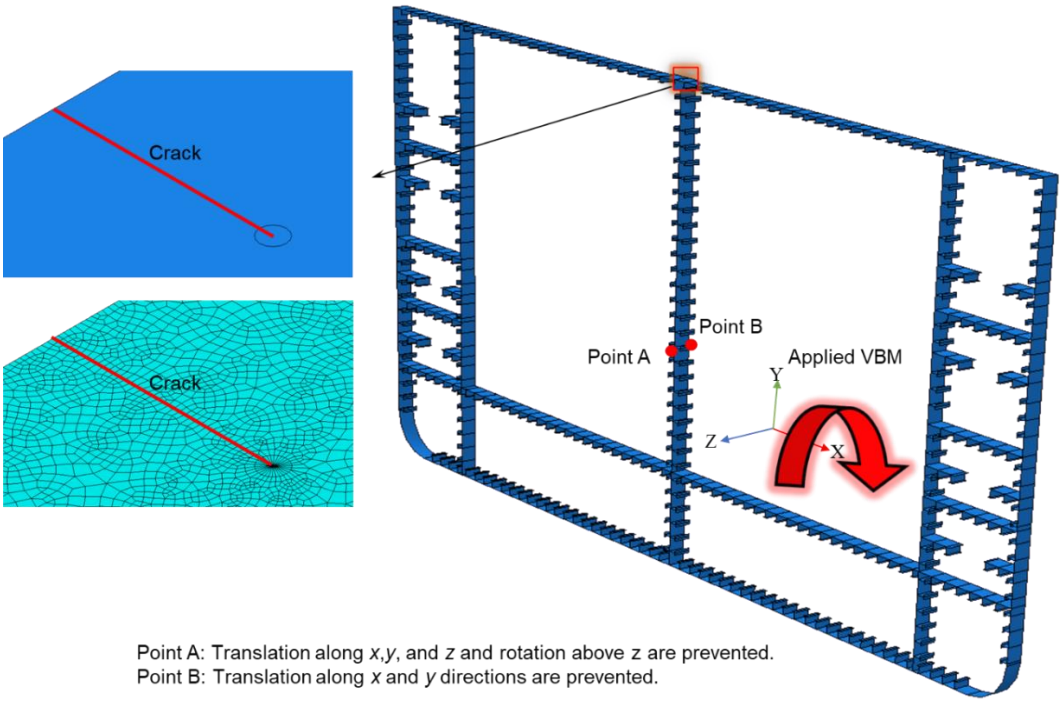

Figure 3-13. Visualization of the developed FE model, the defined constraints, the applied VBM, and the mesh surrounding the crack tip.

The contour integral estimate in ABAQUS is used to quantify the *J*-Integral. This method is often used to study the crack tip behavior in quasi-static problems by constructing rings of elements around the crack tip (Brocks & Scheider, 2001). Figure 3-13 shows a visualization of the mesh surrounding the crack tip. To ensure that the obtained SIF is accurate with reasonable computational cost, convergence analysis is conducted for the mesh around the crack tip. Figure 3-14 shows the SIF values against the number of elements around the crack tip. As shown, further mesh refinement beyond approximately 25 elements achieves a negligible change in the results. Accordingly, 30 elements were

used around the crack tip. This is equivalent to an element size (i.e., arc length) of approximately 1 mm and an element size of 4 mm was used elsewhere in the model.

Table 3-2. Crack propagation prediction parameters

Variable	Distribution Type	Mean	COV	Reference
m_o*	Normal	3.1	0.1	(DNV, 1984)
c*	Normal	$6.8\text{x}10^{-9}\frac{mm}{cycle.(\text{MPa}\sqrt{\text{m}})^{m_o}}$	0.055	(Barasom & Rolfe, 1987, DNV, 1984)
K_c	Normal	44 MPa$\sqrt{\text{m}}$	0.18	(Albrecht & Yazdani, 1986)
ΔK_{th0}	Deterministic	10 MPa$\sqrt{\text{m}}$	------	(Huang et al., 2008, Taheri et al., 2003)
σ_y	Lognormal	344 MPa	0.083	(Hess et al., 2002)
E	Normal	200,000 MPa	0.076	(Hess et al., 2002)
β	Deterministic	0.3	------	(Huang et al., 2008)
β_1	Deterministic	0.5	------	(Huang et al., 2008)
n_1	Deterministic	0.5	------	(Huang et al., 2008)

* Correlation coefficient between c and m_o is -0.95 (Chung, 2004)

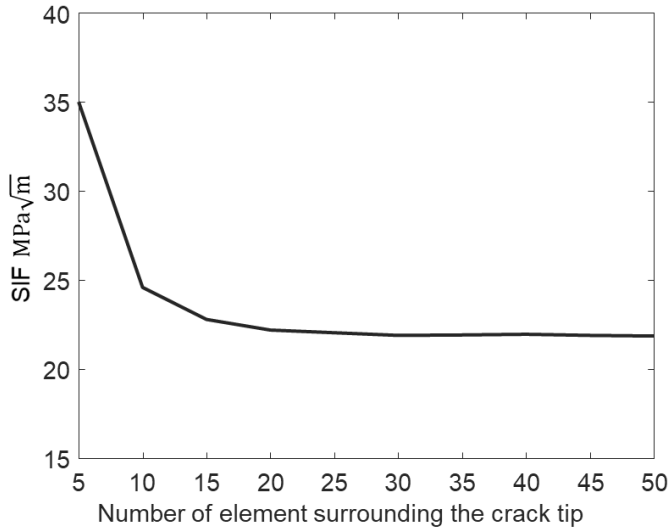

Figure 3-14. Convergence analysis of the SIF with respect to the number of elements around the crack tip.

A MATLAB script is used to iteratively execute the FE model under each particular combination of crack size and VBM and calculate the *J*-integral values. Then, the *J*-integral

is converted to SIF using Equation (3-24). Finally, calculating the equivalent SIF (ΔK_{eq0}) and the crack propagation increment is performed as described in Section 3.6. Figure 3-15 shows the calculated equivalent SIF (ΔK_{eq0}) along Route 1 during 2020-2050 timespan using CanESM2 climate model with RCP 8.5. For this example, the CTOD is measured under the maximum applied load and crack size (i.e., 50 cm) and the elastic and plastic components of the CTOD are calculated. It was found that the ratio between the elastic CTOD and the total CTOD is 87% at maximum load. Since this ratio is higher than 75%, small-scale yielding condition occurs and linear elastic fracture mechanics can be used to assess the crack growth (Marques et al., 2021). To properly account for the uncertainties associated with fatigue life prediction, the material constants c and m_o as well as the critical SIF (K_c) are defined as random variables. The statistical descriptors of the considered random variables are presented in Table 3-2. MCS is then executed, and random samples associated with the defined random variables are used to calculate the equivalent SIF (ΔK_{eq0}) corresponding to individual load profiles and random samples. The crack size growth increment is calculated using Equation (3-22) and the process is iterated to predict the crack growth profile associated with each sample in the vector of random parameters. Figure 3-16 shows the crack growth profile along Route 1 using the projected VBM for all of the available GCMs and considering the uncertainties associated with the material constants c and m_o. The mean, mean minus one standard deviation, and mean plus one standard deviation profiles are also shown in the figure. PDF of crack size after 15 years is also shown in the figure.

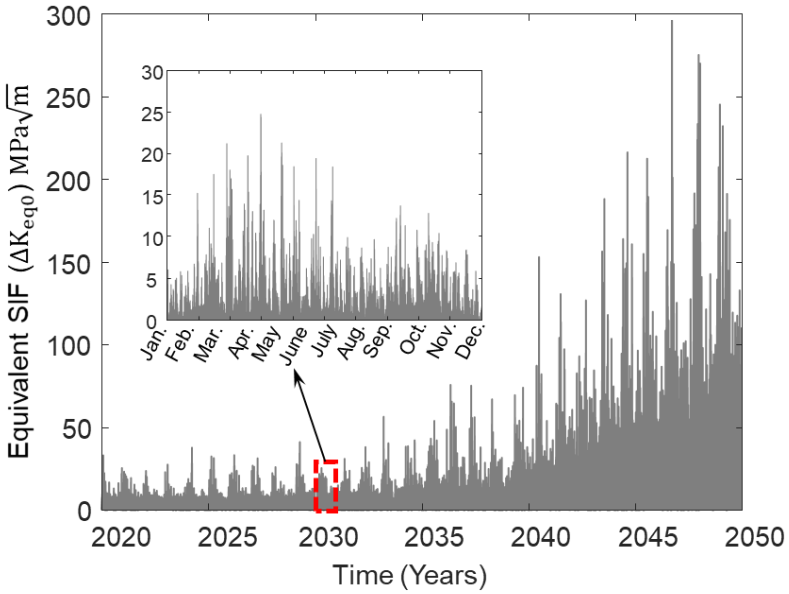

Figure 3-15. The equivalent SIF (ΔK_{eq0}) along Route 1 during 2020-2050 timespan using CanESM2 climate model with RCP 8.5 forcing scenarios.

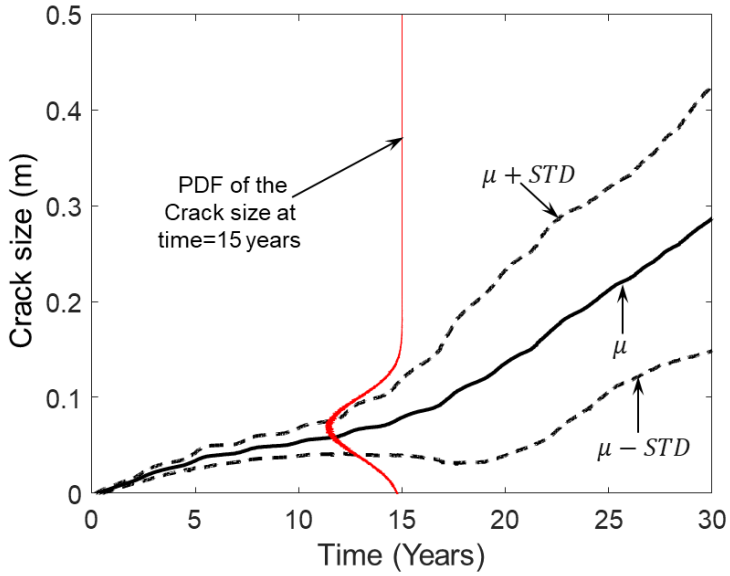

Figure 3-16. The generated crack growth profiles along Route 1 during a 30 years period starting from 2020 and considering the uncertainties associated with climate models and material properties

3.9.5. Impact of Climate Change on the Fatigue Crack Propagation

In order to evaluate the potential effect of climate change on the fatigue crack propagation, VBM projected using historical wind data ranging from 1976 to 2006 and GCM wind data associated with 2020 to 2050, 2030 to 2060, and 2040 to 2070 time periods are used to conduct a comparative analysis. Future GHG emission scenarios represented by RCP 4.5 and RCP 8.5 are considered in this analysis. Figure 3-17 compares the projected fatigue crack growth using the 30-year historical and GCM-provided wind data starting from 2020 for all of the considered navigation routes. As shown, in comparison to historical data, the RCP 4.5 and RCP 8.5 scenarios project lower crack propagation rate along Routes 1, 3, 4, and 5. In contrary, GCM data result in accelerated crack propagation in routes 2, 6, 7, and 8. A similar trend has been also observed when the service life starts in 2030 and 2040. Table 3-3 presents the time required for the crack to propagate from 2 cm to 15 cm in each route based on historical and climate scenarios with different RCP forcing scenarios and start dates. The ratios between the average time required for reaching 15 cm crack size using climate prediction and historical data along each route and each climate scenario are also presented in the table. The average crack propagation time corresponding to each climate scenarios, listed in the utmost right column of Table 3-3, is calculated based on the probability of operation in each route during the service life (Vettor & Guedes Soares, 2015), while all climate scenarios are considered equally weighted in calculating the average time for crack propagation associated with each route (i.e., data in bottom row). As shown, in routes 1, 3, 4 and 5, the time required for 15 cm crack growth increases, while in routes 2, 6, 7, and 8 it decreases. In summary, the results indicate that the effect of the climate change on the crack propagation depends on the navigation route. While some

routes displayed an increase in the crack growth activity, others showed up to 8% reduction in the crack propagation time.

Table 3-3. Time required for 0.15-meter crack propagation in each route based on historical and climate scenarios with different RCP forcing and start dates

Dataset	Time required for 0.15-meter crack propagation								Projection/ Historical (for each climate scenario)
	Route 1	**Route 2**	**Route 3**	**Route 4**	**Route 5**	**Route 6**	**Route 7**	**Route 8**	
Historical (1976-2006)	17.7	23.2	16.6	17.7	19.1	15.3	19.1	23.6	-
RCP 4.5 (2020-2050)	19.6	21.1	17.9	20.8	21.1	14.7	18.7	20.7	1.05
RCP 4.5 (2030-2060)	20.7	22.6	17.3	20.7	21.6	14.9	18.2	22.2	1.07
RCP 4.5 (2040-2070)	19.5	22.1	17.1	18.1	20.1	14.3	17.2	22.1	1.02
RCP 8.5 (2020-2050)	20.2	18.9	17.2	18.0	19.6	13.2	18.1	21.1	0.99
RCP 8.5 (2030-2060)	21.3	21.7	17.5	20.6	20.9	15.0	18.2	22.5	1.07
RCP 8.5 (2040-2070)	20.8	21.8	19.2	19.7	19.4	16.1	17.6	22.6	1.07
Projection/ Historical (for each route)	1.15	0.92	1.07	1.11	1.07	0.96	0.94	0.93	

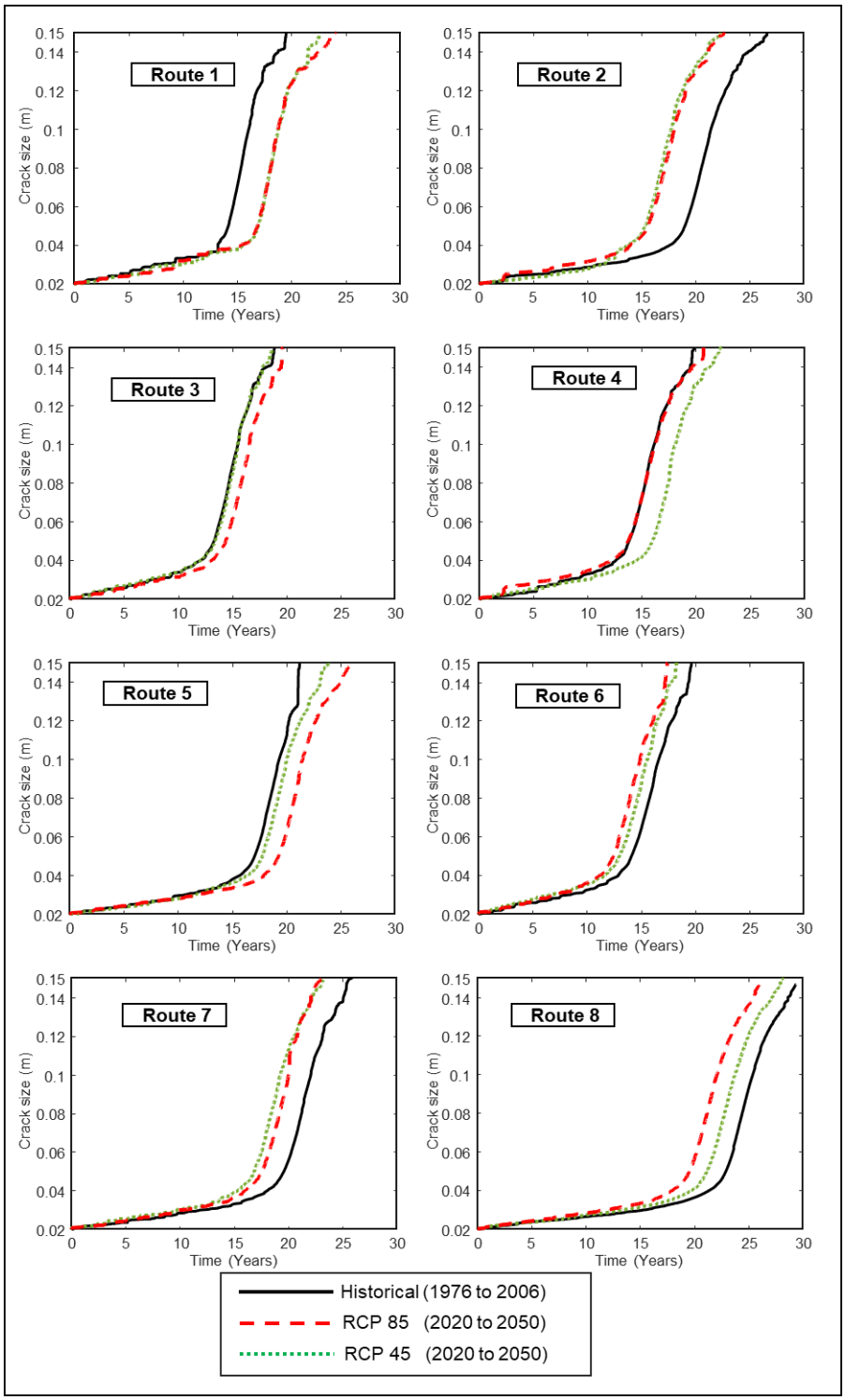

Figure 3-17. Comparison of the projected fatigue crack growth using 30-years historical and GCM-provided wind data starting from 2020 for all the considered navigation routes

The long-term failure probability of the investigated ship operating in the North Atlantic Ocean is also calculated in this chapter. It is assumed that the ship randomly navigates between Routes 1 to 6. The number of voyages corresponding to each route is defined in accordance with navigation data reported in Vettor & Guedes Soares (2015). After conducting the crack propagation given the estimated loads and the associated set of random variables, the performance function is evaluated using Equation (3-25). The probability of exceeding the critical SIF K_c is then calculated using Equation (3-26). Figures 3-18(a) and 3-18(b) present the failure probability given RCP 4.5 and RCP 8.5 forcing scenarios, respectively. As shown in both figures, climate change projections estimate a reduced average failure probability compared to historical records. However, it should be noted that only Routes 1 to 6 are included in the analysis to generate these failure probability profiles. The inclusion of other routes is expected to change this observation.

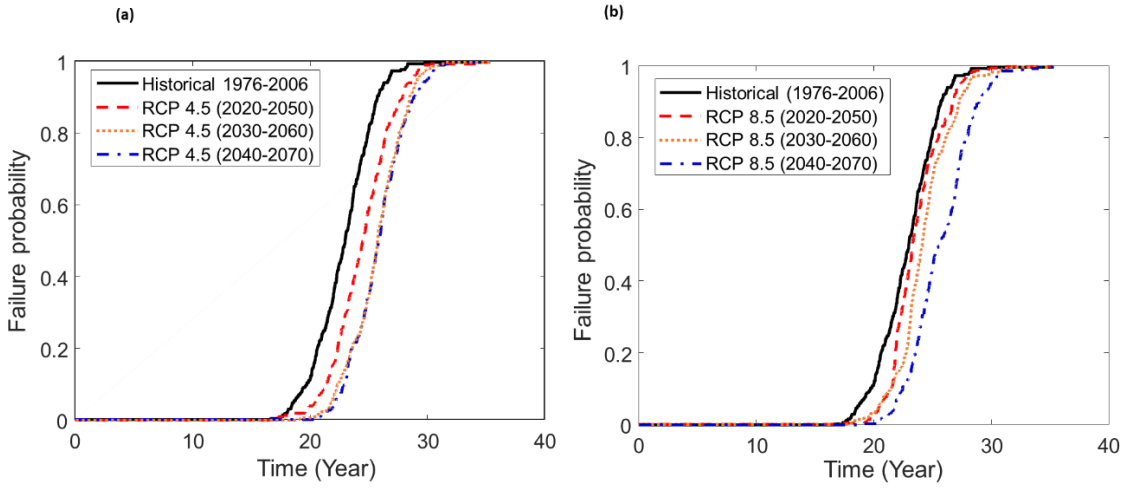

Figure 3-18. Comparison of the failure probability profiles generated using historical data and GCM models with (a) RCP 4.5 (b) RCP 8.5 forcing scenarios

3.10. Conclusion

This chapter presented a probabilistic framework for quantifying the effect of climate change on crack propagation characteristics in ships. The long-term variability in wind-induced waves were projected using global climate models. West-east and south-north wind data were adopted from the CMIP5 archive. The change in the mean and 95th percentile wave heights due to climate variability were projected across the Atlantic Ocean. A probabilistic fatigue crack propagation approach was developed to properly consider the uncertainties associated with material properties and climate-related loading conditions. Eight different routes across the Atlantic Ocean were selected to quantify the effect of climate change on the fatigue crack propagation under future climate conditions. Finally, time-variant failure probability profiles based on historical and GCM-provided climate data in the North Atlantic were generated and compared. The following conclusions were drawn:

- The proposed framework is capable of quantifying the long-term effects of climate change on the VBM and the fatigue crack propagation in ship hulls.
- Analysis of the projected GCM data indicates that tropical regions of the Atlantic Ocean in both southern and northern hemispheres will experience small deviations in mean and extreme wave heights compared to historical records. However, subtropical regions in the southern hemisphere show a decreasing trend in the mean and 95th percentile wave heights. A decreasing trend in mean and extreme wave heights in subtropics and temperate in the northern hemisphere is also observed. In contrary, most of the adopted GCMs projected an increase in the mean and 95th percentile wave heights for regions covering 45^{o} S to 60^{o} S and 70^{o} N to 80^{o} N.

- The fatigue crack propagation results under the defined climate scenarios show that the effect of climate change highly depends on the navigation route. While some routes displayed an expected increase in the fatigue service life, others showed a reduction that can reach 8%.
- Analysis of the impact of climate change on the failure probability of the investigated ship shows that the projected average failure probability associated with Routes 1 – 6 is lower than that resulting from the historical records. However, the failure probability for individual navigation routes can be lower or higher in comparison to the one associated with historical records. Accordingly, the expected navigation routes for a specific ship should be considered in the long-term life-cycle analysis aiming at estimating and/or reducing the fatigue failure probability of the ship.

CHAPTER IV

SENSITIVITY ASSESSMENT OF THE CRACK PROPAGATION BEHAVIOR IN WELDED STIFFENED PANELS

4.1. Overview

Welded stiffened panels play an integral role in maintaining the strength, stability, and lightweight characteristics of marine vessels. The presence of stiffeners can also assist in extending the service life of the structure under propagating cracks. In this context, the proper quantification of the effect of various input parameters on the fatigue crack propagation, especially those associated with the geometry of the stiffened panels, is crucial to accurately predict the service life. This chapter quantifies the influence of relevant input parameters, covering geometric and mechanical properties, on the crack propagation behavior and fatigue service life of welded stiffened panels. The geometric parameters include the main panel thickness and stiffener characteristics while the mechanical properties cover the crack propagation regression parameters, modulus of elasticity, and yield strength. 3-D FE analysis, artificial neural networks, and an elastic-plastic crack advancement rule are integrated to predict the crack propagation profiles. Variance-based sensitivity analysis is conducted to evaluate the effect of the variability in the considered input parameters on the variance of the fatigue service life of these panels. Finally, MCS is utilized to quantify the fatigue reliability of these panels considering

uncertainties associated with different sets of input parameters. It was found that neglecting uncertainties in geometric parameters can lead to unconservative estimates of fatigue reliabilit

4.2. Background

Predicting the crack propagation behavior in welded stiffened panels, commonly found in marine, civil, and aerospace structures, has been especially challenging. The presence of welded stiffeners creates complex stress conditions that need to be properly considered while predicting the crack growth. Variable amplitude loading applied to these structures also leads to sequence and interaction effects that cannot be neglected while predicting the crack growth (Murthy et al., 2007). In addition, as the cracks propagate transversally through the main plate (i.e., main panel), they also propagate through the welds and the stiffeners leading to the presence of multiple crack tips; each with its own stress and crack tip conditions. Furthermore, since these panels are generally designed for relatively low stress levels at service load conditions, load redistribution to adjacent uncracked, low-stressed stiffeners can easily be achieved leading to high levels of structural redundancy. As a result, the panel geometry, including main panel thickness and stiffener attributes (i.e., shape, spacing, and dimensions), play a significant role in the fatigue crack propagation behavior. Although the cracks under these conditions can grow significantly before sudden fracture would occur (Nussbaumer et al. 1999), predicting the crack growth still represents a challenge and requires an integral approach capable of accounting for the load redistribution and interactions, elastic-plastic crack tip conditions, and the presence of residual stresses.

Research on crack propagation in stiffened panels has been active since the 1960s. Poe Jr (1969, 1971) conducted an experimental analysis to study the fatigue crack growth

in aluminum alloy panels with riveted and integral stiffeners. The studies showed that the fatigue crack growth rate is significantly lower when riveted stiffeners were included as compared to unstiffened panels. Nussbaumer et al. (1999), Dexter & Pilarski (2002), and Mahmoud & Dexter (2005) conducted a series of experimental investigations to characterize the crack propagation behavior in welded stiffened panels with different stiffener configurations and load patterns. They also developed analytical models, validated through numerical analysis, to calculate the stress intensity factor considering the effects of stiffener restraint, severed stiffeners, and residual stresses. The predicted crack growth profiles resulting from these models were generally in good agreement with experimentally obtained profiles.

Despite the large number of experimental studies aiming at investigating fatigue cracking in stiffened panels, the high cost of conducting the experimental testing and the long duration of these tests limit the number of test samples and parameters that can be investigated in each study. As a result, it becomes difficult to experimentally characterize the effect of relevant input parameters on the behavior and it is even more challenging to understand the role of uncertainty in input parameters on the behavior. In general, errors in validating the numerical and/or analytical crack propagation prediction models are usually attributed to the aleatoric uncertainties associated with the parameters affecting the crack propagation or epistemic uncertainties of the crack propagation models. Due to these uncertainties, fatigue tests performed under similar conditions often yield different results. Accordingly, probabilistic approaches are essential in evaluating the performance and reliability of structures with stiffened panels under the presence of cracks.

Probabilistic analysis and reliability quantification can help formulate optimal design configurations and plan for inspection, maintenance, and repair activities. The reliability of welded stiffened panels under growing cracks has been investigated in literature. For instance, Feng et al. (2012) and Huang et al. (2013) developed probabilistic approaches to evaluate the fatigue reliability of stiffened panels in the presence of correlated growing cracks. The first-order reliability method (FORM) was utilized to quantify reliability while accounting for the variability in the initial crack sizes and several mechanical properties. Mahmoud & Riveros (2014) implemented numerical analysis to predict the crack growth in stiffened panels under uncertainty and quantified the reliability using Monte Carlo simulation. The variability in the applied load, residual stresses, and the crack propagation regression parameters were considered intheir approach. A similar approach was utilized by Dong et al. (2018) to predict crack growth and quantify the time-variant fatigue reliability of welded joints subjected to stochastic loading. The uncertainty in the residual stress distribution, crack propagation regression parameters, and initial crack size are considered in their study.

The fatigue reliability quantification studies discussed above primarily considered the uncertainty associated with the loads, mechanical properties, residual stresses, and the initial crack size. However, less focus has been placed on integrating the uncertainties associated with the geometric parameters associated with the probabilistic crack propagation prediction process and fatigue reliability quantification. For a stiffened hull girder, differences between the as-built and designed dimensions are inevitable due to manufacturing tolerances and the welding intensive nature of the fabrication process of this type of structures (Caiazzo et al., 2017). These differences lead to uncertainties in the

geometric properties such as spacing between stiffeners, plate thicknesses, and stiffener dimensions (Hess et al., 2002) and are expected to have a significant influence on the crack propagation process (Sankararaman, et al., 2011). Accordingly, to properly characterize the crack propagation behavior in stiffened panels and quantify the reliability under growing cracks, it is essential to first understand the role of the geometric properties of the stiffened panel on the crack propagation within the hull and to identify those parameters that have a significant influence on the crack growth behavior. Furthermore, the effect of the geometric uncertainties on the reliability profiles should be well understood.

This chapter addresses these needs and quantifies the influence of various sources of uncertainty, including those associated with mechanical properties and geometric parameters, on the crack propagation behavior and fatigue service life of welded stiffened panels. The geometric parameters include the main panel thickness and stiffener characteristics (i.e., shape, spacing, and dimensions) while the mechanical properties include the modulus of elasticity, and yield strength, in addition to the crack propagation model regression parameters. 3-D FE analysis, artificial neural networks, and an elastic-plastic crack advancement rule are integrated to predict the crack propagation profiles for the investigated welded stiffened panels. Variance-based sensitivity analysis is conducted for quantifying the influences of the considered input parameters on the variability of the fatigue service life. Finally, MCS is utilized to quantify the fatigue reliability of the welded stiffened panels and evaluate the impact of including uncertainties associated with geometric parameters on the resulting reliability profiles.

4.3. Sensitivity Analysis

Sensitivity analysis can be implemented to quantify the effect of random input variables on the response of a model. Such analysis can be helpful in dimensionality reduction of

problems involving probabilistic modeling and reliability assessment (Gaspar et al., 2016). This analysis can quantify the effect of the variability in the model input variables on the variability of the model output (Saltelli et al., 2008) and identify the variables that have a significant contribution to the variability of the response. These influential parameters can then be considered as random variables in the probabilistic model while the remaining parameters can be considered deterministic (Opgenoord et al., 2016; Khandel et al. 2021). The sensitivity analysis also offers valuable information regarding the influence of various input variables on the model response and can quantify the increase or decrease in the response quantity of interest given the change in the input variable (Gaspar et al., 2016). Such analysis can also be beneficial in structural design optimization and cost-benefit analysis since it identifies the governing variables that have a significant contribution to model response (Leheta & Mansour, 1997).

Sensitivity analysis can be conducted using local or global approaches (Saltelli et al., 2008; Sudret, 2008). The local methods (e.g., the first-order second-moments (FOSM)) are typically utilized to evaluate the sensitivity of the model response to changes in the input random variables around a certain nominal point (e.g., mean values of the variables). Local methods are based on the derivative of the model output with respect to the parameter whose sensitivity is required (Qian & Mahdi, 2020; Castillo et al., 2007; Gaspar et al., 2016). These methods have the limitation of providing sensitivity measures related only to a prescribed point and are often based on linearizing the model response around this point. On the contrary, global methods provide a comprehensive or overall sensitivity measure by considering the whole space of the model input random variables. These methods are not limited to a specific point and can take into account the interaction effects between

input random variables. For complex problems involving a large number of uncertain parameters such as fatigue crack propagation in welded stiffened panels, the sensitivity measures calculated at a certain point (i.e., using local methods) may not be valid over the whole input space. Furthermore, the effect of an input parameter on the output quantity of interest may vary significantly when the other parameters change (Velarde, et al., 2019). Therefore, assessing the sensitivity of the response to one parameter while other parameters remain constant may not be adequate to develop a proper understanding of the behavior; accordingly, global sensitivity analysis is adopted in this chapter.

Variance-based global sensitivity analysis provides a quantitative measure that represents the contribution of various input parameters to the output variance. This contribution is quantified by dividing the output variance into fractions and evaluating the fraction associated with each input parameter (Saltelli et al., 2010). Variance-based sensitivity enables comprehensive input space exploration while taking nonlinear responses and interactions among input parameters into consideration. Two common methods are available for performing the variance-based sensitivity, namely the Fourier amplitude sensitivity test (FAST) and Sobol's method. FAST can handle nonlinear relationships between input and output; however, it does not account for the interaction among input parameters (Saltelli et al., 2010). Sobol's approach (Sobol, 2001), adopted in this chapter, quantifies the variance-based sensitivity measures for complex systems where the nonlinearity and/or interactions effect can be significant.

4.3.1. Sobol Decomposition and Sobol's Sensitivity Indices

Consider the random vector **X** comprising the system input parameters and the response function $F(\mathbf{X})$ in the *n*-dimensional unit cube k^n. The response function can be expressed as (Sobol, 2001):

$$F(\mathbf{X}) = F_0 + \sum_{1\le i\le n} F_i(X_i) + \sum_{1\le i\le j\le n} F_{ij}(X_i, X_j) + \cdots + F_{1\,2\ldots n}(X_1, \ldots, X_n) \quad (4\text{-}1)$$

where **X** is the input vector with *n* random parameters, F_o is the mean value of the response function, F_i is a function representing the portion of $F(\mathbf{X})$ affected by parameter X_i, and F_{ij} is the portion of $F(\mathbf{X})$ resulting from the interaction between X_i and X_j. The terms on the righthand side of the equation (i.e., Sobol's functions) can be calculated by integrating the response function as:

$$F_o = \int_{K^n} F(x)dx \quad (4\text{-}2)$$

$$F_i(X_i) = \int_{K^{n-1}} F(x_{\sim i}, X_i)dx_{\sim i} - F_o \quad (4\text{-}3)$$

$$F_{ij}(X_i, X_j) = \int_{K^{n-2}} F(x_{\sim ij}, X_i, X_j)dx_{\sim ij} - F_i(X_i) - F_j(X_j) - F_o \quad (4\text{-}4)$$

where $x_{\sim i}$ is a dummy variable indicating that the variable x_i is excluded from the calculations; hence, the term $\int_{K^{n-1}} F(x_{\sim i}, X_i)dx_{\sim i}dx_{\sim i}$ symbolizes an integration with respect to all variables except X_i. Sobol's functions are orthogonal, accordingly:

$$\int_{K^n} F_{i1,i2,\ldots is}(X_i, X_j, \ldots X_{is})F_{j1,j2,\ldots js}(X_{j1}, X_{j2}, \ldots X_{js})dx = 0 \quad (4\text{-}5)$$

Consequently, the total variance D of $F(\boldsymbol{X})$ can be calculated as:

$$D = Var[F(\boldsymbol{X})] = \int_{k^n} F^2(X)dX - F_0^2 \quad (4\text{-}6)$$

where the input parameters are defined on the *n*-dimensional unit cube k^n. By integrating the square of Equation (4-1), it is possible to decompose the variance as:

$$D = \sum_{1\le i\le n} D_i + \sum_{1\le i\le j\le n} D_{ij} + \cdots + D_{1\,2\ldots n} \quad (4\text{-}7)$$

$$D_i = \int_{k^1} {F_i}^2(X_i)dX_i \quad (4\text{-}8)$$

$$D_{ij} = \int_{k^2} {F_{ij}}^2(X_i, X_j) dX_i dX_j \quad (4\text{-}9)$$

where D_i is the partial variance of parameter X_i, D_{ij} represents the partial variance due to the interaction between parameters X_i and X_j, and $D_{1\ 2\ldots n}$ is the partial variance due to the interaction between parameters X_1 to X_n. Sobol's sensitivity indices can then be computed as

$$S_i = \frac{D_i}{D} \quad (4\text{-}10)$$

$$S_{ij} = \frac{D_{ij}}{D} \quad (4\text{-}11)$$

where, S_i is the first-order sensitivity index which corresponds to the change in the variance of the output due to change in *i*th parameter alone, while the higher-order sensitivity indices S_{ij} express the change in the variance of the output due to the interactions among multiple variables. Next, the total Sobol's sensitivity index (S_i^T) of one parameter X_i can be expressed as the summation of the first and higher-order sensitivity indices.

Sobol's indices can be computed by utilizing MCS. This approach involves sampling a large number of realizations from one input variable, while the other variables remain constant, and calculating the uncertainty in the output variance. However, this approach may have limited applications given the high computational cost associated with the large number of samples required to perform the analysis (Saltelli, 2008). Meta-modeling techniques can be used to address the limitation associated with the computational cost of the Monte Carlo simulation. A meta-model is a computationally inexpensive model that can produce statistically equivalent findings for a complex model without a known closed-form solution through a limited number of original model executions (Konakli & Sudret,

2016). Several meta-modeling tools are available to fulfil this task, such as low-rank tensor approximation (LRA) or polynomial chaos expansion (PCE) (Janon, 2014). The LRA approximation was shown in Konakli & Sudret (2016) to converge faster to the exact solution and outperform the PCE in predicting extreme model responses. Accordingly, variance-based sensitivity in conjunction with LRA will be utilized herein to evaluate the effect of the variability in several geometrical and mechanical characteristics on the variability in the fatigue service life of stiffened panels.

4.4. Fatigue Crack Propagation Approach

Several approaches have been proposed to predict fatigue crack propagation in stiffened panels. The model proposed by Paris & Erdogan (1963) can characterize fatigue crack propagation based on the Linear Elastic Fracture Mechanics (LEFM) assumptions. In this model, crack propagation rate under constant amplitude loading can be calculated as (Paris & Erdogan, 1963):

$$\frac{da}{dN} = c_0(\Delta K)^{m_0} \tag{4-12}$$

where a is the crack size, N is the number of cycles, c_0 and m_0 are material regression parameters denoted, respectively, as the power law coefficient and Paris exponent, and ΔK is the range of the stress intensity factor (SIF). This model can be used to predict fatigue crack propagation under LEFM assumptions which consider the size of the plastic zone around the crack tip to be small compared to the size of the component (i.e., small-scale yielding (SSY) condition). However, when LEFM conditions are not met, such as in the case of long cracks in ship hulls or if large-scale yielding (LSY) occurs, elastic-plastic fracture mechanics (EPFM) parameters, such as the *J*-integral or the crack tip opening displacement (CTOD) can be utilized to compute the crack driving force (Anderson, 2017;

Božić et al., 2011). In this chapter, the CTOD is used to compute the crack driving force instead of the SIF since the cracks in stiffened panels can propagate considerably before failure occurrence (Anderson, 2017). The crack growth rate can then be computed as (McEvily, 1973):

$$\frac{da}{dN} = C_{CTOD}(\Delta CTOD)^{m_{CTOD}} \tag{4-13}$$

$$m_{CTOD} = \frac{m_0}{2} \tag{4-14}$$

$$C_{CTOD} = \left(\frac{\sigma_y}{d}\right)^{\frac{m_0}{2}} E^{\frac{m_0}{2}}.c_0 \tag{4-15}$$

where E is the modulus of elasticity, σ_y is the material yield strength, and d is the plastic constraint factor (d =1 for plane stress and 2 for plane strain condition).

Another factor that has a significant influence on the crack propagation behavior in welded stiffened panels is the presence of residual stresses. These stresses develop in the panel during fabrication and welding. The presence of residual stresses may result in early yielding in some regions of a stiffened plate which can lead to accelerating the crack growth rate (Deng et al., 2007). Kondo & Ostapenko (1964) found that the welding process produces high residual tensile stresses in regions adjacent to the stiffener and compressive residual stresses in the region between stiffeners. The crack growth rate may decrease in the regions of compressive residual stresses and increase under tensile residual stresses (Nussbaumer et al., 1999). Therefore, the effects of residual stresses should be taken into account while calculating the crack driving force.

In this chapter, the idealized welding-induced residual stress model proposed in Faulkner (1975) is adopted to define the magnitude and distribution of the residual stresses in the stiffened panels. This model defines a triangular tensile stress distribution in the regions immediately surrounding the weld with a magnitude equal to the yield stress, this

region has a width of $\eta \times t_p$, where t_p is the main panel thickness and η is a constant representing the width of the tensile stress region. In ship structures, this constant is often assumed to range between 3 and 4 depending on the stiffened panel design and welding conditions (Faulkner, 1975). The remaining regions in the main panel between stiffeners are subjected to uniform compressive residual stresses whose magnitude is calculated by satisfying force equilibrium between tensile and compressive regions (Faulkner, 1975).

Residual stresses may also form in the stiffeners due to welding. In this chapter, a triangular tensile stress distribution is defined in the web of the stiffener in the regions immediately surrounding the welds with a magnitude equal to the yield stress of the steel (Gannon, 2011). This tensile stress region has a width of $\eta \times t_{sw}$, where t_{sw} is the stiffener web thickness. As indicated in Gannon (2011), the remaining region of the stiffener web is subjected to a steep transition from tensile to compressive residual stress. The magnitude of the compressive residual stresses is calculated by satisfying equilibrium conditions between the tensile and compressive forces. Gannon (2011) also evaluated, experimentally, the magnitude of the residual stresses in the flanges of the T- and L-stiffeners, which were found to exhibit considerable variability. This stress magnitude was found to range between -10 MPa to 7 MPa and -11 MPa to 12 MPa for the T- and L-stiffeners, respectively (Gannon, 2011). This magnitude of residual stress is very small compared to the material resistance. Accordingly, the residual stresses in the flanges were neglected in the subsequent sensitivity and reliability analysis shown in this chapter. Figure 4-1 shows the residual stress distribution in the main panel and stiffeners.

In this chapter, a numerical model is employed to calculate the crack driving parameter for the stiffened panels under propagating crack. The calculated crack driving

parameter is a result of the externally applied loads and the residual stresses. The developed numerical model, in conjunction with the analytical crack propagation given by Equation (4-13), is used to calculate crack growth increment under the applied cyclic load on a cycle-by-cycle basis. However, given the large number of cycles required for this simulation, machine learning is employed to surrogate the numerical analysis and provide the crack driving parameter given a particular set of input parameters. A more detailed discussion of the adopted machine learning algorithm is presented in the following section.

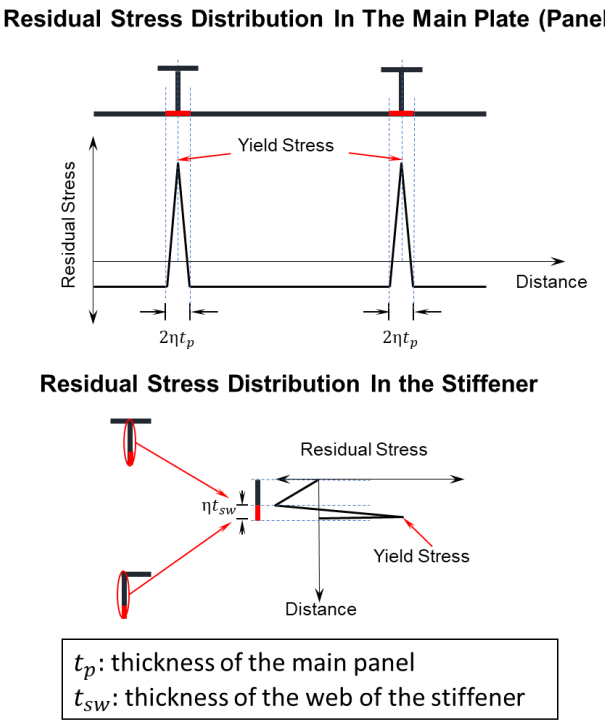

Figure 4-1. Idealized residual stress distribution and magnitude due to welding in the main panel and stiffeners

4.5. ANN-Assisted Crack Growth Prediction

ANNs are commonly used to provide a simplified approximation of complex and higher-order models due to their capability to simulate the behavior of a wide range of complex and physical relationships. Once the ANN is trained and validated, it will gain the ability to predict the output for a given input that falls within the training domain (Avcar &

Saplıoğlu, 2015). Several types of neural networks can be used to surrogate complex computational problems including feedforward, radial basis function, convolutional, recurrent, and modular neural networks, Feedforward ANN is implemented herein due to its superior performance and computational efficiency compared to the other ANN types in the matter of highly nonlinear problems such as the crack propagation in welded stiffened panels (Mortazavi & Ince, 2020; Ma et al., 2021).

Feedforward ANNs are composed of input, output, and hidden layers. An input layer, also known as a passive layer, is responsible for receiving the dataset from an external source and passing it to the subsequent layer for further processing. One or more hidden layers are placed to process the dataset through the interconnections between nodes. After processing, the network sends an output to an external receptor from the nodes on the output layer. ANN is composed of a large number of interconnected processing elements known as artificial neurons organized in layers. These neurons are responsible for converting the input units to nonlinear functions of linear combinations of weights and bias factors, then sending the output to the next layer. The assigned weights and bias factors are optimized by minimizing the error between the target outputs and the ANN prediction. Each input parameter is represented by a single neuron in the input layer, next, the values of these inputs are transferred to the subsequent neurons in the hidden layers. The output ${y_o}^m$ of a neuron o in layer m is calculated as (Hambli, 2010)

$$ {y_o}^m = f({v_o}^m) \tag{4-16} $$

$$ {v_o}^m = \sum_{r=1}^{L} {w_{ro}}^{m-1} {y_o}^{m-1} + {b_o}^m \tag{4-17} $$

where f denotes the activation function, which is generally considered a sigmoid function (e.g., hyperbolic tangent and logistic functions) (Dresia et al., 2019), L is the number of

connections to the previous layer, ${w_{ro}}^{m-1}$ are the weights of each connection, and ${b_o}^m$ is the bias factor. The Levenberg-Marquardt algorithm (LMA) is used herein for training the ANN due to its accuracy and convergence characteristics (Hagan & Menhaj, 1994). This algorithm minimizes the total mean square error between the actual output of the multi-layer network and the desired output (Khan et al., 2013). Feedforward artificial neural networks that adopt Levenberg–Marquardt algorithm are utilized in this chapter to surrogate the numerical analysis and provide the crack driving parameter given a certain set of input parameters.

4.6. Performance Function and Fatigue Reliability Analysis

Once the effect of the variability in the underlying geometric and mechanical parameters is evaluated, probabilistic analysis is conducted to evaluate the effect of uncertainties associated with the important parameters (i.e., those identified based on the sensitivity analysis) on the fatigue reliability of the stiffened panels. To quantify the reliability index, the following performance function G is defined:

$$G(N) = CTOD(\mathbf{M}, N) - CTOD_c(\mathbf{M}) \tag{4-18}$$

where $CTOD_c$ represents the fracture resistance of the material given the vector of random parameters $\mathbf{M}$, while $CTOD(\mathbf{M}, t)$ is the applied CTOD given the vector of random variables **M** and number of applied load cycles *N*. Accordingly, a failure condition is reached if the calculated CTOD at after a given number of cycles is larger than the critical CTOD. The performance function is then integrated into a Monte Carlo simulation process to calculate the probability of exceeding the critical CTOD $P_e(N)$ as

$$P_e(N) = P[G(N) > 0] \tag{4-19}$$

The reliability index is then calculated as a function of the probability of failure:

$$\beta(t) = \Phi^{-1}[1 - P_e] \tag{4-20}$$

where Φ^{-1} denotes the inverse standard normal distribution function, and β is the reliability index based on the crack driving parameter.

4.7. Case Study

This chapter focuses on assessing the performance of welded stiffened panels under propagating fatigue cracks using machine-learning-assisted simulation. ANN is used to generate a surrogate model of the system response and is next integrated with LRA to identify the key contributing variables that significantly affect the fatigue service life of stiffened panels. The key contributing variables that have a considerable influence on the fatigue service life are only treated as random variables within the following reliability analysis. This process helps reduce the number of random variables associated with the problem resulting in a more efficient and accurate probabilistic simulation process. Finally, the developed approach is integrated into the MCS process to quantify the fatigue reliability of welded stiffened panels, a schematic representation of the developed approach can be expressed in Figure 4-2.

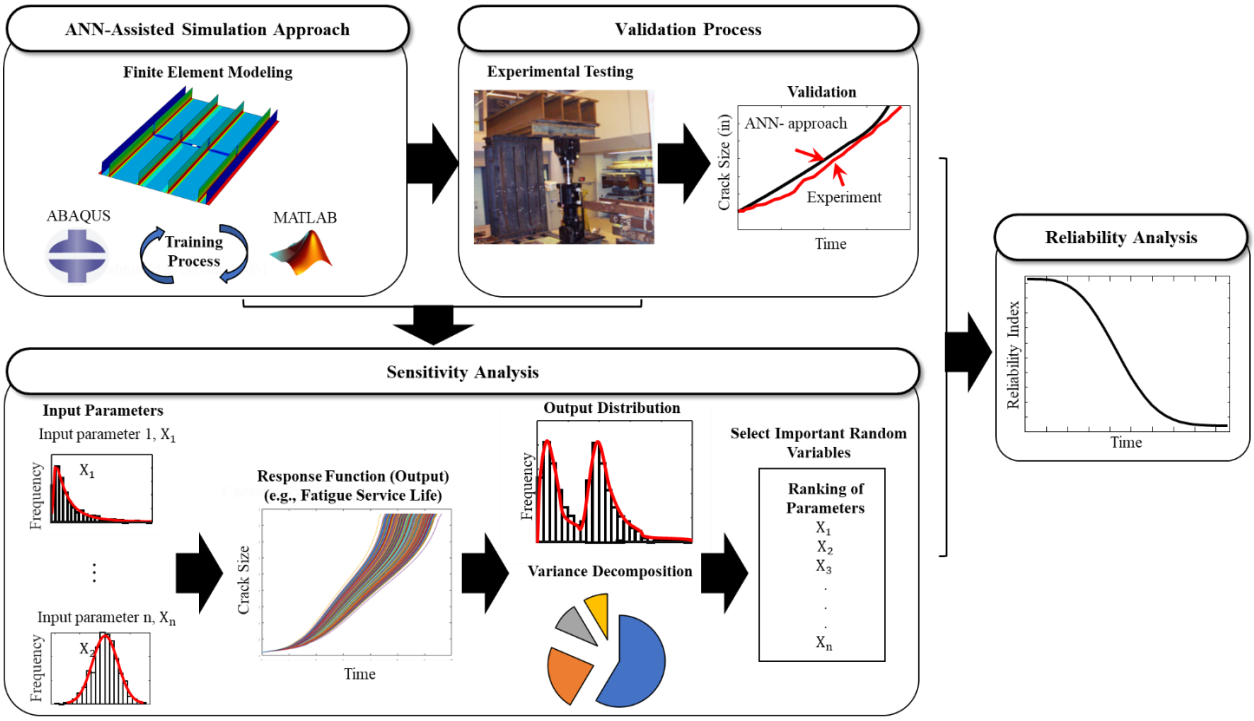

Figure 4-2. A schematic representation of the developed ANN-assisted simulation approach

The sensitivity and reliability assessment approach discussed above is illustrated on stiffened panels with T- and L-shape stiffeners subjected to axial tensile fatigue loading. The stiffened panels analyzed herein were investigated experimentally in Mahmoud & Dexter (2005). The presence of experimental testing results allows for validating the adopted crack growth prediction approach. The stiffened panels were constructed with a length of 3,454 mm, width of 1,626 mm, and a main panel thickness of either 13 mm or 9 mm. Four specimens were tested in Mahmoud and Dexter (2005). The specimens were fabricated with four L (L101×76×8) or bulb T stiffeners (HP160×9). The stiffeners were spaced at 381 mm or 305 mm. A general layout of the stiffened panels is shown in Figure 4-3, while Table 4-1 presents the test matrix for the experimentally tested specimens in Mahmoud & Dexter (2005). A center, through-thickness, fatigue crack at the mid-section with a size of 152.5 mm was initiated in the panels and its propagation across the panel

was tracked during the tests. A constant amplitude cyclic load was applied to all the specimens resulting in a stress range of 55 MPa with a load ratio of 0.2. The main panels were constructed using A572 Gr. 50 steel (ASTM A572/A572M, 2015), while the stiffeners were constructed using grade AH36 steel (ASTM A131, 2019).

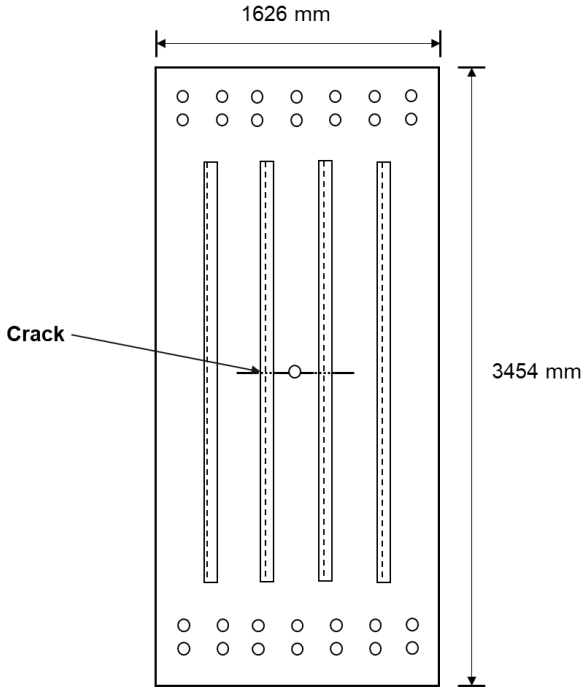

Figure 4-3. A view of the general geometry for the stiffened panels (adapted from Mahmoud and Dexter 2005).

Table 4-1. Test matrix for the specimens tested experimentally in Mahmoud & Dexter (2005)

Specimen Number	Main Panel Thickness	Stiffener Type	Stiffener Spacing
S1	13 mm	Bulb-T (HP160 x 9)	381 mm
S2	13 mm	Bulb-T (HP160 x 9)	305 mm
S3	13 mm	L-Shape (L101×76×8)	381 mm
S4	9 mm	Bulb-T (HP160 x 9)	381 mm

In order to compute the crack driving parameter, 3-D FE models of the stiffened panels are constructed in ABAQUS environment (Simulia, 2018) in which the main panel and stiffeners are modeled using four-node shell elements (S4R element). An element size

of 10 mm is chosen and the loading is applied at one end of the stiffened panel while the support conditions are applied at the opposite end as shown in Figure 4-4. Translations and rotations about x, y, and z directions are restricted at the support end. The contour integral method in ABAQUS is used to quantify the crack driving parameter. In this approach, the crack tip behavior is studied by constructing rings of elements in the radial direction around the crack tip. Thirty elements around the crack tip are used in the developed models based on Brocks & Scheider (2001). A close-up view of the mesh surrounding the crack tip is also shown in Figure 4-4. The selection of the crack driving parameter is based on the yielding conditions ahead of the crack tip. A SSY condition is expected to occur for small crack sizes; however, as the crack length increases, LSY condion may occur. Accordingly, the yielding condition of these stiffened panels is evaluated next section in order to select an appropriate crack driving parameter.

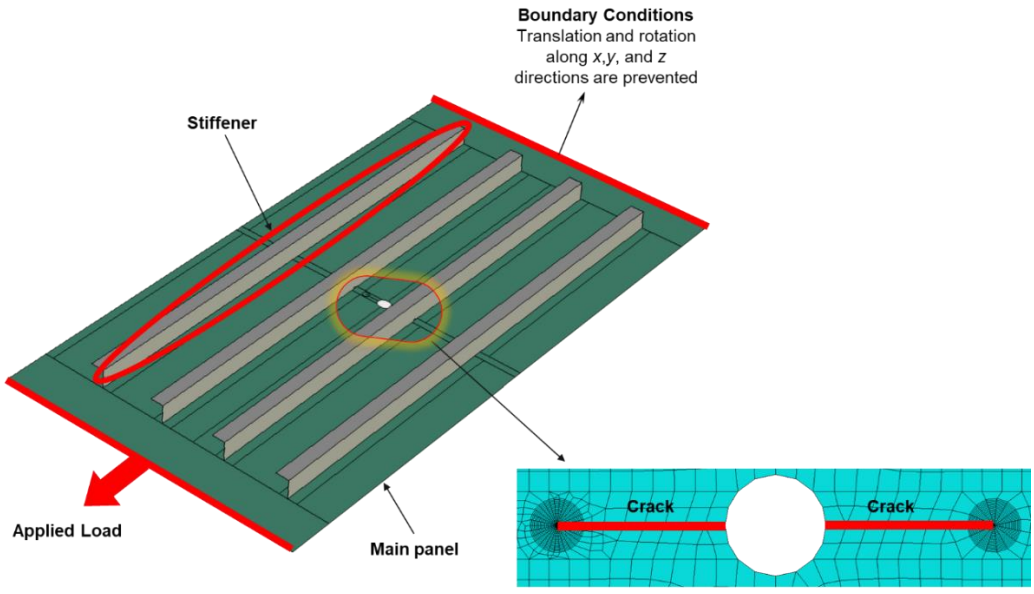

Figure 4-4. Visualization of the developed finite element model, loading, boundary conditions, and mesh configuration.

4.7.1. Evaluation of the Crack Tip Condition

The yielding condition within stiffened panels is evaluated based on the approach proposed in Marques et al. (2021) which quantifies the elastic (δ_e) and plastic (δ_p) components of the CTOD to distinguish between SSY and LSY conditions. In Marques et al. (2021), it was found that SSY conditions become dominant ahead of the crack tip when the proportion of the elastic component of the CTOD to the total CTOD (δ_t) exceeds 75%. However, when this ratio drops below 60%, the LSY conditions becomes dominant. For this case study, the CTOD is measured from the FE model up to the maximum possible applied stress (i.e., 70 MPa), then the elastic and plastic components of CTOD are calculated. This is shown in Figure 4-5(a) for Specimen 1 listed in Table 4-1. At this crack size, the ratio of the elastic CTOD to the total CTOD is 54%. This indicates that LSY conditions may occur under the selected crack size and stress level.

The analysis in Figure 4-5(a) is repeated for crack sizes ranging from 50 to 650 mm, then the ratio between the elastic CTOD and the total CTOD is calculated. As shown in Figure 4-5(b), this ratio is above 75% when the crack size is less than 120 mm, which indicates that SSY conditions are applicable. This ratio decreases as the crack grows and drops below 60% when the crack size is between 120 and 650 mm. A similar behavior was found for the other specimens where LSY condition is reached at crack sizes of 165 mm, 140 mm, and 180 mm, respectively for specimens S2, S3, and S4. Accordingly, the EPFM parameter CTOD is considered to quantify the crack driving force based on Equations (4-13) to (4-15).

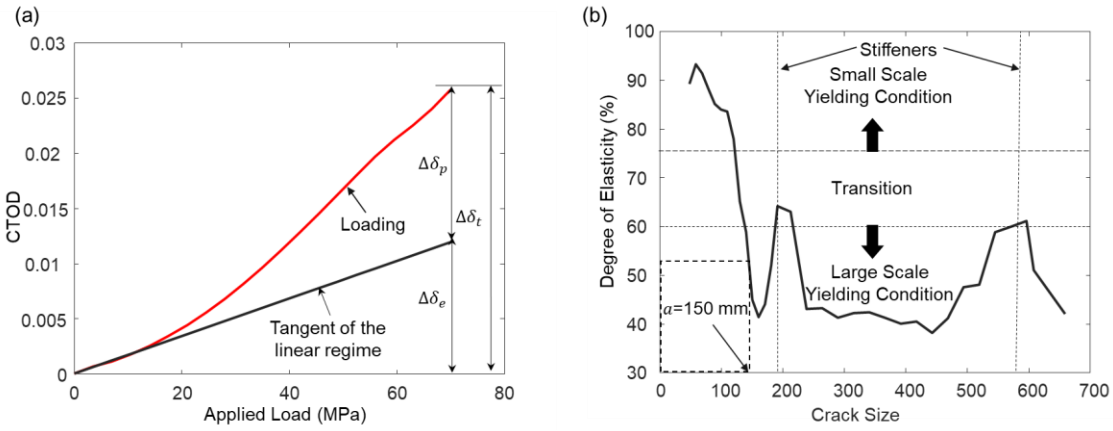

Figure 4-5. The yielding condition of the investigated stiffened panel: (a) CTOD versus the applied load at a crack size equal to 150 mm (b) degree of plasticity measured using the FE model under the maximum applied stress and half crack size ranging from 50-650 mm.

4.7.2. Application of ANNs to Quantify the Crack Driving Parameter

The ultimate goal of this chapter is to quantify the influence of relevant sources of uncertainty, including those associated with the mechanical properties and geometric parameters, on the fatigue reliability and service life of welded stiffened panels. In order to calculate the fatigue service life of stiffened panels, the FE model needs to be constructed and executed to compute the crack driving parameter for each load cycle as the crack propagates. However, each stiffened panel in this example may be subjected to millions of cycles. As a result, it was not possible to utilize the FE analysis directly for each load cycle. Given the computational cost involved with the iterative execution of the FE models, feedforward ANNs that adopt Levenberg–Marquardt algorithm have been utilized to surrogate the FE model and compute the crack driving parameter given a certain set of input parameters.

Since it was desirable to quantify the influence of various sources of uncertainty considering several configurations of stiffened panels (e.g., different stiffener characteristics and main panel thickness), wide variations in the input parameters are

considered in the ANN training dataset. For instance, stiffened panels with main panels thickness ranging from 6 mm to 30 mm are considered. Stiffener heights between 50 mm and 450 mm are also included. The training dataset also covers a wide range of spacing between stiffeners. Table 4-2 shows the input parameters and the range covered in the training process. The Sobol sequence experimental sampling design technique (Sobol & Levitan, 1999) is employed to identify the combinations of input parameter values that are utilized to construct the training dataset. A total of 45,000 samples are generated for training and testing the ANN. Among those, 75% is used to train the ANN, 15% is used for validation, and 10% is used for testing (Jaimes et al., 2005).

Table 4-2. Range of input parameters covered in the ANN training dataset.

Variable	Range
Stiffener Spacing	$[150 - 450]\ mm$
Stiffener Web Thickness	$[5 - 30]\ mm$
Stiffener Flange Thickness	$[5 - 30]\ mm$
Stiffener Flange Width	$[0 - 450]\ mm$
Stiffener Web Height	$[50 - 450] mm$
Main Panel Thickness	$[5 - 30]\ mm$
Crack Size (Main Panel)	$[37.5 - 830]\ mm$
Modulus of Elasticity	$[150 - 250]\ GPa$
Yield Stress	$[300 - 450]\ MPa$
Stress Level	$[0 - 100]\ MPa$

A MATLAB script is used to create the input file needed to build and execute the FE model and collect the output (i.e., actual CTOD) associated with the set of input parameters (Table 4-2 shows the considered of input paramters). Based on convergence analysis, it was found that a feedforward ANN with 8 hidden layers and 7 neurons for each layer can predict the relation between the FE obtained CTOD and the associated set of input parameters. The neural network toolbox in MATLAB (MathWorks, 2020) is used to

conduct this analysis. To verify that the trained ANN model is not overfitting and to avoid the potential deviation while analyzing a dataset not included in the training data, a new testing dataset including 500 samples is selected randomly from the ranges of input parameters and tested against the FE results. Figure 4-6 shows a comparison between the FE results and the ANN prediction. As shown, the ANN can be utilized to provide an accurate prediction of the crack driving parameter of these stiffened panels; accordingly, it will be used in the next sections to validate the crack prediction approach and also to perform the sensitivity and reliability analysis presented in subsequent sections.

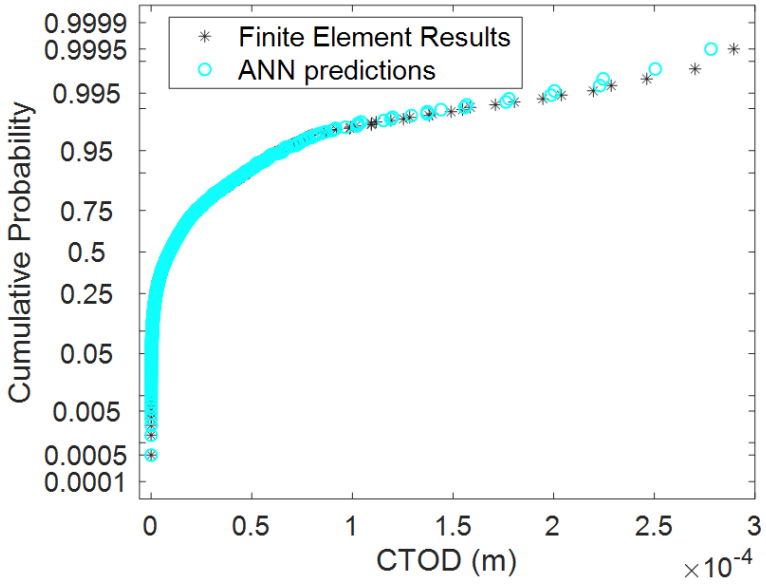

Figure 4-6. Comparison between the FE results to the ANN prediction

4.7.3. Validation of the Crack Propagation Prediction Approach

The ability of the ANN-assisted simulation approach to predict the crack propagation in stiffened panels is validated using the experimental results reported in Mahmoud & Dexter (2005). The developed model, in conjunction with the analytical crack propagation rule given by Equations (4-13) – (4-15), is used to calculate crack size increment under the

applied load. The regression parameters values of the Paris Law (c_0 and m_0) are obtained according to Barasom & Rolfe, (1987) and DNV (1984), where the value of c_0 for this material is taken as 9.5×10^{-12}, and the value of m_0 is 3 for units of MPa for stresses and meters for crack size. Figure 4-7 shows the crack propagation profiles obtained utilizing the ANN-assisted simulation approach and compares them to those obtained experimentally and reported in Mahmoud & Dexter (2005). The figure shows that the developed approach can capture the crack growth behavior and provide accurate crack growth predition. Note that the actual mechanical properties of the material used in fabricating the specimens were not provided in Mahmoud & Dexter (2005) which may have led to the difference between the prediction and experimental results in Figure 4-7.

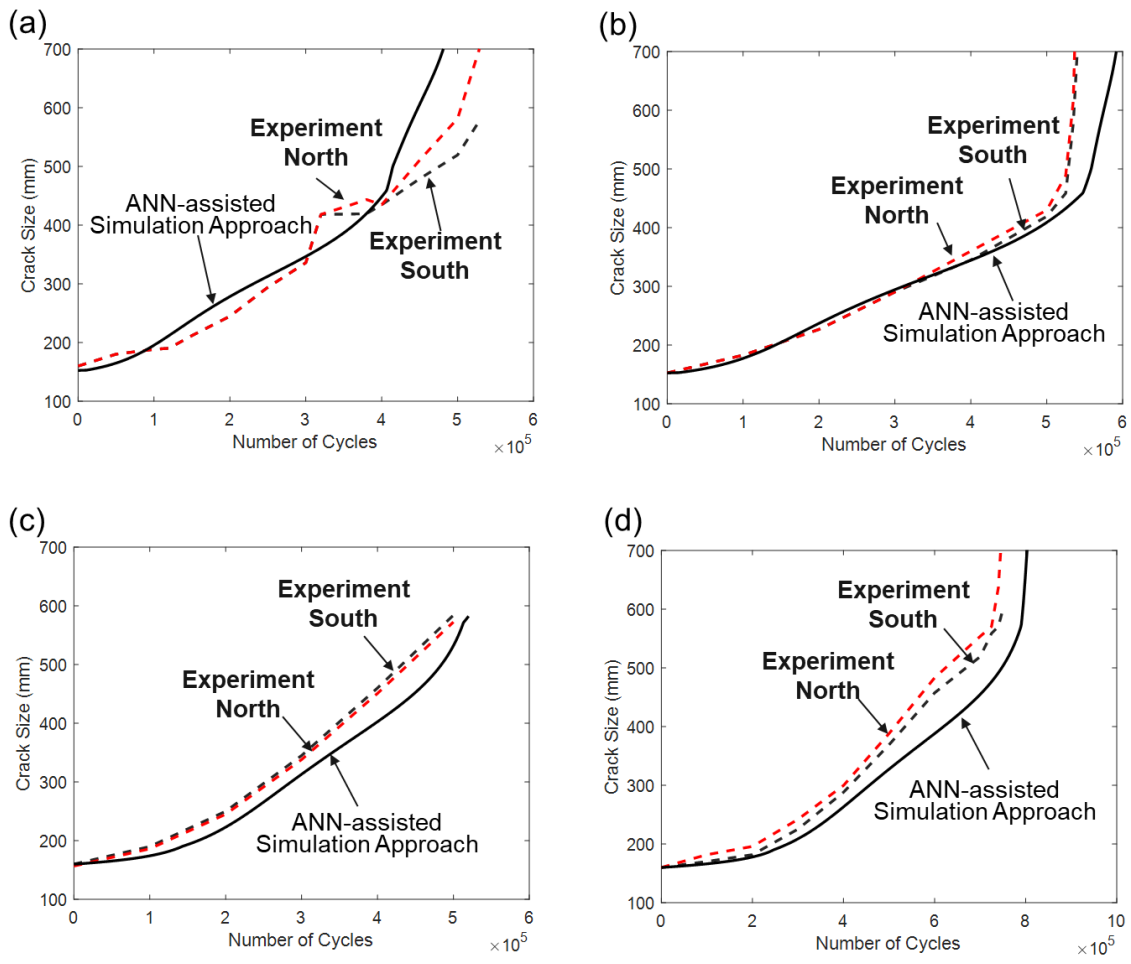

Figure 4-7. Comparison between the crack propagation profile obtained using the ANN-assisted simulation approach and the experimental tests conducted by Mahmoud and Dexter (2005): (a) specimen 1, (b) specimen 2, (c) specimen 3, and (d) specimen 4.

4.7.4. Sensitivity Analysis of the Fatigue Service Life

Sensitivity analysis is conducted utilizing the ANN-assisted simulation approach with the objective of identifying the key parameters that have a significant effect on the fatigue service life of stiffened panels. The sensitivity analysis is conducted on stiffened panels with two different stiffener types (i.e., T- and L-stiffeners) with the characteristics and dimensions presented in Table 4-3. These stiffener types are selected since they are the most commonly used types in ship hull construction (Tharain et al., 2013). The sensitivity

analysis considers geometric parameters (i.e., main panel thickness, stiffener characteristics, and spacing between stiffeners), as well as mechanical properties (i.e., Paris' law material regression parameters, modulus of elasticity, and yield strength) as the input parameters. The probabilistic descriptors of these parameters are summarized in Table 4-3. The developed crack propagation model is used to calculate crack size increment under the applied cyclic load with a stress range of 55 MPa and a load ratio of 0.2. The number of cycles needed for the crack to propagate in the main panels from 152.5 mm to the total width of the panel is designated as the response parameter of interest.

Table 4-3. The statistical descriptors of the considered parameter.

Variable	Unit	Stiffeners Type		COV	Distribution	Reference
		T-Shaped	L-Shaped			
Stiffeners Height	mm	101	101	0.019	Normal	(Hess et al., 2002)
Flange Width	mm	76	76	0.019	Normal	(Hess et al., 2002)
Stiffener Thickness (Web)	mm	8	8	0.05	Normal	(Hess et al., 2002)
Stiffener Thickness (Flange)	mm	8	8	0.05	Normal	(Hess et al., 2002)
Stiffener Spacing	mm	381		0.03	Normal	(Hess et al., 2002)
Modules of Elasticity	GPa	200		0.0179	Lognormal	(Hess et al., 2002)
Yield Stress	MPa	400		0.068	Lognormal	(Hess et al., 2002)
Main Panel Thickness	mm	13		0.05	Normal	(Hess et al., 2002)
c_0*	$\left(\frac{m}{cycle.(\mathrm{MPa}\sqrt{\mathrm{m}})^{m_o}}\right)$	9.5×10^{-12}		0.055	Normal	(Barasom and Rolfe, 1987, DNV, 1984)
m_0*	-	3		0.1	Normal	(Barasom and Rolfe, 1987, DNV, 1984)
$CTOD_{cr}$	mm	0.2		0.15	Normal	(Feng et al, 2012; Kayamori & Kawabata, 2017)
ANN Bias Factor (FE/ANN)	-	0.988		0.01	Normal	Derived

* Correlation coefficient between c_0 and m_0 is -0.95 (Chung, 2004)

Variance-based sensitivity in conjunction with LRA is then utilized to evaluate the effect of the variability of the considered parameters on the variability in the fatigue service life of stiffened panels given their marginal distributions. UQ-Lab MATLAB toolbox (Marelli & Sudret, 2014) is used to calculate Sobol's sensitivity indices associated with the considered parameters. Based on the results of a convergence analysis, 2,000 samples are drawn from each of the considered parameters to obtain accurate Sobol's indices. The results of the conducted sensitivity analysis are shown in Figures 4-8 to 4-10. Figure 4-8 shows the total Sobol's sensitivity indices collectively for the considered variables associated with the geometric parameters (i.e., main panel thickness, stiffener characteristics, and spacing between stiffeners) and mechanical properties (i.e., Paris' law material regression parameters, modulus of elasticity, and yield strength). As shown, the collective Sobol's indices associated with both groups of parameters are very close which indicates that the contribution of the geometric parameters to the variability of the response is approximately equal to that of the mechanical properties. Accordingly, neglecting the uncertainties associated with the geometric parameters may lead to errors in fatigue reliability analysis. This will be investigated further in the last section of this chapter.

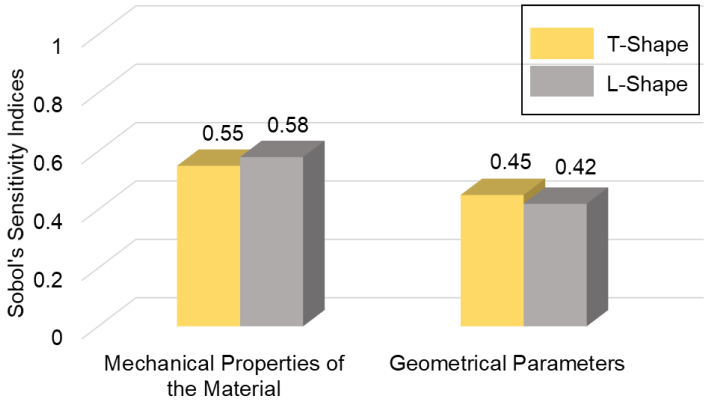

Figure 4-8. The total sensitivity indices of the geometrical and mechanical parameters for the investigated stiffened panel.

To quantify the effect of the variability in each input parameter on the variability of the fatigue service life, the total Sobol's sensitivity indices of the input parameters associated with the mechanical properties are quantified for the investigated stiffened panels. The results are depicted in Figure 4-9. As shown, the variability in the fatigue service life is strongly influenced by the variability in Paris' law material regression parameters (i.e., c_o and m_o) while the modulus of elasticity and yield strength seem to have a lower effect. The total Sobol's sensitivity indices of the considered geometric parameters are computed next and shown in Figure 4-10. The results show that the variability in fatigue service life highly depends on the variability in the main panel thickness for both stiffener types. The contribution of the main panel thickness to the total variance of the fatigue service life is approximately 44% for the two types of stiffened panels. The second dominant quantity is the stiffener web properties (i.e., height and thickness), followed by the spacing between stiffeners. The flange properties (i.e., flange width and thickness) have a low contribution with indices less than 5%.

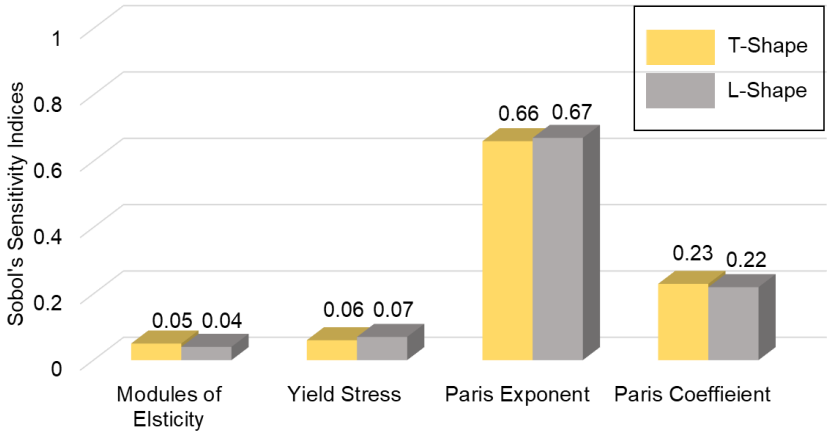

Figure 4-9. The total sensitivity indices of the individual input parameters associated with the mechanical properties of the material for the investigated stiffened panel.

Figure 4-10. The total sensitivity indices of the individual input parameters associated with the geometrical parameters for the investigated stiffened panels.

4.7.5. Effect of Altering the Geometric Parameters on the Fatigue Service Life

The conducted sensitivity analysis is very helpful to understand the importance and interaction among various parameters related to the fatigue crack growth in welded stiffened panels. The results show how the uncertainty in the fatigue service life is affected by different sources of uncertainties in its input; however, it does not directly quantify the actual change in the output with the change in an input parameter. Accordingly, the ANN-assisted simulation approach is next utilized to investigate the effect of changing the geometric parameters on the crack growth behavior. The crack propagation profile for the stiffened panel with L-stiffeners presented in Table 4-3 is generated using the mean value of the input parameters. Then, new configurations are constructed by altering one of the input parameters while keeping the other unchanged and the resulting crack propagation profiles are compared.

This analysis is accomplished by increasing the overall cross-sectional area of the original investigated stiffened panel by 2.5% of the original value. The following five cases

are considered with increasing only the (a) main panel thickness, (b) stiffener web thickness, (c) stiffener flange thickness, (d) stiffener web height, and (e) stiffener flange width. The crack propagation profiles of the original and the new configurations of stiffened panels are shown in Figures 4-11(a) to 4-11(c). As shown in these figures, the fatigue service life increases as the cross-sectional area increases; higher values are also observed when the increase in the cross-sectional area is conducted by altering the main panel thickness or the web area of the stiffener. Increasing the main panel thickness by 2.5% can lead to a 12% increase in the fatigue service life, whereas this increase is only 10% and 8% for the web height and thickness, respectively. However, increasing the flange dimensions (i.e., flange width and thickness) have a low effect on the fatigue service life.

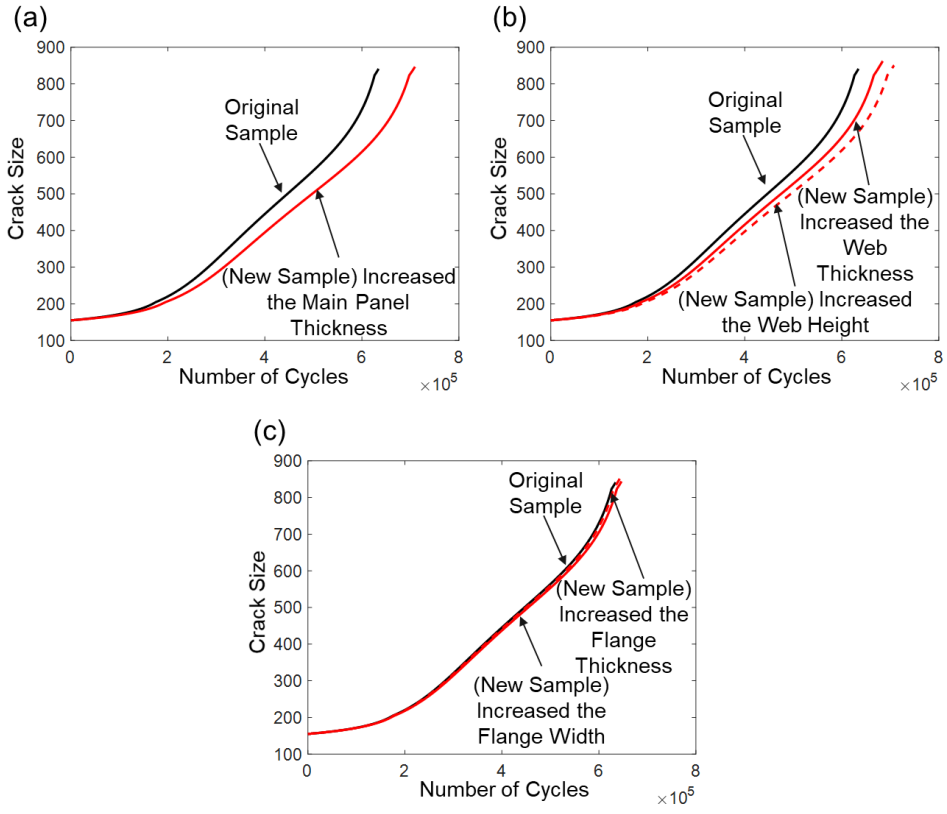

Figure 4-11. The crack propagation profiles of the stiffened panel with L-shaped stiffener and new configurations constructing by increasing the cross-sectional area in the (a) main panel (b) web of the stiffener, and (c) flange of the stiffener.

4.7.6. Fatigue Reliability of Stiffened Panels Considering Uncertainties in Geometric Parameters

The results of the sensitivity analysis indicated that the variability in the fatigue service life of stiffened panels depends not only on the variability of the mechanical properties, but also on the variability in several geometric parameters. Nevertheless, traditional reliability assessment approaches usually do not account for uncertainties in the geometric parameters. Accordingly, it was of interest to the authors to calculate and compare the reliability index of stiffened panels with and without considering the variability in the geometric parameters. To do such a comparison, the reliability index is first computed considering the uncertinaity in the geometry of the stiffeners and main panels, material properties, fracture resistance, and Paris's law regression parameters. The reliability analysis is illustrated on the stiffened panels with the random variables shown in Table 4-3. The Table also presents the statistical desriptos of these variables. Based on the results of a convergence analysis, four million samples are drawn from each random variable. Monte Carlo simulation is used to quantify the failure probability and reliability index using the performance function given by Equations (4-18).

Next, Monte Carlo simulation is performed again to determine the probability of failure and reliability index considering only the variability in material properties including the fracture resistance and Paris's law regression parameters. Figure 4-12 illustrates the reliability index of the investigated stiffened panels for two cases (i.e., with and without uncertainties in the geometric paramters). As shown, traditional reliability assessment approaches that do not properly consider the variability in geometric parameters may result in a higher reliability index compared to the case when this variability is considered. The reliability index of the stiffened panels calculated based on this assumption drops below a

target reliability index of 3.5 (Bhattacharya et al., 2001) after 664,835 cycles which is 73% higher than the case when the variability in the geometric parameters is included. Accordingly, neglecting the uncertainty in the geometric properties can lead to a non-conservative estimate of the fatigue reliability index.

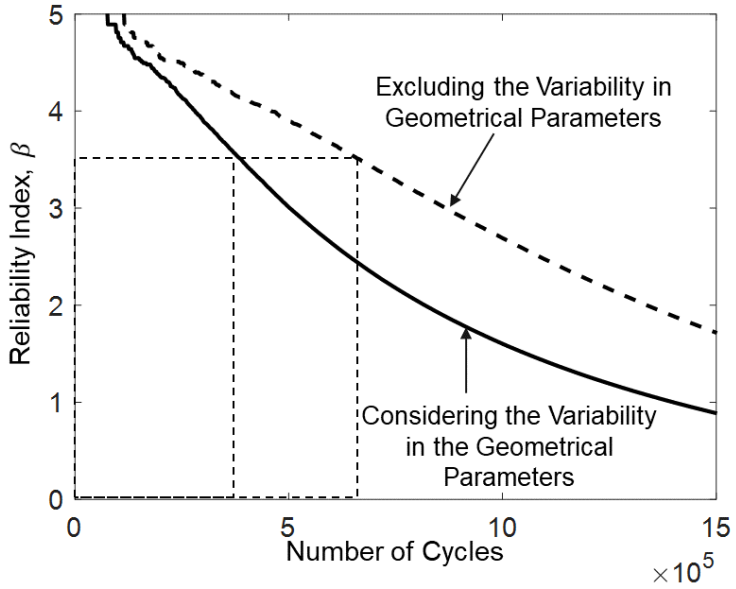

Figure 4-12. The reliability index of the investigated stiffened considering the variability in the mechanical and/or geometrical parameters.

4.8. Conclusions

This chapter presented the results of a sensitivity analysis of the fatigue crack propagation behavior in welded stiffened panels. A 3-D FE analysis, artificial neural network, and an elastic-plastic crack growth model are integrated to predict crack propagation under cyclic loading. The proposed approach is validated using experimental test data reported in literature. The sensitivity analysis is conducted to identify the key parameters that have a significant effect on the crack propagation behavior. The variability in the mechanical properties and geometric parameters of the panel is considered. Additionally, the effect of

neglecting the uncertainties associated with the geometric properties of the panel on the reliability index is evaluated. The following conclusions can be drawn:

- The proposed ANN-assisted simulation approach can provide accurate fatigue crack growth prediction for welded stiffened panels under the case of LSY conditions, the predicted crack growth profile agreed well with the experimental results.
- The results of the sensitivity analysis showed that the variability in both geometric parameters and mechanical properties has a significant influence on the variability of the fatigue service life of the stiffened panels.
- Among the mechanical properties of the material, the variability in the fatigue service life is strongly influenced by that associated with Paris' law material regression parameters (i.e., c_o and m_o). However, the modulus of elasticity and yield strength of the material have a low effect on the fatigue service life.
- Relative to the geometric parameters of the stiffened panel, the variability in the main panel thickness has a significant effect on the fatigue service life. Another influential parameter is the web characteristics (i.e., stiffener height and thickness). On the other hand, the variability in the properties of the flange (i.e., flange width and thickness) seem to have a minimal contribution to the variability in the fatigue service life.
- The reliability analysis conducted on the investigated stiffened panels showed that neglecting the uncertainties associated with the geometric properties can lead to a non-conservative estimate of the fatigue reliability index..

CHAPTER V

COMPREHENSIVE QUANTIFICATION OF THE RELIABILITY OF SHIP HULLS UNDER PROPAGATING FATIGUE CRACKS

5.1. Overview

Traditional approaches for reliability assessment of ship hulls under propagating cracks mostly rely on comparing the value of a certain fracture mechanics parameter calculated at the crack tip to the fracture toughness of the material. This assumption may not accurately represent the failure event since the fracture resistance is not only affected by the material properties but also by the component geometry. Furthermore, this approach may not properly account for the possibility of elastic-plastic fracture in the ship hull. This chapter presents a novel probabilistic approach for quantifying the reliability of ship hulls under propagating fatigue cracks. The approach utilizes the failure assessment diagram (FAD) to define the performance function of the hull and can account for the occurrence of various possible failure mechanisms ranging from brittle fracture to full plastic collapse. The Weibull stress criterion is utilized to quantify the critical crack tip opening displacement which is adopted herein to represent the fracture resistance of the cracked hull. MCS is used to quantify the failure probability and the reliability index of the ship hull under encountered wave loads and propagating cracks. The approach is illustrated on a tanker operating in the Atlantic Ocean.

5.2. Background

Detectable fatigue cracks are commonly observed in marine structures during routine inspections (Hodapp et al., 2015). When fatigue cracks reach their critical size, sudden fracture failure or yielding of the reduced section may occur, which may lead to catastrophic collapse. As a result, it is essential to develop proper fatigue assessment techniques that can help maintain acceptable reliability levels of ship hulls during their service life. Fatigue life prediction and damage assessment can be performed using the stress-life (S-N) approach or methodologies based on fracture mechanics concepts. The S-N approach is commonly used during the design phase of a structure due to its simplicity and reasonable accuracy when compared to experimental fatigue crack propagation results (Doshi & Vhanmane, 2013). It is also adopted by several design specifications published by the European Committee for Standardization (Eurocode3, 2010), Det Norske Veritas (DNV) (DNV, 2015), International Association of Classification Societies (IACS) (IACS, 2022), and the American Bureau of Shipping (ABS) (ABS, 2020). However, the S-N approach cannot quantify the change in the crack size during the service life and may not be suitable to account for the input from in-service inspection and maintenance activities (Dexter & Pilarski, 2002). Since ship structures may operate with multiple cracks growing, it is essential to be able to predict the crack growth for proper assessment of the fatigue life.

Methodologies based on fracture mechanics allow for studying the crack condition in a given detail and predicting the crack growth throughout the service life. Under small-scale yielding (SSY) conditions, the linear elastic fracture mechanics (LEFM) can be applied to quantify the crack propagation rate as a function of the range of the stress

intensity factor (SIF), representing the stress conditions ahead of the crack tip, and experimentally obtained material regression parameters. The LEFM is applicable when the size of the plastic zone ahead of the crack tip is sufficiently small compared to the panel dimensions and the crack size. Several studies in literature adopted LEFM to predict fatigue crack propagation in stiffened panels commonly utilized in ship hull construction. Poe Jr (1971) developed a solution for the SIF for structural panels with riveted and integral stiffeners which was later refined by Nussbaumer (1994) to include the effect of residual stresses. A similar approach was utilized in Nussbaumer (1994) and Mahmoud and Dexter (2005) to investigate crack propagation in stiffened panels with different stiffener configurations and load patterns. These studies implemented LEFM to assess the propagation and compared the analytical SIF predictions to those obtained numerically using FE analysis. For a stiffened ship hull structure, the presence of stiffeners offers multiple potential load paths that can become active as a crack propagates through the hull. This level of redundancy allows the crack to grow considerably before the failure occurrence of the hull. In this situation, the LEFM may not be directly applicable and elastic-plastic fracture mechanics (EPFM) should be utilized (Anderson, 2017; Božić et al., 2011).

Another challenge associated with the fatigue assessment of ship hulls is the presence of significant uncertainties in the fatigue crack growth prediction process. The randomness in sea loading, variability in the mechanical properties of materials, and imperfect modeling techniques are among the main contributors to these uncertainties. Oftentimes, fatigue tests conducted under similar conditions would yield significantly different results due to these uncertainties (Huang et al., 2013). Accordingly, probabilistic

analysis is essential to evaluate the fatigue performance of structures over their service life while accounting for these uncertainties (Dong et al., 2018). In this context, several studies in literature focused on investigating the fatigue reliability of ship hulls utilizing LEFM to model the fatigue crack propagation. For instance, Feng et al. (2012) evaluated the fatigue reliability of stiffened panels in the presence of correlated propagating cracks. Huang et al. (2013) also studied the fatigue reliability of complex welded structural components subjected to multiple cracks. The crack propagation prediction was conducted using numerical FE modeling and LEFM while the first-order reliability method (FORM) was used to quantify the reliability. A similar approach was also utilized by Dong et al. (2018) to predict crack growth and quantify the reliability of welded joints subjected to stochastic loading. FE analysis coupled with LEFM was also implemented by Mahmoud and Riveros (2014) to quantify the fatigue reliability of stiffened panels using MCS.

The literature also includes several other studies that focused on evaluating the reliability of deteriorating ships subjected to corrosion damage and growing cracks (e.g., (Akpan et al., 2002; Moan & Ayala-Uraga, 2008)) and the implementation of reliability-based optimization of inspection, monitoring, or maintenance actions (e.g., (Guedes Soares & Garbatov, 1996; Kim & Frangopol, 2012; Soliman et al., 2015)). In most of these aforementioned reliability quantification studies, a performance function was defined based on LEFM concepts to quantify the failure probability and reliability index. This function uses the applied range of the SIF as the crack driving force (i.e., demand parameter) and the critical SIF as the resistance parameter. This performance function utilizing the SIF can only be used for relatively short crack sizes under LEFM assumptions and may not be applicable for long cracks that may propagate transversally across ship

hulls. In such cases, EPFM parameters (e.g., *J*-integral or the crack tip opening displacement (CTOD)) may provide a better representation of the crack driving force. Furthermore, this performance function assumes the fracture resistance to be equivalent to the fracture toughness of the material that is quantified by testing standard specimens (i.e., compact or deep-cracked bend specimens). This assumption may not accurately represent the hull failure event since the fracture resistance calculated at the crack tip is controlled by both the mechanical properties and component geometry (Kim et al., 2020). It is essential to account for the effect of the plastic constraint conditions when calculating the fracture resistance of a structural component (Ohata & Minami, 2012).

Other studies (e.g., (Feng et al., 2012; Huang et al., 2013)) defined the performance function as the difference between the time-variant crack size and the critical one. Again, LEFM is typically used to compute the time-variant crack size while the critical size is assumed based on engineering judgment, chosen as the minimum detectable crack size for planning inspection and maintenance activities, or computed based on the critical SIF. In addition to the complexities associated with quantifying the critical crack size and the potential errors arising from the simplified assumptions, this performance function, and the one discussed above, account only for the possibility of brittle fracture failure and may not be valid under considerable plastic conditions. In these situations, which can be encountered in the hull structure, the plastic deformations can increase the occurrence probability of ductile failures and should not be ignored.

Based on this review, it seems that the reliability quantification of ship hulls under growing cracks requires fundamental enhancements before rational and realistic estimates of the failure probability can be established. First, a new performance function that can

account for different potential failure mechanisms ranging from brittle fracture to plastic collapse should be defined. Second, the developed approach should be able to model the crack propagation under large-scale plasticity conditions that may occur in ship hulls as the crack size increases. Finally, the resistance to sudden fractures should be properly quantified to represent the actual geometry and mechanical characteristics of the hull girder.

This chapter addresses these needs and proposes a novel approach for quantifying the fatigue reliability of stiffened ship hulls with long propagating fatigue cracks. The approach utilizes the failure assessment diagrams (FAD) (BSI, 2015) to define the performance function which enables accounting for a wide spectrum of failure modes ranging from fully plastic collapse to brittle fracture. The Weibull stress criterion (Beremin et al., 1983) is implemented to correlate the fracture resistance obtained from laboratory testing on standard coupons to the fracture resistance of the ship hull under propagating cracks. The critical CTOD is adopted to represent the fracture resistance while accounting for large-scale plasticity conditions that may occur in ship hulls as the crack size increases. Uncertainties associated with loading, material properties, and modeling technique are considered in the fatigue crack propagation prediction process. MCS is used to quantify the failure probability and reliability index of the ship hull under the encountered wave loads and propagating cracks. The approach is illustrated on a tanker operating in the Atlantic Ocean.

5.3. Prediction of Ship Hull Loads

Ship hulls can be subjected to different loading types such as dynamic (wave-induced), static (still water), and thermal loads (Decò et al., 2012). When evaluating the fatigue

reliability of ship hulls, wave-induced and still water loads are the two main stressors (Guedes Soares & Teixeira, 2000); accordingly, they will be used to estimate the load effects in this chapter. Analysis of available historical data is used herein to establish a realistic estimation of ship hull loads. Historical records, often available in terms of wind or wave characteristics at specific spatial resolutions, are used to generate wave-induced loads. The fifth-generation climate reanalysis dataset (ERA5) dataset, developed by the European center for medium-range weather forecasts (ECMWF, 2022), provides historical data with 0.25^{o} and 0.5^{o} grids at 6 hours of temporal resolution for a timespan ranging from 1976 to 2020 (Hersbach et al., 2019). To generate realistic loading conditions similar to those encountered by a ship during its service life, the loads generated across principal navigation routes are analyzed and used to predict fatigue crack propagation. Eight principal trans-oceanic routes in the Atlantic are identified based on Rodrigue et al. (2016) and Vettor and Guedes Soares (2015). The wave-induced loads encountered by a ship operating in each of these navigation routes are generated and used in the fatigue reliability assessment.

Linear strip theory (Hansen, 1994) is used to simulate the interaction between sea waves and the ship hull and to quantify wave-induced vertical bending moment (VBM) acting on the ship structure. The computer program SPECTRA (Michaelson, 2000) is used to generate response amplitude operators (RAOs) of the VBM considering several variables such as sea states, ship speed, and heading angle. SPECTRA is capable of generating RAOs that cover both wave-induced (low frequency) and slam-induced (high frequency) bending moments in lateral, vertical, and torsional directions (Sikora, 1998). The Joint North Sea Wave Project (JONSWAP) spectra (Hasselmann et al., 1973) is

employed to construct the wave-induced load profiles using the adopted historical wave data. The JONSWAP spectrum is defined as (Hasselmann et al., 1973):

$$S_{\omega}(\omega) = \alpha \frac{g^2}{(2\pi)^4} (T)^5 \exp\left(-\frac{5}{4} (\frac{\omega_p T}{2\pi})^4\right) \gamma^{exp\left[-\frac{(\frac{2\pi}{T}-\omega_p)^2}{2\sigma^2\omega_p{}^2}\right]} \quad (5\text{-}1)$$

where T is the average wave period, ω_p is the frequency at the spectral peak, γ is the peak enhancement factor, σ is the peak shape parameter, α is the Philips constant which is expressed as a function of the significant wave height (SWH) as $\alpha = 4.5\,(\frac{\omega_p}{2\pi})^4 SWH^{\,2}$ (Ochi, 2003).

Based on the generated the RAOs and sea spectrum parameters, the response spectrum for the wave-induced load effect $S_M(\omega_{e,U,H})$ can be found as (Hughes, 1983; Sikora, 1998):

$$S_M(\omega_{e,U,H}) = \left|\mathrm{F}_i(\omega_{e,U,H})\right|^2 S_{\omega}(\omega_{e,U,H}) \quad (5\text{-}2)$$

where, $\mathrm{F}_i(\omega_{e,U,H})$ and $S_{\omega}(\omega_{e,U,H})$ represent the RAO for wave-induced VBM and the wave spectrum, respectively, given the encountered frequency (ω_e) at speed (U) and heading angle (H).

If information regarding cargo conditions is not available, the design bending moments can be used to estimate the still water bending moment under service conditions. This chapter assumes that the still water bending moment follows a normal distribution with a mean equal to 63% of the design still water bending moment and a coefficient of variation of 20% (Hørte et al., 2007). The design values of sagging ($M_{sw,sag}$) and hogging ($M_{sw,hog}$) still water bending moments at each cross-section along the ship length are estimated based on IACS (2022) as:

$$M_{sw,sag} = 0.05185 f_{sw} C_{wv} l^2 b (C_b + 0.7) \quad (5\text{-}3)$$

$$M_{sw,hog} = 0.01 f_{sw} C_{wv} l^2 b(11.97 - 1.9C_b) \quad (5\text{-}4)$$

where f_{sw} is the factor accounting for the variation of VBMs along the vessel length (with 1.0 at midship), C_b is the ship block coefficient, l is the ship length (m), b is the ship breadth (m), and C_{wv} is a wave coefficient calculated as follows (IACS, 2022):

$$C_{wv} = \begin{cases} 10.75 - \left(\frac{300-l}{100}\right)^{1.5} & 150 \le l \le 300 \\ 10.75 & 300 \le l \le 350 \\ 10.75 - \left(\frac{l-350}{150}\right)^{1.5} & 350 \le l \le 500 \end{cases} \quad (5\text{-}5)$$

More information on utilizing the historical data to generate the wave-induced loads across the adopted navigation routes can be found in Tamimi et al. (2022).

5.4. Fatigue Crack Propagation in Stiffened Panels

The crack propagation in stiffened panels can be analyzed using several analytical models. Among those, the Paris and Erdogan (1963) model is widely adopted to characterize fatigue crack propagation under constant amplitude loading based on LEFM concepts. This model quantifies the crack growth rate *da*/*dN* as:

$$\frac{da}{dN} = c_0(\Delta K)^{m_0} \quad (5\text{-}6)$$

where da is the increment of crack length, dN is the number of cycles corresponding to the crack increment, c_0 and m_0 are regression parameters, and ΔK is the range of the SIF. If plastic conditions are expected to govern the crack growth, the EPFM parameter CTOD may be employed to represent the crack driving force. The crack growth rate can then be computed as (McEvily, 1973):

$$\frac{da}{dN} = C_{CTOD}(\Delta CTOD)^{m_{CTOD}} \quad (5\text{-}7)$$

$$m_{CTOD} = \frac{m_0}{2} \quad (5\text{-}8)$$

$$C_{CTOD} = \left(\frac{\sigma_y}{d}\right)^{\frac{m_0}{2}} E^{\frac{m_0}{2}}.c_0 \quad (5\text{-}9)$$

in which E is the modulus of elasticity, σ_y is the material yield strength, and d is the plastic constraint factor (d =1 for plane stress and 2 for plane strain condition). Note that, under elastic conditions, the SIF can be computed as a function of the CTOD as (Irwin, 1957):

$$\Delta K = \sqrt{d \times E \times \sigma_y \times \Delta CTOD} \quad (5\text{-}10)$$

Since the model given by Equation (5-7) can be used in both SSY and large-scale yielding (LSY) conditions, it is adopted in this chapter to predict the crack growth under the established sea loading. Section 5.9.1 of this chapter presents an in-depth discussion on the criteria for evaluating the plasticity condition within stiffened hulls.

Crack propagation in stiffened panels is significantly influenced by residual stresses induced during construction procedures and welding (Dexter et al., 2003; Nussbaumer et al., 1999). In this chapter, the idealized residual stress distribution recommended by Faulkner. (1975) is adopted to model the residual stresses in the main panel and stiffeners. This model defines a triangular stress distribution for the tensile regions around the stiffeners as shown in Figure 4-1. The width of the tensile zone is proportional to the plate thickness and the constant η, which is generally assumed in ship structures to range from 3 to 4 depending on the stiffened panel geometry and welding conditions (Nussbaumer et al., 1999). The maximum value of the tensile residual stress at the location of the stiffener is assumed to be equal to the yield stress of the plate material. The remaining regions are subjected to residual compressive stresses. The magnitude of these stresses is determined by satisfying the equilibrium condition between the tensile and compressive forces. A similar concept is employed to calculate the residual stress occurring in the stiffeners following (Božić et al., 2014; Rahman et al., 2020).

5.5. Fracture Resistance Measures

The fracture toughness calculated utilizing standard specimens usually underestimates the actual fracture resistance of large-scale structural components (Prakash, 2009). This can be attributed to the difference in crack tip plastic constraints between the standard specimen and the actual component; especially when the structure is exposed to large deformations (Ohata & Minami, 2012). A more realistic estimate of the fracture resistance of structural components under service conditions can be established through a correlation process between the fracture toughness of standard fracture specimens and the actual specimen configurations. The Weibull stress criterion is utilized herein to establish this correlation (Beremin et al., 1983).

In this approach, a probabilistic characterization of the instability of microcracks is obtained by integrating the near crack-tip stresses over the fracture process zone V_f. This leads to the Weibull stress σ_w defined as (Beremin et al., 1983)

$$\sigma_w = \left[\frac{1}{V_o}\int_{V_p} {\sigma_{eff}}^m dV_P\right]^{1/m} \tag{5-11}$$

where V_p is the volume of the plastic zone near the crack tip, σ_{eff} is the effective stress for fracture, generally considered as the maximum principal stress, whereas m represents the shape factor that reflects the distribution of microcracks within the material (Minami et al., 1992), and V_o is a reference volume. This reference volume has to be small enough to avoid stress gradients and large enough to increase the probability of detecting a microcrack with a reasonable length (Beremin et al., 1983). The value of V_o is considered herein as 1 mm^3 based on Ohata and Minami (2012), Sarzosa et al. (2018), and Yusuke et al. (2017). The critical Weibull stress at fracture is considered as a material property that is independent of

the specimen configuration, size, and loading condition (Ohata & Minami, 2012; Yusuke et al., 2017). This feature allows correlating fracture conditions between different specimen configurations. The approach adopted herein to assess the fracture condition of the structural component is depicted in Figure 5-1. The figure shows a standard fracture toughness specimen (i.e., compact tension C(T) specimen) and a ship hull section representing the structural component under investigation. For these two components, three-dimensional FE models are constructed and used to compute the Weibull stress at different CTODs, as shown schematically in Figure 5-1. The C(T) specimen exhibits higher Weibull stress under the same CTOD level due to the larger fracture process zone V_f compared to the ship hull. Based on the Weibull stress criterion, the critical Weibull stress $\sigma_{w,cr}$ can be obtained at the critical CTOD of a standard fracture toughness specimen $\delta_{ss,cr}$, then the critical CTOD of the structural component $\delta_{structure,cr}$ can be computed at the critical Weibull stress $\sigma_{w,cr}$ for different crack sizes.

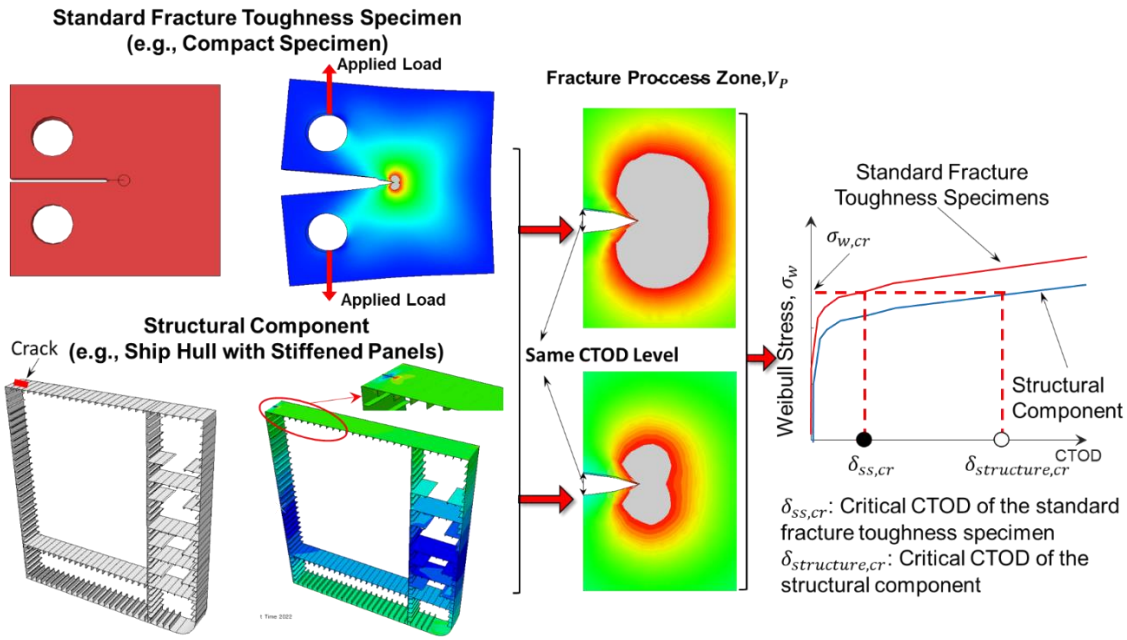

Figure 5-1. A schematic representing the Weibull stress criterion adopted to quantify the fracture resistance.

5.6. Failure Assessment Approach

Ship hulls under propagating cracks are prone to various potential failure mechanisms ranging from brittle fracture to fully plastic collapse (Mahmoud & Dexter, 2005). Defining a performance function that accounts for the possibility of fracture failure only may not provide a rational prediction of the reliability levels. Accordingly, it is essential to account for these potential failure mechanisms. This is accomplished in this chapter through the application of the FAD (BSI, 2015). The FAD can be looked at as an interaction diagram of different failure modes that can be used to determine, given the crack size, whether the condition of this crack is acceptable or not. This method enables the assessment of various failure modes in the structural component including, fully plastic collapse, brittle fracture, and elastic-plastic fracture. The FAD consists of a vertical axis, a horizontal axis, and an assessment curve. The vertical axis represents a measure of the applied stress conditions required to cause a sudden (i.e., brittle) fracture while the horizontal axis provides a

measure of the applied load required to cause plastic collapse. The assessment curve is plotted to define the capacity limits. Given the loading condition and crack size at a given time, the actual state of the structure is represented by an assessment point. The location of this assessment point can then be compared to the plotted assessment curve to determine whether the flaw or crack is acceptable or not. An assessment point that lies within the region bounded by the assessment curve is considered acceptable, while a point outside the bounded region is deemed unacceptable.

The FAD has three assessment options outlined in the British Standard, BSI 7910 (BSI, 2015), namely options A, B, and C. The most suitable option is generally selected based on the accuracy required for the analysis and the availability of information to create the FAD. Option A is suitable for cases where detailed stress-strain data is not available, option B requires actual uniaxial stress-strain data of the material, while Option C uses numerical analysis to generate the FAD. Option A is only appropriate when limited information on the material properties or the external forces is available as it does not require detailed stress-strain data of the material. Option B is suitable for all types of structures when the required data is available (BSI, 2015). Option C generates the assessment line for a specific material and geometry and requires additional FE simulations to generate the FAD. For this investigated problem, Options B or C can be used to assess the failure probability; however, Option B is utilized to maintain a reasonable computational cost for the probabilistic simulations (Horn & Sherry, 2012).

For utilizing the FAD, the assessment point is defined with two parameters, the load ratio (L_r) and fracture ratio (δ_r). The load ratio is defined as (BSI, 2015):

$$L_r = \frac{\sigma_{ref}}{\sigma_y}, \tag{5-12}$$

in which σ_{ref} is the reference stress, and σ_y is the yield strength of the material. When using the CTOD to assess the possibility of brittle fracture, the fracture ratio $K_{r_{ap}}$ can be defined as (Ohata & Minami, 2012):

$$K_{r_{ap}} = \sqrt{\frac{\delta}{\delta_{structure,cr}}} \tag{5-13}$$

where δ is the CTOD occurring under a given crack size and applied loads considering residual stresses and $\delta_{structure,cr}$ is the critical CTOD of the structure calculated based on the Weibull stress criterion. equivalent CTOD concept. For materials that may exhibit yield discontinuity, the assessment curve for Option B is expressed as:

$$K_{r_{ac}}(L_r) = \begin{cases} \left(\frac{E\times\varepsilon_{ref}}{L_r\times\sigma_y} + \frac{{L_r}^3\times\sigma_y}{2\times E\times\varepsilon_{ref}}\right)^{-1/2} & L_r < L_{r,max} \\ 0 & L_r > L_{r,max} \end{cases} \tag{5-14}$$

where ε_{ref} is the true strain at the true stress $\sigma_{ref} = L_r \times \sigma_y$, E is the modulus of elasticity, and $L_{r,max}$ is the maximum cut-off value for L_r defined to prevent local plastic collapse and is calculated as:

$$L_{r,max} = \frac{\sigma_y+\sigma_u}{2\times\sigma_y} \tag{5-15}$$

where σ_y and σ_u are the tensile yield and ultimate strengths of the material, respectively.

After constructing the assessment curve, the assessment point is plotted on the FAD and is considered acceptable if it lies within the region bounded by the assessment curve and the axes. To further illustrate this concept, a typical Option B FAD is shown in Figure 5-2(a) for high-strength steel material 350WT (CSA, 2018). The stress-strain behavior of this steel type is shown in Figure 5-2(b) (Dehghani et al., 2017). The FAD is divided into three zones as shown in Figure 5-2(a). Zone I is defined as the area above the line originating from the origin and intersecting the assessment curve at $L_r = 0.62$ while Zone

III falls within the area below the line from the origin to the assessment curve at $0.95 \times L_{r,max}$. Zone II is the remaining area underneath the assessment line. Zone I represents brittle fracture-controlled failures while a failure in Zone II tends to be an elastic-plastic fracture. Finally, if the assessment point lies in Zone III, the failure is caused by the plastic collapse.

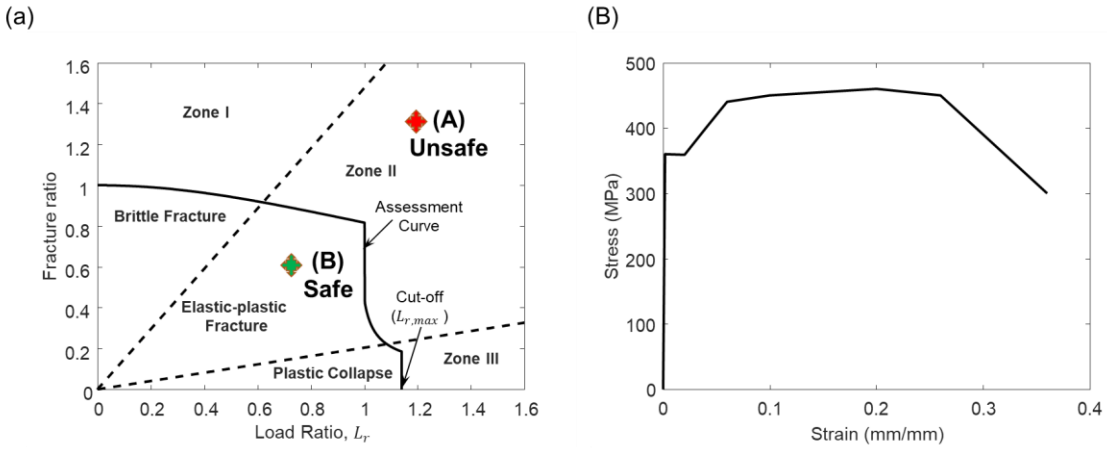

Figure 5-2. (a) A typical Option B FAD and (b) stress-strain curve of the 350WT steel.

5.7. Performance Function and Failure Probability

To assess the failure condition, the assessment points, given the vector of random variables ($\boldsymbol{X}$), at a certain crack size (a) are compared to the generated FAD assessment curve. Accordingly, the following performance function (g) can be defined to compute the failure probability:

$$g(\boldsymbol{X}, a, L_r) = K_{r_{ap}}(\boldsymbol{X}, a, L_r) - K_{r_{ac}}(\boldsymbol{X}, L_r) \tag{5-16}$$

where $K_{r_{ap}}(\boldsymbol{X}, a, L_r)$, representing the demand, is the fracture ratio associated with a particular assessment point (calculated using Equation (5-13)) at a specific crack size and load ratio given the vector of random variables, while $K_{r_{ac}}(\boldsymbol{X}, L_r)$, representing the capacity, is the fracture ratio of the assessment curve at the same load ratio for the

corresponding random variables (calculated using Equation (5-14)). This performance function is next implemented into a MCS process to calculate the probability P_f of the demand exceeding the capacity as:

$$P_f(a) = P[g(\boldsymbol{X}, a) \geq 0] \tag{5-17}$$

Finally, the reliability index β is determined as:

$$\beta(a) = \Phi^{-1}\left[1 - P_f(a)\right] \tag{5-18}$$

where $\beta(a)$ is the reliability index at crack size a and Φ is the cumulative density function (CDF) of the standard normal distribution.

5.8. Reliability Assessment Framework

The proposed reliability assessment framework contains three interconnected modules. Module I focuses on estimating the loads acting on the ship hull, Module II predicts the crack propagation along the service life of the ship hull, while Module III is responsible for analyzing the potential failure mechanism and quantifying the fatigue reliability of the investigated structure utilizing the failure assessment diagram. Module I starts with characterizing potential navigation routes and defining the ship geometry. Historical wave data are next obtained from the ERA5 database to establish the wave characteristics across the defined routes. The operational conditions along the route are determined and used for computing the RAOs. JOWNSWAP spectrum is next used to calculate the sea wave spectrum. The vertical bending moment associated with each route is then found using Equation (5-2) and several realizations of the VBM are generated for the defined routes.

Module II starts with developing a 3-D FE model of the ship hull. The model is utilized to quantify the crack driving force in conjunction with the analytical crack advancement rule (i.e., Equation (5-7)) under external loads and residual stresses. Module III starts with

defining the statistical descriptors of the underlying random variables (e.g., c_0 and m_0) and conducting crack propagation analysis. The established crack propagation profiles corresponding to different VBM realizations are discretized into small segments and the applied loads within each segment are quantified. The developed FE model of the ship hull is utilized to evaluate the demand measure (e.g., von Mises stresses and actual CTOD) for each load cycle within the segments. Next, the fracture ratio of the assessment curve at the same load ratio for each cycle is calculated using Equation (5-14). The performance function defined in Equation (5-16) is used to compute the probability of failure defined based on the difference between the fracture ratio of the assessment point and that of the assessment curve for a particular load sample and crack size. MCS is used next to calculate the failure probability and reliability of the ship hull under propagating cracks. A layout of the proposed framework is presented in Figure 5-3.

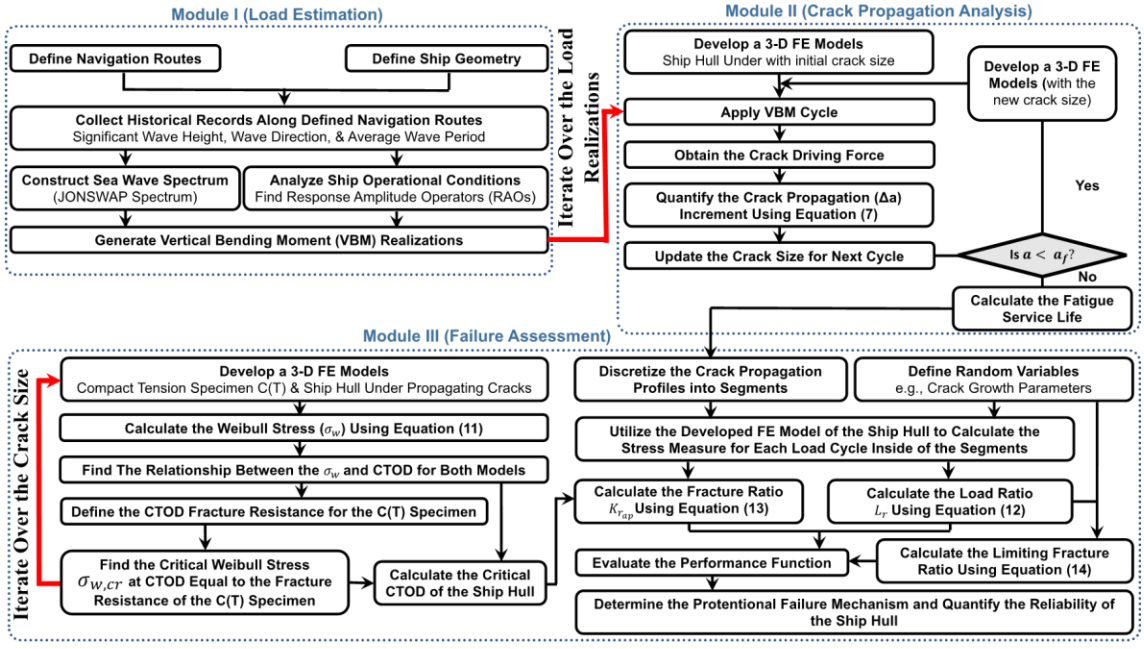

Figure 5-3. A layout of the framework proposed for quantifying the reliability of ship hulls under propagating cracks.

5.9. Illustrative Example

The proposed framework is illustrated on a tanker investigated in Dinovitzer (2003). The tanker is a double-hulled structure with a length of 324.5 m, depth of 31.2 m, and a beam of 57 m. A center, through-thickness, fatigue crack at the mid-section of the deck is assumed to initiate and propagate transversally through the stiffened panel. Figure 5-4 shows a cross-sectional view of the tanker. The ship is assumed to operate in the Atlantic Ocean with an average speed of 15 knots knots (Lindstad & Eskeland, 2015) along the trans-oceanic passages analyzed in Tamimi et al. (2022) and defined based on Vettor and Guedes Soares (2015) and Rodrigue et al. (2016). Figure 5-5(a) shows these considered routes. Next, historical wave data across the Atlantic Ocean are adopted from the ERA5 reanalysis dataset (Hersbach et al., 2019). Wave data are utilized to construct the wave energy density spectrum and project the wave-induced VBM profiles for the selected routes. It is assumed that the ship navigates randomly across the identified routes during its service life. Figure 5-5(b) shows the generated wave-induced VBM along Route 1 during the 1990-2020 timespan using this approach. This route is also highlighted in Figure 5-5(a). The effects of still water bending moments are estimated based on design loads calculated using Equation (5-3) to (5). It is assumed that the still water bending moment follows a normal distribution with a mean value equal to 63% of the design still water bending moment and a coefficient of variation of 20% (Hørte et al., 2007). Finally, the total load effects are calculated as the summation of the still water and wave-induced VBMs.

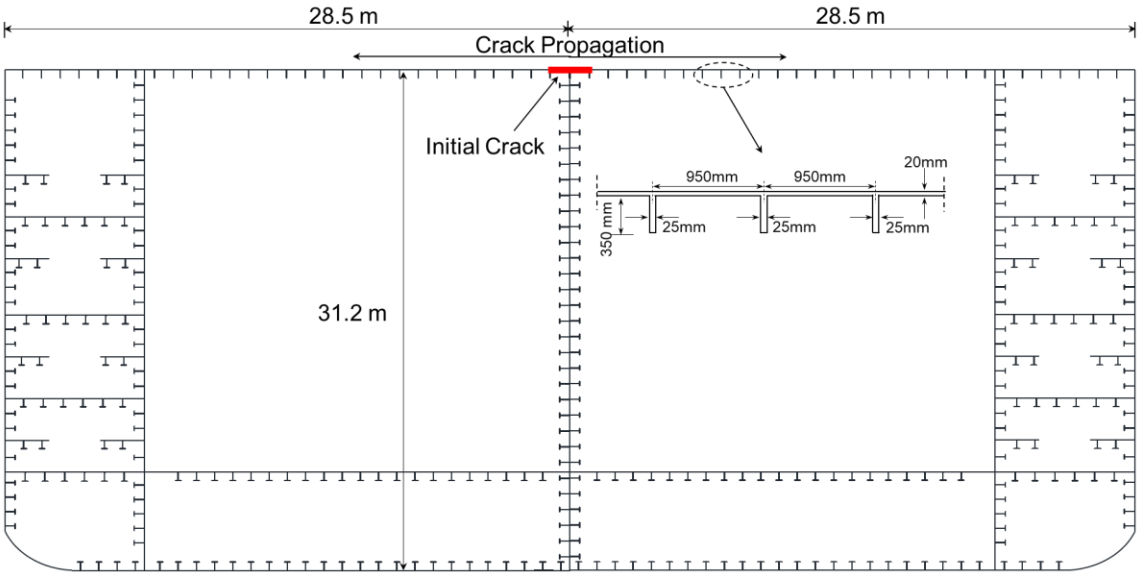

Figure 5-4. A View of the mid-section of the investigated tanker.

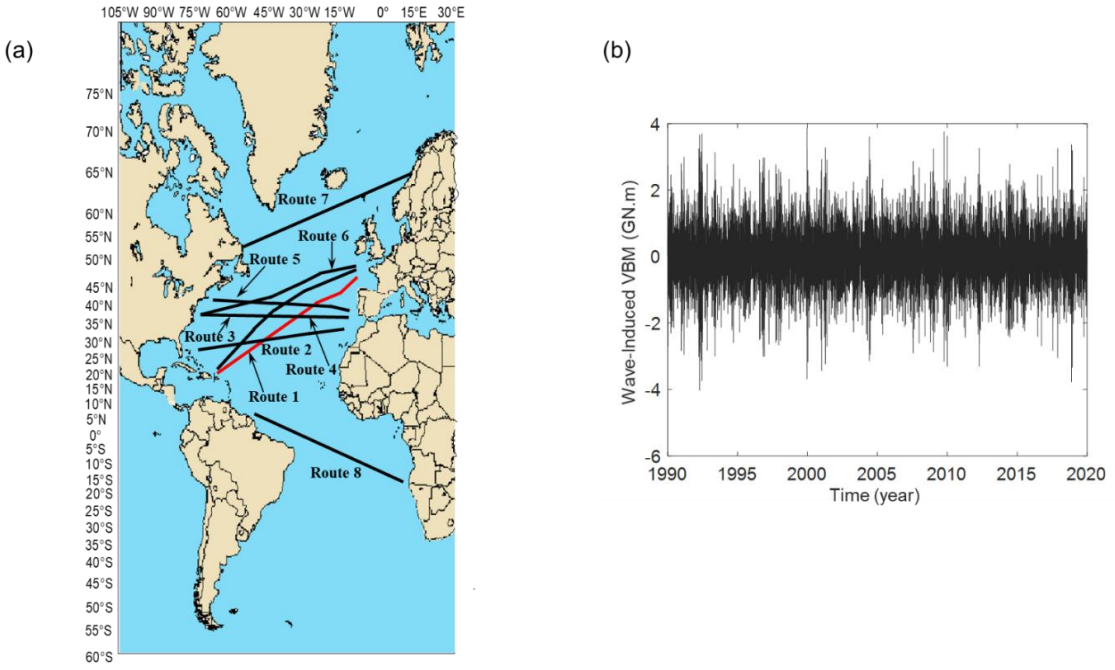

Figure 5-5. (a) The defined ship navigation routes in the Atlantic Ocean (b) the generated wave-induced VBM along Route 1 during the 1990-2020 timespan using the ERA5 reanalysis dataset.

In this example, it is assumed that the tanker is constructed using 350WT steel (Dehghani et al., 2017). To account for the uncertainties associated with the fatigue crack

growth prediction, the yield strength, ultimate strength, material fracture toughness, and modulus of elasticity, as well as the regression parameters c_o and m_o are considered as random variables. The statistical descriptors of these variables are presented in Table 5-1. Given these material uncertainties, the assessment curve of the FADs can be constructed based on the defined random variables as shown in Figure 5-6. To compute the crack driving force and assess the failure conditions, a 3-D FE model of the ship cross-section is constructed and analyzed in ABAQUS environment (Simulia, 2018). A view of the FE model is shown in Figure 5-7. The stiffeners and plates are modeled using reduced integration four-node shell elements (S4R element). Boundary conditions are applied at Point A and Point B along the neutral axis of the cross-sections to simulate the bending behavior of the section. Translations in the x, y, and z directions and the rotation around the z-axis are prevented at Point A, while only translations in the x and y axes are restricted at Point B (Decò et al., 2012). The loading (i.e., VBM) is applied about the *x*-axis at point B. Given the symmetry of the cross-section and the loads applied along the *y*-*z* plane, only half of the cross-section was simulated to reduce the computational time.

Table 5-1. The statistical descriptors of the considered random variables

Variable	Distribution Type	Mean	COV	Reference
c_0*	Normal	$6.8*10^{-9}$	0.055	(Barsom & Rolfe, 1987; DNV, 2015)
m_0*	Normal	3.1	0.1	(DNV, 2015)
$\delta_{ss,cr}$	Normal	0.1 mm	0.15	(Feng et al., 2012; Kayamori & Kawabata, 2017)
σ_y	Lognormal	353 MPa	0.083	(Hess et al., 2002)
σ_u	Normal	490 MPa	0.075	(Hess et al., 2002)
E	Normal	200 GPa	0.076	(Hess et al., 2002)
Still water VBM Ratio Bias (Applied/Design Value)	Normal	0.63	0.2	(Hørte et al., 2007)

* Correlation coefficient between c_0 and m_0 is -0.95 (Chung, 2004)

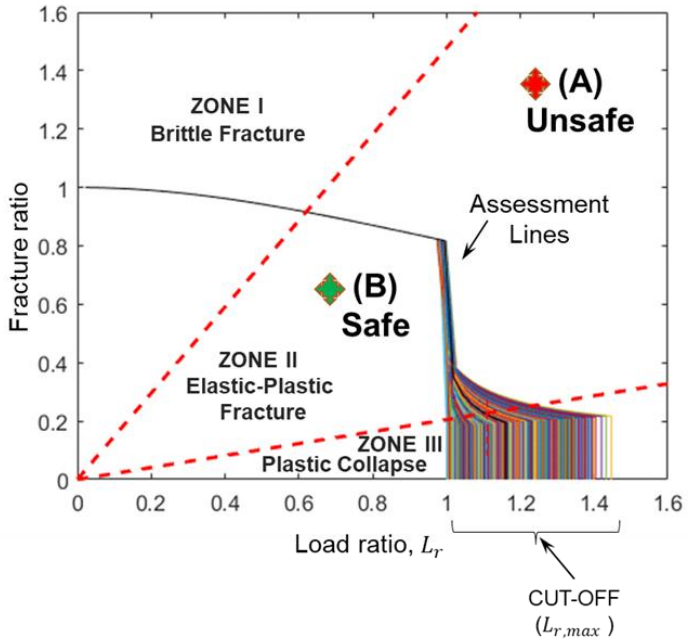

Figure 5-6. Option B FADs considering the uncertainties associated with material properties.

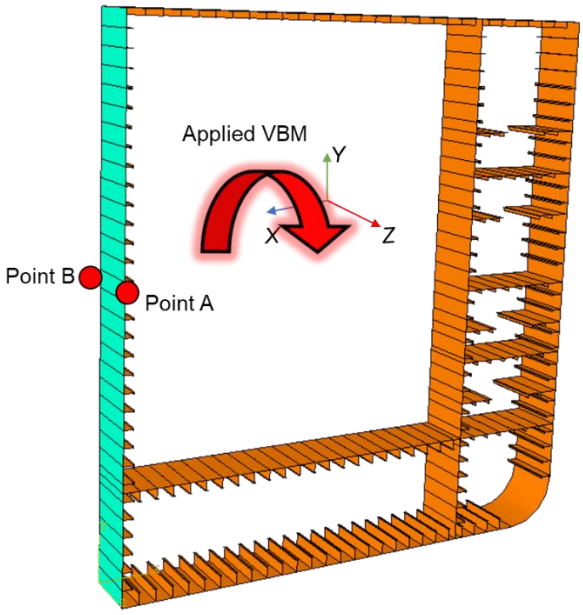

Point A: Translation along *x*,*y*, and *z* and rotation above z are prevented.
Point B: Translation along *x* and *y* directions are prevented.

Figure 5-7. The developed FE model of the ship hull, the defined constraints, and the applied VBM.

5.9.1. Crack Propagation Analysis and Demand Measures

The crack propagation analysis is conducted based on the model proposed in McEvily (1973) and presented by Equations (5-7) to (5-9). Crack sizes between 25 to 75 mm are generally considered detectable using regular visual inspections (Stenseng, 1996). Accordingly, this chapter assumes an initial crack size of 50 mm. For this type of structure, the crack growth can be significantly affected by the plasticity conditions ahead of the crack tip. For small crack sizes, SSY condition is expected to occur; however, as the crack propagates, LSY condition may occur and the LEFM assumptions may no longer provide accurate results. The approach proposed by Marques et al. (2021) is adopted in this chapter to evaluate the yielding condition within the stiffened hull under propagating cracks. This approach uses the CTOD to distinguish between SSY and LSY conditions. The approach quantifies the elastic ($\Delta\delta_e$) and plastic ($\Delta\delta_p$) components of the CTOD. SSY condition is found to govern the behavior when the ratio between the elastic component of the CTOD and the total CTOD (δ_t) is higher than 75% (Marques et al., 2021). LSY condition becomes dominant when this ratio is less than 60%. In these cases, the EPFM parameter CTOD is more suitable to model the crack growth.

To assess the yielding condition of the investigated ship hull, the total CTOD is measured from the developed FE model under the maximum possible bending moment at different crack sizes. Based on the load analysis discussed above, the maximum bending moment encountered due to both the still water and wave-induced loads was found to be 8 GN.m. At different crack sizes, the elastic and plastic components of the total CTOD are computed and the ratio of the elastic CTOD to the total CTOD, denoted as the degree of elasticity thereafter, is quantified. To illustrate this approach, the CTOD is measured from

the FE model at a crack size of 8.5 m for different values of VBM. The elastic and plastic components of the CTOD are also quantified and depicted in Figure 5-8(a). The degree of elasticity for this case was found to be 52%, which indicates that LSY conditions would occur under the considered loading condition and crack size.

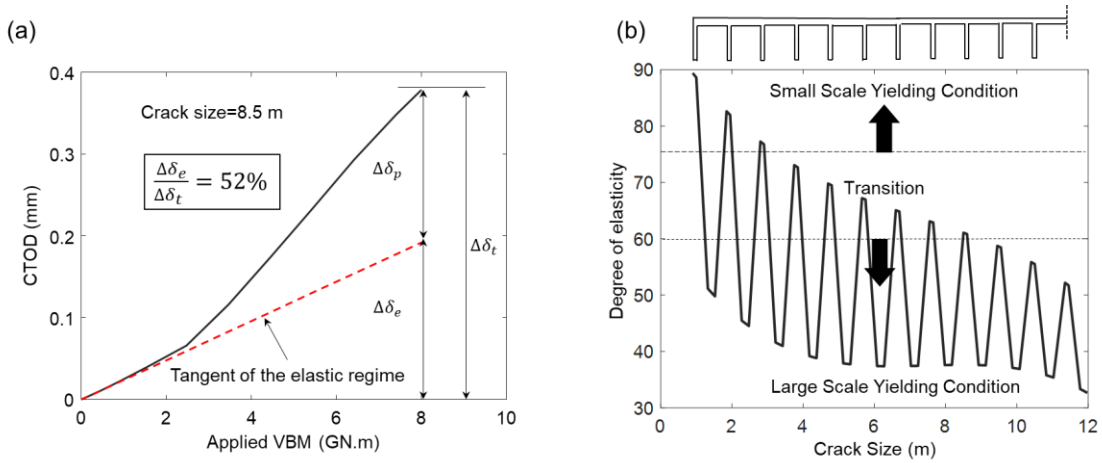

Figure 5-8. The crack tip yield conditions of the investigated ship hull: (a) CTOD versus the applied load at a crack size equal to 8.5 m and (b) the degree of elasticity as a function of the crack sizes under the maximum possible bending moment.

The analysis in Figure 5-8(a) is next conducted for crack sizes up to 12 m and the degree of elasticity is calculated as a function of the crack sizes and shown in Figure 5-8(b). As expected, the degree of elasticity for the investigated hull decreases as the crack propagates. The degree of elasticity was found to be above 75% only when the crack size is smaller than 1 m; up to this crack size, SSY conditions are dominant and LEFM can be used to model the crack propagation. Since this type of transversal crack may propagate beyond this limit (Nussbaumer et al., 1999), the CTOD is considered as the crack driving force in place of the traditionally adopted SIF to predict crack propagation.

To account for the uncertainty in the crack propagation, the crack growth profiles are established using Equations (5-7) to (5-9), along with the results from the FE model, considering the random variables defined in Table 5-1. Several VBM realizations (240

VBM realizations) are generated for the defined eight routes, and the time required for the crack to propagate from initial sizes of 0.05 m to 12 m is calculated for each of them. The statistical regression parameters of the Paris Law (c_0 and m_0) are considered as random variables in the crack propagation analysis. Figure 5-9 shows the mean crack propagation profile as a function of time, as well as the PDF of the time required to reach crack sizes of 4 and 8 m. This figure represents the average crack propagation profile obtained for all considered navigation routes. However, this analysis can be conducted on only specific routes if more information on the navigational profile of the ship is available.

After establishing the crack growth profiles, assessing the failure condition of the hull will be accomplished by estimating the fracture ratio computed at different load cycles and comparing it to the limiting fracture ratio obtained from the assessment curve under the same conditions. Accordingly, each crack propagation profile is discretized into segments of 0.25 m in length. Then the von Mises stress and resultant CTOD (i.e., demand measures) for each load cycle within the segment are calculated. The resultant CTOD represents the crack driving force due to applied loads and residual stresses. This process is conducted for all generated VBM realizations resulting in more than 6,000,000 samples of von Mises stress and resultant CTOD for each crack segment. These samples will be used to evaluate the assessment point and compute the reliability in the next sections.

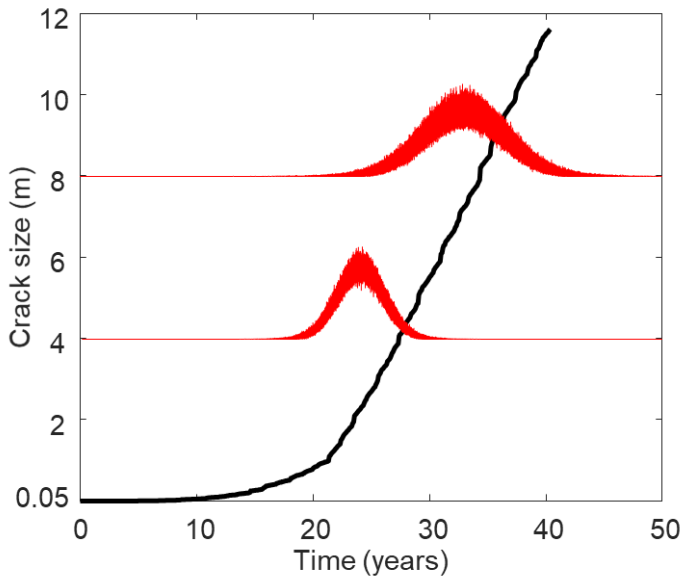

Figure 5-9. The crack growth profile as a function of time considering the uncertainties associated with the loading and material properties.

5.9.2. Fracture Resistance of the Ship Hull Under Crack Propagation

The Weibull stress criterion is adopted to quantify the .fracture resistance of the ship hull under the propagating crack. The fracture resistance of the hull is obtained based on the analysis of the material fracture toughness of a compact tension specimen (i.e., C(T) specimen). An ASTM E1290-08 (ASTM-E1290-08, 2002) standard specimen with the dimensions shown in Figure 5-10(a) is utilized for this process. A Nonlinear 3-D FE model representing the C(T) specimen is constructed in ABAQUS environment (Simulia, 2018). The FE model uses eight-node hexahedral elements with an element size of 0.05×0.05×0.2 mm near the crack tip. The mesh configuration consisted of 30 focused rings of elements in the radial direction that surrounds the crack tip. The model is adopted to provide the required crack tip stresses at the fracture process zone for computing the evolution of the Weibull stress σ_w with respect to the CTOD. The fracture process zone is defined as the region where the maximum principal stresses are equal to or greater than the yield stress

of the material. The crack tip stress fields were evaluated by increasing the magnitude of remote loading, then finding the volume of the fracture process zone and the corresponding maximum principal stress. An example of the 3-D FE model for the C(T) specimen and contours of maximum principal stress near the crack tip are shown in Figure 5-10(b). The Weibull stress is then calculated using Equation (5-11) for $m = 20$ (Ohata & Minami, 2012). The relationship between the σ_w and CTOD is shown in Figure 5-11(a). As seen in the figure, the Weibull stresses vary nonlinearly with the increasing CTOD (i.e., remote loading).

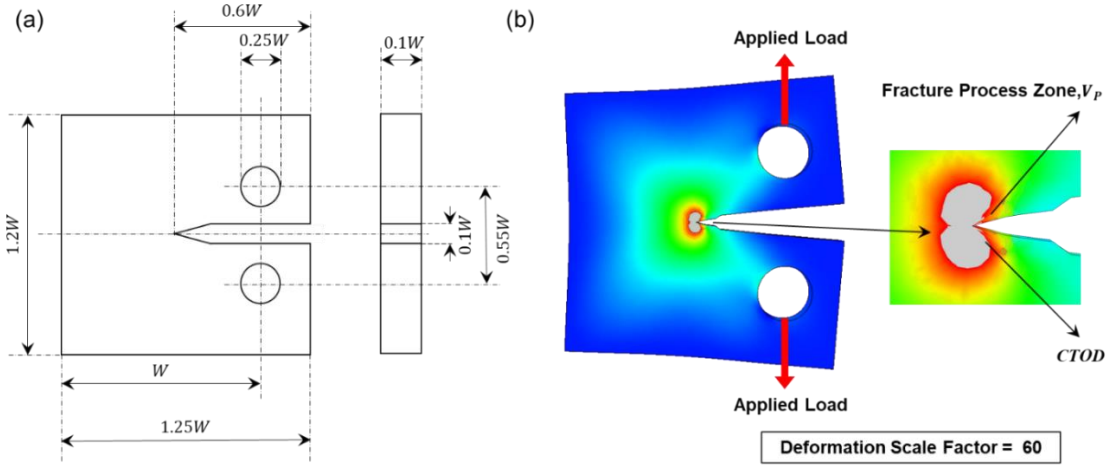

Figure 5-10. Standard ASTM E1290-08 (ASTM-E1290-08, 2002) C(T) fracture specimen: (a) the geometry and dimensions and (b) the developed finite element model, applied loads, contours of maximum principal stress near the crack tip, and fracture process zone.

The analysis presented in Figure 5-11(a) is next conducted on the 3-D model of the ship hull to compute its critical CTOD based on the data obtained from the fracture toughness specimen. The $\sigma_w - CTOD$ relationship is generated for crack sizes ranging from 0.5 m to 12 m. The volume of the fracture process zone and the corresponding maximum principle stress with increasing levels of remote loading are computed, then the Weibull stress is calculated using Equation (5-11). Figure 5-11(b) shows the σ_w – CTOD

relationships for various crack sizes. As shown in Figure 5-11(b), longer cracks result in higher Weibull stress under the same CTOD level due to the larger fracture process zone V_f and the change in plastic constraint conditions. The evolution of the Weibull stress with respect to the CTOD for the C(T) specimen is also plotted in Figure 5-11(b). The critical CTOD fracture toughness of the C(T) specimen is considered as a random variable that follows a normal distribution with a mean of 0.1 mm and a coefficient of variation (COV) of 15% (Feng et al., 2012; Kayamori & Kawabata, 2017; Lancaster, 1999). For illustration purposes, the mean value of this parameter is plotted in Figure 5-11(b), and the corresponding critical Weibull stress $\sigma_{w,cr}$ is obtained at this CTOD.

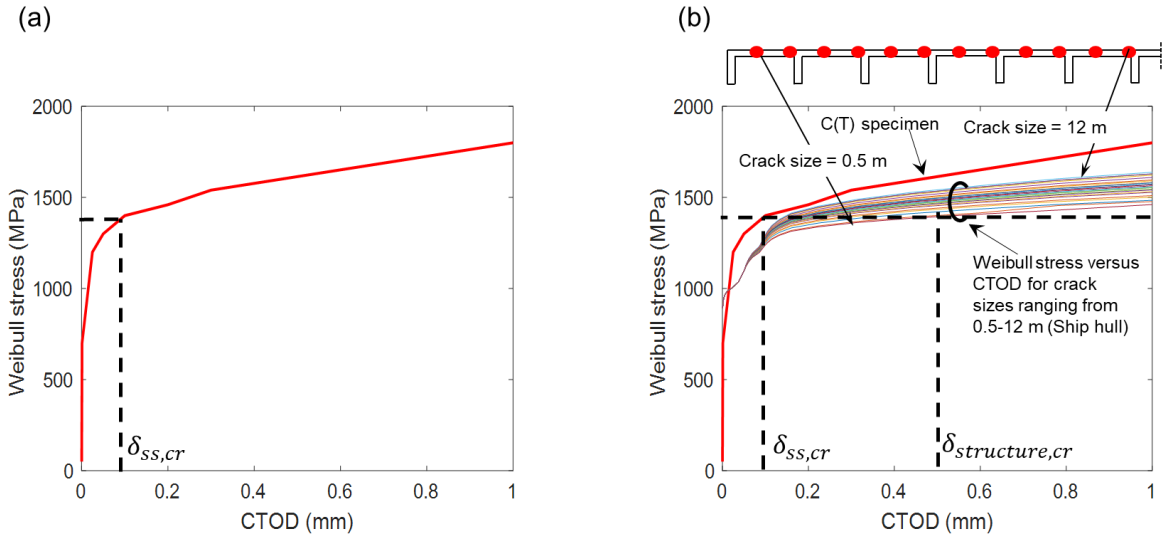

Figure 5-11. The Weibull stress σ_w versus the CTOD for: (a) the C(T) fracture specimen and (b) the ship hull under different crack sizes.

The critical CTOD of the ship hull can then be computed at the critical Weibull stress $\sigma_{w,cr}$ for different crack sizes as shown in Figure 5-12. The figure also shows the PDF of the critical CTOD at crack sizes of 5 and 8 m. As shown, the critical CTOD decreases as the crack propagates; higher values are also observed at stiffener locations due to the higher constraints induced by the stiffeners. These results are integrated into the

MCS to compute the reliability accounting for the uncertainties associated with the critical CTOD at different crack sizes.

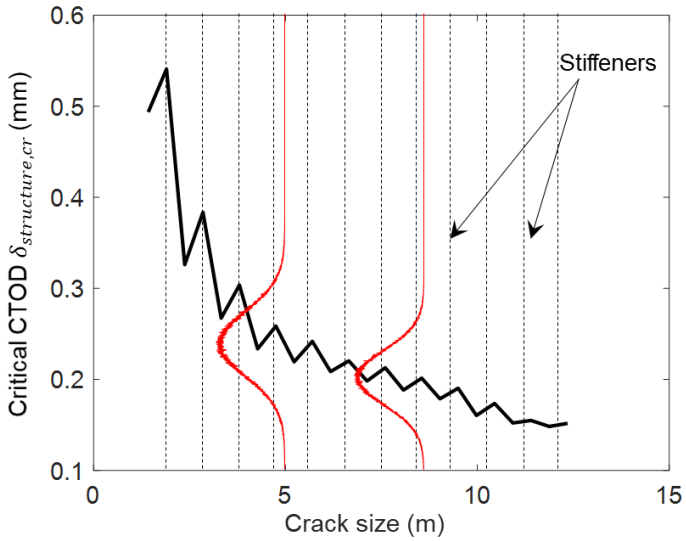

Figure 5-12. The critical CTOD of the ship hull at the critical Weibull stress for different crack sizes.

5.9.3. Failure Assessment and Reliability Analysis

The failure condition of the ship hull is next evaluated by computing the fracture ratio for the drawn samples (i.e., $K_{r_{ap}}$) and comparing it to the limiting fracture ratio (i.e., $K_{r_{ac}}$) obtained from the assessment curve under the same loading condition. The load and crack size dependent CTOD and von Mises stress necessary to obtain the assessment point are computed through the developed FE model as discussed earlier. At this stage, the fracture resistance (i.e., the critical CTOD) of the ship hull under a propagating crack has been also obtained as shown in Figure 5-12. Accordingly, all information necessary to compute the load and fracture ratio needed to define the assessment points is obtained. Next, the limiting fracture ratio obtained from the assessment curve at the same load ratio for each drawn sample is calculated using Equation (5-14). The uncertainties associated with the material

properties (i.e., modulus of elasticity, yield strength, and ultimate strength) are considered for calculating the limiting fracture ratio. The failure condition of each drawn sample is considered acceptable if the fracture ratio of the assessment point is less than the limiting fracture ratio. Figures 5-13(a) and 5-13(b) show 3-D views of the simulated assessment points and the mean assessment curve at a crack size ranging between 0-6 m, and 6-12 m, respectively. The number of failed samples can be used to quantify the failure probability and reliability index. As shown, the number of failed samples increases with increasing the crack size. To better illustrate the results, Figures 5-14(a) to 5-14(c) show a 2-D view of assessment points and mean assessment curves at a crack size ranging between 2-3 m, 4-5 m, and 11-12 m. As shown in these figures, there are samples that lie outside the mean assessment curve in Zone I (i.e., brittle failure), Zone II (i.e., elastic-plastic fracture), and Zone III (i.e., plastic collapse). Accordingly, the failure mechanism changes as the crack propagates with a higher possibility of brittle fracture at a higher crack size.

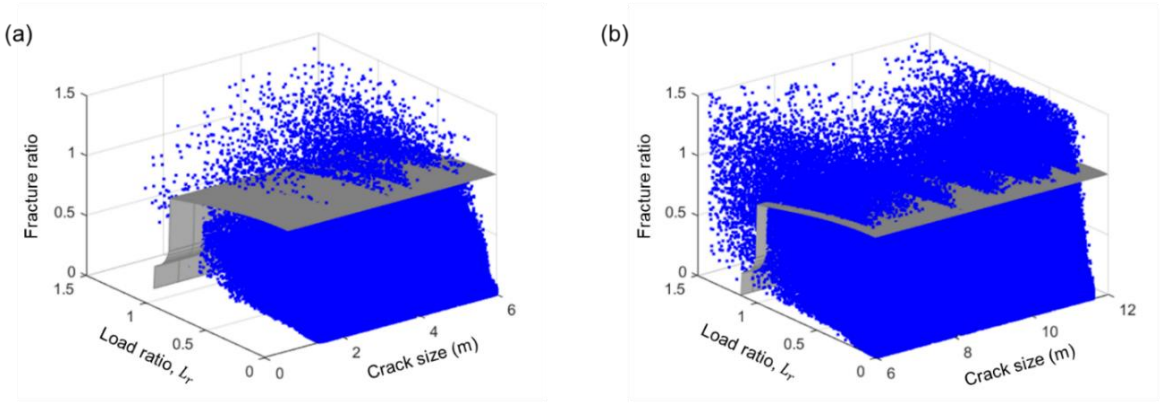

Figure 5-13. A 3-D view of the simulated assessment points and the mean assessment curve for crack sizes ranging between: (a) 0 to 6 m, and (b) 6 to 12 m.

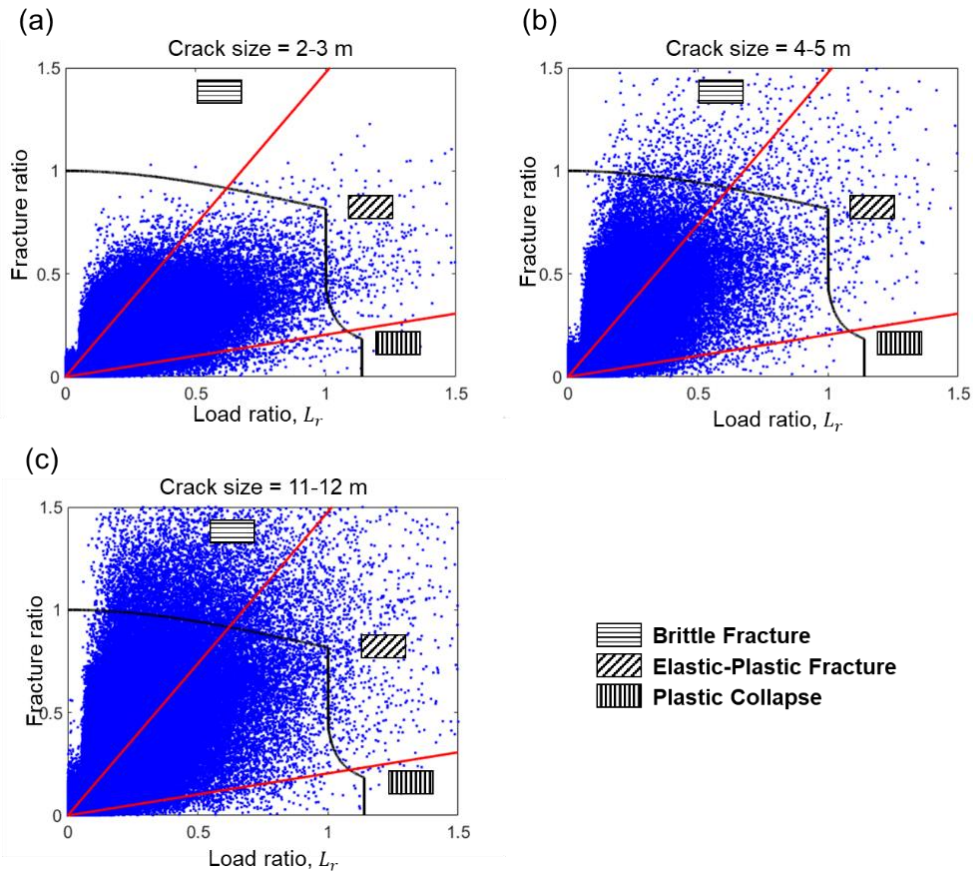

Figure 5-14. A 2-D view of the simulated assessment points and mean assessment curves at a crack size ranging between (a) 2 to 3 m, (b) 4 to 5 m, and (c) 11 to 12 m.

To further investigate the dominant failure mechanism with respect to the crack sizes, the number of failed samples in different zones was quantified and the ratio between the number of failed samples at each zone to the total number of failed samples was computed. Figure 5-15 shows this percentage for different mechanisms with respect to the crack sizes. As shown, for crack sizes lower than 4 m, the elastic-plastic fracture is the most probable failure mechanism. However, for longer crack sizes, the occurrence probability of brittle fracture increases and it becomes the dominant failure mode when the crack size is above 10 m. The failure probability and reliability index are calculated using Equations (5-17) and (5-18), respectively. Figure 5-16(a) shows the reliability index with

respect to the crack size obtained using the proposed approach. As shown, the reliability index ranges between 4.5 and 2.7 for the considered crack sizes. The reliability also drops significantly when the brittle fracture becomes the dominant failure mechanism (i.e., a > 10 m). The results show that to maintain a target reliability index of 3.5 (Bhattacharya et al., 2001), it is essential to limit the crack size below 4.75 m. Note that the total width of the section is 28.5 m.

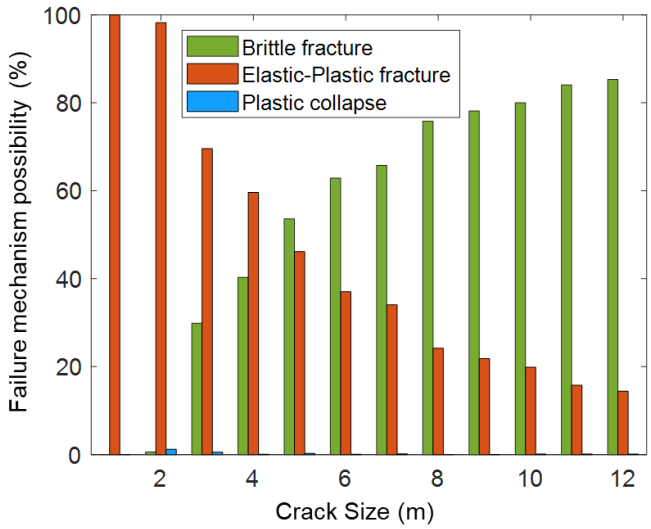

Figure 5-15. Percentage of different failure mechanisms in all failed samples with respect to crack size.

It was of interest to the authors to compare the results of the proposed approach to those resulting from traditional performance functions. To conduct such analysis, a performance function in terms of the SIF (i.e., $g = \Delta K - K_{IC}$) is defined and the MCS is used to compute the reliability index. K_{IC} represents the critical SIF of the material. In this performance function, the critical SIF is considered as the resistance limit while the applied SIF is considered as the load effect. A failure condition is reached if the calculated SIF is larger than the critical SIF. The SIF range is extracted directly from the developed FE model in ABAQUS environment while the critical SIF is computed from the C(T) specimen at the

critical CTOD using Equation (5-10). The resulting critical SIF value was found to be comparable to those reported in literature (Mahmoud & Riveros, 2014). MCS is performed to determine the probability of failure and the reliability index and the results are shown in Figure 5-16(b). As shown, the traditional approach may result in a highly conservative estimate of the reliability since it does not account for the elastic-plastic failure mechanism and does not properly predict the fracture resistance of the structure.

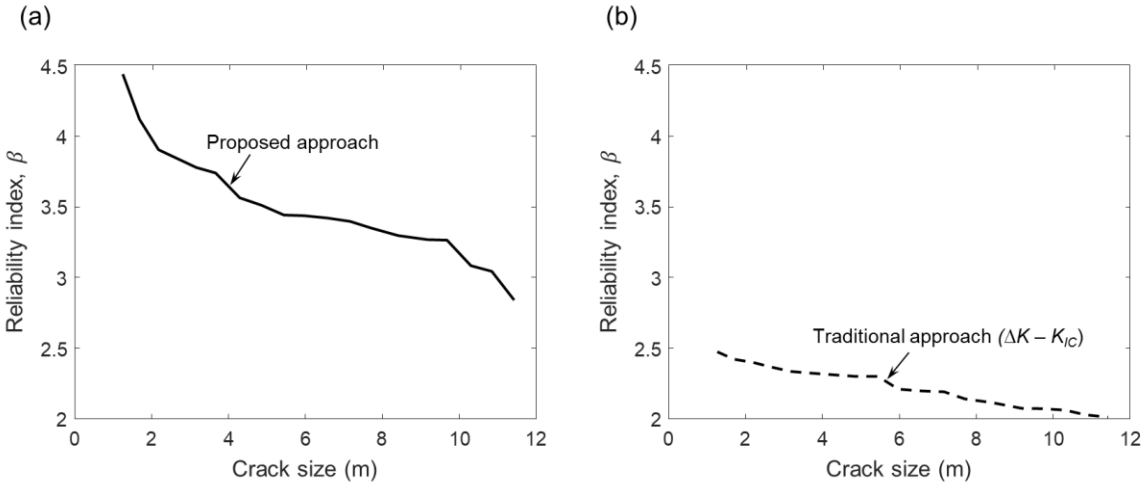

Figure 5-16. The reliability index of the investigated ship hull at various crack sizes calculated using: (a) the proposed framework and (b) the traditional performance function utilizing the SIF.

5.10. Conclusions

This chapter presented a probabilistic framework for quantifying the reliability of ship hull structures under propagating fatigue cracks. Climate data are used to estimate the realistic wave-induced loads acting on the hull structure. The failure assessment diagram is utilized to define the limit states considering various failure modes that may occur under hull cracking. The resistance of the hull to sudden fracture is evaluated by applying the Weibull stress criterion. The crack driving force, stress fields, and other necessary resistance and demand parameters were obtained from a 3-D FE model of the hull. MCS is used to conduct

the probabilistic analysis and quantify the reliability of the ship hulls under the applied loads and propagating crack. The following conclusions are drawn:

- The proposed approach provides a rational mechanism for quantifying the reliability of the cracked hulls while accounting for realistic loading conditions, occurrence probability of relevant failure modes, and the resistance of the hull girder to sudden fracture. Traditional performance functions defined in terms of the SIF (i.e., $\Delta K - K_{IC}$) were found to provide a highly conservative estimate of the reliability index compared to the proposed approach.
- Analysis of the investigated case study showed that the yielding condition at the crack tip changes as the crack propagates. At lower crack sizes, small-scale yielding conditions are expected to occur and LEFM can be used to model the crack propagation. For the investigated example, these conditions were applicable up to a crack size of approximately one meter. Large-scale plasticity conditions may occur beyond this limit.
- The fracture resistance of the ship hull was found to be significantly higher than that of standard compact tension specimens; this is especially true at small crack sizes. The fracture resistance was found to decrease as the crack size increases due to the constraint losses effect.
- Evaluation of the failed samples within the MCS process indicated that there is a probability of occurrence of all three possible failure modes: brittle failure, elastic-plastic fracture, and plastic collapse. However, the occurrence probability of each failure mechanism changes as the crack propagates with a higher possibility of brittle fracture at a larger crack size.

- The generated reliability profile can be used to make informed decisions regarding repair planning and optimization to minimize repair costs while maintaining reliability levels above acceptable thresholds.

CHAPTER VI

CONCLUSIONS

6.1. Overview

The main goal of this dissertation is to develop a probabilistic approach for assessing the performance of civil and marine structures using machine-learning-assisted MCS. In this approach, machine learning is used to generate a surrogate model of the system response and is next integrated into the MCS to quantify the failure probability and the reliability of the structure. Sensitivity analysis is conducted to identify the key contributing variables that significantly affect the system response. The developed approach was applied to investigate the behavior of eccentrically loaded connections made by combining fillet welds and high-strength pretensioned bolts. FE analysis is conducted to investigate the load sharing and transfer mechanisms within the combination connections. The FE models were also utilized in a sensitivity analysis aiming at identifying the key parameters that have a significant effect on the connection capacity. A thorough reliability analysis was conducted using FE analysis assisted by machine learning to quantify the reliability level of the investigated connections and establish the appropriate resistance factors necessary to maintain the reliability level above prescribed thresholds.

This dissertation also developed a probabilistic fatigue crack propagation approach that accounts for uncertainties associated with the loading conditions; specifically, those affected by climate change. The results showed that the effect of climate change on the crack growth rate depends on the navigation route. While several routes displayed a reduction in the crack growth activity within the prediction time frame, some routes showed a reduction in the expected fatigue service life. Furthermore, this dissertation quantified the influence of relevant input parameters, covering geometric and mechanical properties, on the crack propagation behavior and fatigue service life of welded stiffened panels. The geometric parameters include the main panel thickness and stiffener characteristics while the mechanical properties cover the crack propagation regression parameters, modulus of elasticity, and yield strength. The results showed that the variability in both geometric parameters and mechanical properties have a significant influence on the variability of the fatigue service life of the stiffened panels. Furthermore, it was found that neglecting uncertainties in geometric parameters when evaluating the fatigue reliability of these panels can lead to highly unconservative estimates.

Meanwhile, a novel probabilistic approach was proposed for quantifying the reliability of ship hulls under propagating fatigue cracks by utilizing the failure assessment diagram. The proposed approach considers various possible failure mechanisms ranging from brittle fracture to plastic collapse. In addition, the proposed approach properly quantifies the fracture resistance of the structure to represent the actual geometry and mechanical characteristics of the hull girder. MCS is performed to determine the probability of failure and the reliability index of the ship hull under encountered wave loads and propagating cracks. The results showed that the traditional approaches may result in a highly

conservative estimate of the reliability compared with the proposed approach since it does not account for the elastic-plastic failure mechanism, as well as the actual fracture resistance of the structure.

6.2. Investigating the Behavior and Reliability of Eccentrically Loaded Steel Connections Made with Bolts and Welds in Combination

This chapter provided an in-depth investigation into the behavior of eccentrically loaded steel connections combining fillet welds and high-strength pretensioned bolts. The capacity of the combination connections was calculated using the ICR method when connecting elements are considered as a part of a single load resisting system. A newly developed load-deformation model for the slip resistance introduced by the pretensioned bolts was utilized to improve the ability of the ICR method to predict the capacity. Three-dimensional FE models representing the investigated connections were developed and validated utilizing experimental results. The load sharing and transfer mechanisms within the combination connections were studied using the validated FE models. Finally, this chapter integrated FE analysis, ANN, and MCS to evaluate the reliability level of these connections. The following conclusions can be drawn:

- The ICR method can be used to predict the load-carrying capacity of eccentrically loaded combination connections. This requires considering the connecting elements to be participating in a single load resisting system and utilizing proper load-deformation characteristics of slip-resistant bolted connections. A simple summation of individual resistances provided by the bolts and welds may not achieve accurate estimates of the combination connection capacity.

- The proposed load-deformation models for slip-resistant bolted connections enhance the ability of the ICR method to predict the load-carrying capacity of eccentrically loaded slip-resistant bolted connections combined with fillet welds. These models can also be adopted in predicting the capacity of bolted-only slip resistance connections using the ICR method.
- For the investigated combination connections, the load-rotation behavior was found to depend on the weld-to-bolt strength ratio (Rn_w/Rn_b). The improvement in the overall capacity, compared to the individual capacities provided by the bolts and welds, was relative to the ratio between welds capacity and bolts capacity.
- The efficiency of individual connecting elements in resisting eccentric loads can be improved by combining bolts and welds in a single load-resisting mechanism. Given the location of the ICR in the combined system, connecting elements can carry more eccentric loading in the shared mechanism compared to their capacity if used separately.
- The reliability analysis conducted on the investigated connections shows that these connections, when designed using the ICR method, can achieve high reliability levels using a resistance factor of 0.75. A higher resistance factor can also be used for connections with Class A and B faying surfaces to provide an adequate reliability index under various live-to-dead load ratios.

6.3. Quantifying Fatigue Deterioration of Ship Structures under Changing Climate Conditions

This chapter presented a probabilistic framework for quantifying the effect of climate change on crack propagation characteristics in ships. The long-term variability in wind-

induced waves were projected using global climate models. West-east and south-north wind data were adopted from the CMIP5 archive. The change in the mean and 95th percentile wave heights due to climate variability were projected across the Atlantic Ocean. A probabilistic fatigue crack propagation approach was developed to properly consider the uncertainties associated with material properties and climate-related loading conditions. Eight different routes across the Atlantic Ocean were selected to quantify the effect of climate change on the fatigue crack propagation under future climate conditions. Finally, time-variant failure probability profiles based on historical and GCM-provided climate data in the North Atlantic were generated and compared. The following conclusions were drawn:

- The proposed framework is capable of quantifying the long-term effects of climate change on the VBM and the fatigue crack propagation in ship hulls.
- Analysis of the projected GCM data indicates that tropical regions of the Atlantic Ocean in both southern and northern hemispheres will experience small deviations in mean and extreme wave heights compared to historical records. However, subtropical regions in the southern hemisphere show a decreasing trend in the mean and 95th percentile wave heights. A decreasing trend in mean and extreme wave heights in subtropics and temperate in the northern hemisphere is also observed. In contrary, most of the adopted GCMs projected an increase in the mean and 95th percentile wave heights for regions covering 45^{o} S to 60^{o} S and 70^{o} N to 80^{o} N.
- The fatigue crack propagation results under the defined climate scenarios show that the effect of climate change highly depends on the navigation route. While some

routes displayed an expected increase in the fatigue service life, others showed a reduction that can reach 8%.

- Analysis of the impact of climate change on the failure probability of the investigated ship shows that the projected average failure probability associated with Routes 1 – 6 is lower than that resulting from the historical records. However, the failure probability for individual navigation routes can be lower or higher in comparison to the one associated with historical records. Accordingly, the expected navigation routes for a specific ship should be considered in the long-term life-cycle analysis aiming at estimating and/or reducing the fatigue failure probability of the ship.

6.4. Sensitivity and Probabilistic Assessment of Crack Propagation Behavior in Welded Stiffened Panels

This chapter presented a probabilistic analysis for the sensitivity and reliability assessment of the fatigue crack propagation in welded stiffened panels. A 3-D FE analysis, an artificial neural network, and an Elastic-Plastic advanced crack growth model are integrated to predict crack propagation under cyclic loading. The proposed approach is validated using experimental test data from literature. A sensitivity analysis is conducted to identify the key variables that have a significant effect on the crack propagation behavior in stiffened panels. The variability in the mechanical properties of the material and several geometric parameters are considered. MCS is used to conduct the probabilistic analysis and quantify the reliability of the stiffened panels while accounting for the variability in the mechanical and geometric parameters. The following conclusions were drawn:

- The results of the sensitivity analysis showed that both geometric parameters and mechanical properties have a significant influence on the fatigue service life of the stiffened panels. Thus, more attention should be paid to the dimensions during the design and manufacturing process.
- Relative to the mechanical properties of the material, the variability in the fatigue service life is strongly influenced by the variability in Paris's law material regression parameters (i.e., c_o and m_o). However, the modulus of elasticity and yield strength of the material have a low effect.
- Relative to the geometric parameters of the stiffened panels, the variability in the fatigue service life is strongly influenced by the variability in the main panel thickness. The second dominant quantity is the web characteristics (i.e., stiffener height and thickness). The third influential quantity is spacing between stiffeners. On the other hand, the variability in the properties of the flange (i.e., flange width and thickness) seem to have a minimal contribution to the variability in the fatigue service life.
- The reliability analysis conducted on the investigated stiffened panels shows that using traditional reliability assessment approaches that do not properly consider the variability in geometric properties can lead to a considerable non-conservative estimate of the reliability index.

6.5. Comprehensive Quantification of the Reliability of Ship Hulls Under Propagating Fatigue Cracks

This chapter presented a probabilistic framework for quantifying the reliability of ship hull structures under propagating fatigue cracks. Climate data are used to estimate the realistic

wave-induced loads acting on the hull structure. The failure assessment diagram is utilized to define the limit states considering various failure modes that may occur under hull cracking. The resistance of the hull to sudden fracture is evaluated by applying the Weibull stress criterion. The crack driving force, stress fields, and other necessary resistance and demand parameters were obtained from a 3-D FE model of the hull. MCS is used to conduct the probabilistic analysis and quantify the reliability of the ship hulls under the applied loads and propagating crack. The following conclusions are drawn:

- The proposed approach provides a rational mechanism for quantifying the reliability of the cracked hulls while accounting for realistic loading conditions, the occurrence probability of relevant failure modes, and the resistance of the hull girder to sudden fracture. Traditional performance functions defined in terms of the SIF (i.e., $\Delta K - K_{IC}$) were found to provide a highly conservative estimate of the reliability index compared to the proposed approach.
- Analysis of the investigated case study showed that the yielding condition at the crack tip changes as the crack propagates. At lower crack sizes, small-scale yielding conditions are expected to occur and LEFM can be used to model the crack propagation. For the investigated example, these conditions were applicable up to a crack size of approximately one meter. Large-scale plasticity conditions may occur beyond this limit.
- The fracture resistance of the ship hull was found to be significantly higher than that of standard compact tension specimens; this is especially true at small crack sizes. The fracture resistance was found to decrease as the crack size increased due to the constraint losses effect.

- Evaluation of the failed samples within the MCS process indicated that there is a probability of occurrence of all three possible failure modes: brittle failure, elastic-plastic fracture, and plastic collapse. However, the occurrence probability of each failure mechanism changes as the crack propagates with a higher possibility of brittle fracture at a larger crack size.
- The generated reliability profile can be used to make informed decisions regarding repair planning and optimization to minimize repair costs while maintaining the reliability levels above acceptable thresholds.

6.6. Future Research

- The presented work focused on quantifying the reliability of ships under propagating fatigue cracks to ensure safety and serviceability during their service life. Although fatigue is a major aspect affecting the safety of the ships, other failure modes such as ultimate failure and progressive collapse should be studied.
- The presented work proposed a simulation-based framework for predicting the fatigue service life of ships under wave loading in light of climate change. Ships are also vulnerable to corrosion attacks due to the aggressive environment, and this lead to amplifying the crack growth rate under wave loading due to the interaction of the applied cyclic loads and the influence of the corrosive environment. Accordingly, the combined effect of both corrosion and fatigue should be considered in future work.
- The proposed framework for quantifying the fatigue service life of ships can be used for optimal ship routing, with the goals of extending the service life and minimizing the cost of maintenance and repair.

- Future research is needed to extend the conducted research by considering other materials such as aluminum.

REFERENCES

Aarnes, O. J., Reistad, M., Breivik, Ø., Bitner-Gregersen, E., Ingolf Eide, L., Gramstad, O., Magnusson, A. K., Natvig, B., & Vanem, E. (2017). Projected changes in significant wave height toward the end of the 21st century: Northeast A tlantic. *Journal of Geophysical Research: Oceans*, *122*(4), 3394-3403.

Abbasianjahromi, H., & Shojaeikhah, S. (2021). Structural reliability assessment of steel four-bolt unstiffened extended end-plate connections using Monte Carlo simulation and artificial neural networks. *Iranian Journal of Science and Technology, Transactions of Civil Engineering*, *45*(1), 111-123.

ABS. (2017). *Springing assessment for container carriers and ore carriers*. Houston, TX, USA: American Bureau of Shipping.

ABS. (2020). *Guide for fatigue assessment of offshore structures*. Houston, TX, USA: American Bureau of Shipping.

Agarwal, A., Venugopal, V., & Harrison, G. P. (2013). The assessment of extreme wave analysis methods applied to potential marine energy sites using numerical model data. *Renewable and Sustainable Energy Reviews*, *27*, 244-257.

AISC. (2006). *Manual of steel construction, 13th Edition*. Chicago, IL, USA: American Institute of Steel Construction.

AISC. (2016). *Specification for structural steel buildings (ANSI/AISC 360–16)*. Chicago, IL, USA: American Institute of Steel Construction.

AISC. (2017). *Manual of steel construction, 15th Edition*. Chicago, IL, USA: American Institute of Steel Construction.

Akpan, U. O., Koko, T. S., Ayyub, B., & Dunbar, T. E. (2002). Risk assessment of aging ship hull structures in the presence of corrosion and fatigue. *Marine Structures, 15*(3), 211-231.

Albrecht, P., & Yazdani, N. (1986). *Risk analysis of extending bridge service life*. MD, USA: Department. of Civil Engineering, University of Maryland.

Aly, Z., Casagranda, A., Pastore, G., & Brown, N. R. (2019). Variance-based sensitivity analysis applied to the hydrogen migration and redistribution model in Bison. Part II: Uncertainty quantification and optimization. *Journal of Nuclear Materials, 523*, 478-489.

Anderson, T. L. (2017). *Fracture mechanics: fundamentals and applications*. Boca Raton, FL, USA: CRC Press.

Arwade, S. R., Moradi, M., & Louhghalam, A. (2010). Variance decomposition and global sensitivity for structural systems. *Engineering Structures, 32*(1), 1-10.

ASCE/SEI. (2016). *Minimum design loads for buildings and other structures*. Reston, VA, USA: ASCE/Structural Engineering Institute 7-16.

ASTM A131. (2019). Standard specification for structural steel for ship. West Conshohocken, PA, USA: ASTM International, American Association State.

ASTM A572/A572M. (2015). Standard specification for high-strength low-alloy columbium-vanadium structural steel. West Conshohocken, PA, USA: ASTM International, American Association State.

ASTM-E1290-08. (2002). *Standard test method for crack-tip opening displacement (CTOD) fracture toughness measurement*. West Conshohocken, PA, USA: American Society for Testing and Materials.

Avcar, M., & Saplioglu, K. (2015). An artificial neural network application for estimation of natural frequencies of beams. *International Journal of Advanced Computer Science and Applications, 6*(6), 94-102.

Barsom, J. M. & Rolfe, S. T. (1987). *Fracture and Fatigue Control in Structures 2nd ed*. New Jersey, USA: Englewood Cliffs.

Bennett, S., Hudson, D., & Temarel, P. (2013). The influence of forward speed on ship motions in abnormal waves: Experimental measurements and numerical predictions. *Journal of Fluids and Structures, 39*, 154-172.

Beremin, F. M., Pineau, A., Mudry, F., Devaux, J.-C., D'Escatha, Y., & Ledermann, P. (1983). A local criterion for cleavage fracture of a nuclear pressure vessel steel. *Metallurgical Transactions A, 14*(11), 2277-2287.

Bernard, E. N., & Robinson, A. R. (2009). *Tsunamis* (Vol. 15). MA, USA: Harvard University Press.

Bhattacharya, B., Basu, R., & Ma, K.-t. (2001). Developing target reliability for novel structures: the case of the Mobile Offshore Base. *Marine Structures, 14*(1-2), 37-58.

Bitner-Gregersen, E. M., Vanem, E., Gramstad, O., Hørte, T., Aarnes, O. J., Reistad, M., Breivik, Ø., Magnusson, A. K., & Natvig, B. (2018). Climate change and safe design of ship structures. *Ocean Engineering, 149*, 226-237.

Boone, A. A., Xue, Y., De Sales, F., Comer, R. E., Hagos, S., Mahanama, S., Schiro, K., Song, G., Wang, G., & Li, S. (2016). The regional impact of Land-Use Land-cover

Change (LULCC) over West Africa from an ensemble of global climate models under the auspices of the WAMME2 project. *Climate Dynamics*, *47*(11), 3547-3573.

Božić, Ž., Mlikota, M., & Schmauder, S. (2011). Application of the ΔK, ΔJ and ΔCTOD parameters in fatigue crack growth modelling. *Tehnički Vjesnik, 18*(3), 459-466.

Božić, Ž., Schmauder, S., Mlikota, M., & Hummel, M. (2014). Multiscale fatigue crack growth modelling for welded stiffened panels. *Fatigue and Fracture of Engineering Materials and Structures*, *37*(9), 1043-1054.

Bretschneider, C. L. (1959). *Wave variability and wave spectra for wind-generated gravity waves*. Washington D.C, USA: US Army Corps of Engineers, Beach Erosion Board.

Bricheno, L. M., & Wolf, J. (2018). Future wave conditions of Europe, in response to high-end climate change scenarios. *Journal of Geophysical Research: Oceans*, *123*(12), 8762-8791.

Brocks, W., & Scheider, I. (2001). Numerical aspects of the path-dependence of the J-integral in incremental plasticity. *GKSS Forschungszentrum, Geesthacht*, *1*, 1-33.

Brown, J. M., Wolf, J., & Souza, A. J. (2012). Past to future extreme events in Liverpool Bay: model projections from 1960–2100. *Climatic change*, *111*(2), 365-391.

BSI. (2015). *Guide to methods for assessing the acceptability of flaws in metallic structures*. London, United Kingdom: British Standards Institution.

Butler, L. J., Pal, S., & Kulak, G. L. (1972). Eccentrically loaded welded connections. *Journal of the Structural Division*, *98*(5), 989-1005.

Caiazzo, F., Alfieri, V., Corrado, G., & Argenio, P. (2017). Laser powder-bed fusion of Inconel 718 to manufacture turbine blades. *The International Journal of Advanced Manufacturing Technology*, *93*(9), 4023-4031.

Castillo, E., Fernández-Canteli, A., Hadi, A. S., & López-Aenlle, M. (2007). A fatigue model with local sensitivity analysis. *Fatigue & Fracture of Engineering Materials & Structures*, *30*(2), 149-168.

Chen, J.-p., & Zhu, D.-x. (2010). Numerical simulations of wave-induced ship motions in time domain by a Rankine panel method. *Journal of Hydrodynamics*, *22*(3), 373-380.

Chung, H.-Y. (2004). *Fatigue reliability and optimal inspection strategies for steel bridges*. Doctoral dissertation, The University of Texas at Austin, Austin, TX, USA.

Cornell, C. (1969). A probability-based structural code. *Journal of the American Concrete Institute*, *66*(12), 974-985.

Crawford, S. F., & Kulak, G. L. (1971). Eccentrically loaded bolted connections. *Journal of the Structural Division*, *97*(3), 765-783.

CSA. (2018). *General requirements for rolled or welded structural quality steel*. Ontario, Canada: Canadian Standards Association.

Deb, K., Pratap, A., Agarwal, S., & Meyarivan, T. A. M. T. (2002). A fast and elitist multiobjective genetic algorithm: NSGA-II. *IEEE Transactions on Evolutionary Computation*, 6(2), 182-197.

Decò, A. (2013). *Risk-based approach for life-cycle assessment and management of bridges and ship structures*. Doctoral dissertation, Lehigh University, Bethlehem, PA, USA.

Decò, A., Frangopol, D. M., & Zhu, B. (2012). Reliability and redundancy assessment of ships under different operational conditions. *Engineering Structures*, *42*, 457-471.

Dehghani, M., Tremblay, R., & Leclerc, M. (2017). Fatigue failure of 350WT steel under large-strain seismic loading at room and subfreezing temperatures. *Construction and Building Materials*, *145*, 602-618.

Deng, D., Liang, W., & Murakawa, H. (2007). Determination of welding deformation in fillet-welded joint by means of numerical simulation and comparison with experimental measurements. *Journal of Materials Processing Technology*, *183*(2-3), 219-225.

Der Kiureghian, A., Lin, H. Z., & Hwang, S. J. (1987). Second-order reliability approximations. *Journal of Engineering Mechanics*, *113*(8), 1208-1225.

Dexter, R. J., & Pilarski, P. J. (2002). Crack propagation in welded stiffened panels. *Journal of Constructional Steel Research*, *58*(5-8), 1081-1102.

Dexter, R. J., Mahmoud, H. N., & Pilarski, P. (2005). Propagation of long cracks in stiffened box-sections under bending and stiffened single panels under axial tension. *International Journal of Steel Structures*, *5*(3), 181-188.

Dexter, R. J., Pilarski, P. J., & Mahmoud, H. N. (2003). Analysis of crack propagation in welded stiffened panels. *International Journal of Fatigue*, *25*(11), 1169-1174.

Ding, Z., Wang, X., Gao, Z., & Bao, S. (2017). An experimental investigation and prediction of fatigue crack growth under overload/underload in Q345R steel. *International Journal of Fatigue*, *98*, 155-166.

Dinovitzer, A. (2003). *Life expectancy assessment of ship structures*. Washington D.C, USA: Ship Structure Committee.

DNV. (1984). *Fatigue Strength Analysis for Mobile Offshore Units: Classification Notes No. 30.2*, Høvik, Norway: Det Norske Veritas.

DNV. (2001). *Fatigue assessment of ship structures*, Høvik, Norway: Det Norske Veritas.

DNV. (2015). *Fatigue assessment of ship structures*. Høvik, Norway: Det Norske Veritas.

Dong, Y., Teixeira, A., & Guedes Soares, C. (2018). Time-variant fatigue reliability assessment of welded joints based on the PHI2 and response surface methods. *Reliability Engineering and System Safety*, *177*, 120-130.

Doré, M. J., & Maddox, S. J. (2013). Accelerated fatigue crack growth in 6082 T651 aluminium alloy subjected to periodic underloads. *Procedia Engineering*, *66*, 313-322.

Doshi, K., & Vhanmane, S. (2013). Probabilistic fracture mechanics based fatigue evaluation of ship structural details. *Ocean Engineering*, *61*, 26-38.

Dresia, K., Waxenegger-Wilfing, G., Riccius, J., Deeken, J. C., & Oschwald, M. (2019). Numerically efficient fatigue life prediction of rocket combustion chambers using artificial neural networks. *The 8th European for Aeronautics and Space Sciences Conference*, Madrid, Spain.

Drummen, I., Wu, M., & Moan, T. (2009). Experimental and numerical study of containership responses in severe head seas. *Marine Structures*, *22*(2), 172-193.

ECMWF. (2022). *The fifth-generation climate reanalysis dataset (ERA5) dataset*. Reading, England: European Centre for Medium-Range Weather Forecasts https://www.ecmwf.int/en/forecasts/datasets/reanalysis-datasets/era5

Espinosa, A. A., Fellows, N. A., Durodola, J. F., & Fellows, L. J. (2017). Determination of crack growth for 6082-T6 aluminium subjected to periodic single and block overloads and underloads using a two dimensional finite element model. *International Journal of Fatigue*, *105*, 244-261.

Eurocode 3. (2010). *Design of steel structures part 1–9, fatigue strength*. Brussels, Belgium: CEN-European Committee for Standardisation.

Faltinsen, O. (1993). *Sea loads on ships and offshore structures* (Vol. 1). Trondheim, Norway: Norwegian Institute of Technology, Cambridge University Press.

Faulkner, D. (1975). A review of effective plating for use in the analysis of stiffened plating in bending and compression. *Journal of Ship Research, 19*(01), 1-17.

Feng, G., Garbatov, Y., & Guedes Soares, C. (2012). Fatigue reliability of a stiffened panel subjected to correlated crack growth. *Structural Safety*, *36*, 39-46.

Fisher, J. (1964). *On the behavior of fasteners and plates with holes (No. 288-18).* Bethlehem, PA, USA: Fritz Engineering Laboratory, Lehigh University, Department of Civil Engineering.

François, D., Pineau, A., & Zaoui, A. (1999). *Mechanical behaviour of materials*. New Jersey, USA: Springer.

Galambos, T. V., & Ravindra, M. (1981). Load and resistance factor design. *Engineering Journal, AISC, 18*(3), 78-84.

Gannon, L. (2011). Effect of welding residual stress and distortion on ship hull structural performance. Halifax, Nova Scotia: Doctoral Dissertation, Dalhousie University.

Gaspar, B., Teixeira, A. P., & Guedes Soares, C. (2016). Sensitivity analysis of the IACS-CSR buckling strength requirements for stiffened panels. London, UK: Taylor and Francis Group.

Gope, P. C. (2016). Probabilistic model of fatigue crack propagation and estimation of probability-confidence bounded a–N curves. *International Journal for Computational Methods in Engineering Science and Mechanics*, *17*(4), 298-314.

Grabemann, I., & Weisse, R. (2008). Climate change impact on extreme wave conditions in the North Sea: an ensemble study. *Ocean Dynamics*, *58*(3-4), 199-212.

Grondin, G. Y., Jin, M., & Georg, J. (2007). *Structural engineering*, Report No. 270. Alberta, Canada: The University of Alberta, Department of Civil Engineering.

Guedes Soares, C., & Garbatov, Y. (1996). Fatigue reliability of the ship hull girder accounting for inspection and repair. *Reliability Engineering and System Safety*, *51*(3), 341-351.

Guedes Soares, C., & Teixeira, A. (2000). Structural reliability of two bulk carrier designs. *Marine Structures*, *13*(2), 107-128.

Hagan, M. T., & Menhaj, M. B. (1994). Training feedforward networks with the Marquardt algorithm. *IEEE Transactions on Neural Networks*, *5*(6), 989-993.

Hambli, R. (2010). Application of neural networks and finite element computation for multiscale simulation of bone remodeling. *Journal of Biomechanical Engineering*, *132*(11).

Hansen, P. F., & Hansen, A. M. (1994). *Reliability analysis of a midship section*. Denmark: Danmarks Tekniske Universitet, Instituttet for Skibs-og Havteknik.

Hasselmann, K., Barnett, T. P., Bouws, E., Carlson, H., Cartwright, D. E., Enke, K., Ewing, J., Gienapp, A., Hasselmann, D., & Kruseman, P. (1973). Measurements of wind-wave growth and swell decay during the Joint North Sea Wave Project

(JONSWAP). *Ergaenzungsheft zur Deutschen Hydrographischen Zeitschrift*, *8*(12), 1–95.

Hawkins, E., & Sutton, R. (2009). The potential to narrow uncertainty in regional climate predictions. *Bulletin of the American meteorological Society*, *90*(8), 1095-1108.

Hersbach, H., Bell, B., Berrisford, P., Biavati, G., Horányi, A., Muñoz Sabater, J., Nicolas, J., Peubey, C., Radu, R., & Rozum, I. (2019). ERA5 monthly averaged data on single levels from 1979 to present. *Copernicus Climate Change Service (C3S) Climate Data Store (CDS)*, *10*, 252-266.

Hess, P. E., Bruchman, D., Assakkaf, I. A., & Ayyub, B. M. (2002). Uncertainties in material and geometric strength and load variables. *Naval Engineers Journal*, *114*(2), 139-166.

Hibbitt, D., Karlsson, B., & Sorensen, P. (2013). *Abaqus/CAE user's guide, ABAQUS 6.11*, RI, USA: Dassault Systèmes Simulia Corp.

Hodapp, D. P., Collette, M. D., & Troesch, A. W. (2015). Stochastic nonlinear fatigue crack growth predictions for simple specimens subject to representative ship structural loading sequences. *International Journal of Fatigue*, *70*, 38-50.

Holtz, N. M., & Kulak, G. L. (1970). *High-strength bolts and welds in load-sharing systems*, Report No. 8. Canada: Nova Scotia Technical College, Department of Civil and Environmental Engineering.

Horn, A., & Sherry, A. (2012). An engineering assessment methodology for non-sharp defects in steel structures–Part I: Procedure development. *International Journal of Pressure Vessels and Piping*, *89*, 137-150.

Hørte, T., Wang, G., & White, N. (2007). Calibration of the hull girder ultimate capacity criterion for double hull tankers. In *Proceedings from the 10th international Symp on Practical Designs of Ships and Other Floating Structures*, Houston, TX, USA.

Huang, W., Garbatov, Y., & Guedes Soares, C. (2013). Fatigue reliability assessment of a complex welded structure subjected to multiple cracks. *Engineering Structures*, *56*, 868-879.

Huang, X., Torgeir, M., & Cui, W. (2008). An engineering model of fatigue crack growth under variable amplitude loading. *International Journal of Fatigue*, *30*(1), 2-10.

Hughes, O. F. (1983). *Ship structural design: a rationally-based, computer-aided, optimization approach*. CA, USA: Wiley-Interscience.

Hussein, A., & Guedes Soares, C. (2009). Reliability and residual strength of double hull tankers designed according to the new IACS common structural rules. *Ocean Engineering*, *36*(17-18), 1446-1459.

IACS. (2022). *Common structural rules for bulk carriers and oil tankers*. London, United Kingdom: The International Association of Classification Societies.

Irwin, G. R. (1957). Analysis of stresses and strains near the end of a crack traversing plate. *Journal of Applied Mechanics, 24*, 361-364.

Jaimes, F., Farbiarz, J., Alvarez, D., & Martínez, C. (2005). Comparison between logistic regression and neural networks to predict death in patients with suspected sepsis in the emergency room. *Critical Care, 9*(2), 1-7.

Janon, A., Klein, T., Lagnoux, A., Nodet, M., & Prieur, C. (2014). Asymptotic normality and efficiency of two Sobol index estimators. *ESAIM: Probability and Statistics, 18*, 342-364.

Janssen, P. A. (2015). *Notes on the maximum wave height distribution*. Reading, UK: European Centre for Medium-Range Weather Forecasts.

Jarosch, K., & Bowman, M. (1986). Tension butt joints with bolts and welds in combination. *Engineering Journal, AISC, 23*(1), 25-35.

Kayamori, Y., & Kawabata, T. (2017). Evaluation of rotational deformation in compact specimens for CTOD fracture toughness testing. *Procedia Structural Integrity, 5*, 286-293.

Kent, E., Hall, A., & Leader, V. T. T. (2010). The Voluntary Observing Ship (VOS) Scheme. In *Proceedings from the 2010 AGU Ocean Sciences Meeting.* Washington DC, USA: American Geophysical Union, 551-561.

Khan, N., Gaurav, D., & Kandl, T. (2013). Performance evaluation of Levenberg-Marquardt technique in error reduction for diabetes condition classification. *Procedia Computer Science, 18*, 2629-2637.

Khandel, O., & Soliman, M. (2019). Integrated framework for quantifying the effect of climate change on the risk of bridge failure due to floods and flood-induced scour. *Journal of Bridge Engineering, 24*(9), 04019090.

Khandel, O., & Soliman, M. (2021). Integrated Framework for Assessment of Time-Variant Flood Fragility of Bridges Using Deep Learning Neural Networks. *Journal of Infrastructure Systems, 27*(1), 04020045.

Khandel, O., Tamimi, M. F., Soliman, M., Russell, B. W., & Waite, C. D. (2022). Reliability assessment of connections with slip-critical bolts and fillet welds in combination. *Journal of Constructional Steel Research, 188*, 107036.

Kim, D.-K., & Lee, C.-H. (2020). Experimental and analytical study of combined bolted-welded lap joints including high-strength steel. *Journal of Constructional Steel Research, 168*, 105995.

Kim, S., Frangopol, D.M. & Soliman, M., (2013). Generalized probabilistic framework for optimum inspection and maintenance planning, *Journal of Structural Engineering*, 139(3), 435-447.

Kim, Y. K., Oh, B. T., & Kim, J. H. (2020). Effects of crack tip constraint on the fracture toughness assessment of 9% Ni steel for cryogenic application in liquefied natural gas storage tanks. *Materials*, *13*(22), 5250.

Konakli, K., & Sudret, B. (2016). Global sensitivity analysis using low-rank tensor approximations. *Reliability Engineering and System Safety*, *156*, 64-83.

Konakli, K., & Sudret, B. (2016). Polynomial meta-models with canonical low-rank approximations: Numerical insights and comparison to sparse polynomial chaos expansions. *Journal of Computational Physics*, *321*, 1144-1169.

Kondo, J., & Ostapenko, A. (1964). *Tests on longitudinally stiffened plate panels with fixed ends*. Bethlehem, PA, USA: Fritz Engineering Laboratory, Lehigh University.

Kulak, G. L. (1975). Eccentrically loaded slip-resistant connections. *Journal of the Structural Division*, *12*(2), 52-55.

Kumar, V. S., & Naseef, T. M. (2015). Performance of ERA-Interim Wave Data in the Nearshore Waters around India. *Journal of Atmospheric and Oceanic Technology*, *32*(6), 1257.

Kwan, Y. K., Gomez, I. R., Grondin, G. Y., & Kanvinde, A. M. (2010). Strength of welded joints under combined shear and out-of-plane bending. *Canadian Journal of Civil Engineering*, *37(2)*, 250-261.

Lancaster, J. F. (1999). *Metallurgy of welding, 6th edition*. Cambridge, England: Woodhead Publishing Limited.

Leheta, H. W., & Mansour, A. E. (1997). Reliability-based method for optimal structural design of stiffened panels. *Marine Structures*, *10*(5), 323-352.

Leitner, M., Barsoum, Z., & Schäfers, F. (2016). Crack propagation analysis and rehabilitation by HFMI of pre-fatigued welded structures. *Welding in the World*, *60*(3), 581-592.

Leon, R.T., Hoffman, J. & Staeger, T. (1996). *Design of partially restrained composite connections*. Chicago, IL, USA: Design Guide 8, American Institute of Steel Construction.

Lesik, D. F., & Kennedy, D. L. (1990). Ultimate strength of fillet welded connections loaded in-plane. *Canadian Journal of Civil Engineering*, *17*(1), 55-67.

Li, C., Grondin, G. Y., & Driver, R. G. (2007). Reliability analysis of concentrically loaded fillet welds, Report No. 271. Alberta, Canada: University of Alberta, Department of Civil and Environmental Engineering.

Lin, Y., & Yang, J. (1985). A stochastic theory of fatigue crack propagation. *AIAA journal, 23*(1), 117-124.

Lindstad, H., & Eskeland, G. S. (2015). Low carbon maritime transport: How speed, size and slenderness amounts to substantial capital energy substitution. *Transportation Research Part D: Transport and Environment, 41*, 244-256.

Lu, Y.-c., Yang, F.-p., & Chen, T. (2019). Effect of single overload on fatigue crack growth in QSTE340TM steel and retardation model modification. *Engineering Fracture Mechanics, 212*, 81-94.

Lue, D.-M., Liao, C.-Y., Chang, C.-C., & Hsu, W.-T. (2017). Improved analysis of bolted shear connection under eccentric loads. *Journal of Marine Science and Technology, 25*(4), 22-35.

Ma, X., He, X., & Tu, Z. C. (2021). Prediction of fatigue–crack growth with neural network-based increment learning scheme. *Engineering Fracture Mechanics, 241*, 107402.

Mahmoud, H. N., & Dexter, R. J. (2005). Propagation rate of large cracks in stiffened panels under tension loading. *Marine Structures, 18*(3), 265-288.

Mahmoud, H., & Riveros, G. (2014). Fatigue reliability of a single stiffened ship hull panel. *Engineering Structures, 66*, 89-99.

Maljaars, J., & Vrouwenvelder, A. (2014). Probabilistic fatigue life updating accounting for inspections of multiple critical locations. *International Journal of Fatigue, 68*, 24-37.

Manuel, T. J., & Kulak, G. L. (2000). Strength of joints that combine bolts and welds. *Journal of Structural Engineering, 126*(3), 279-287.

Mao, W., Ringsberg, J. W., Rychlik, I., & Li, Z. (2012). Theoretical development and validation of a fatigue model for ship routing. *Ships and Offshore Structures, 7*(4), 399-415.

Marelli, S., & Sudret, B. (2014). UQLab: A framework for uncertainty quantification in Matlab. In *Vulnerability, Uncertainty, and Risk: Quantification, Mitigation, and Management*, Liverpool, United Kingdom.

Marques, B., Borges, M., Antunes, F., Vasco-Olmo, J., Díaz, F., & James, M. (2021). Limitations of small-scale yielding for fatigue crack growth. *Engineering Fracture Mechanics, 252*, 107806.

MathWorks. (2020). *MATLAB: the language of technical computing: computation, visualization, programming*. Natick, MA, USA: MathWorks.

McEvily, A. (1973). Phenomenological and microstructural aspects of fatigue. *The Microstructure and Design of Alloys, 1,* 204-225.

McPherson, R. (2016). *Impacts of Climate Change on Flows in the Red River Basin,* Report No. G13AC00386. Norman, OK, USA: South Central Climate Science Center.

Mehrzadi, M., & Taheri, F. (2013). A material sensitive modified wheeler model for predicting the retardation in fatigue response of AM60B due to an overload. *International Journal of Fatigue, 55,* 220-229.

Mehta, S., Rastegari, M., Shapiro, L., & Hajishirzi, H. (2019). Espnetv2: A light-weight, power-efficient, and general-purpose convolutional neural network. In *Proceedings of the IEEE/CVF Conference on Computer Vision and Pattern Recognition*, Long Beach, CA, USA.

Meinshausen, M., Smith, S. J., Calvin, K., Daniel, J. S., Kainuma, M. L., Lamarque, J.-F., Matsumoto, K., Montzka, S. A., Raper, S. C., & Riahi, K. (2011). The RCP greenhouse gas concentrations and their extensions from 1765 to 2300. *Climatic change, 109*(1), 213-241.

Melchers, R. E., & Beck, A. T. (2018). *Structural reliability analysis and prediction*. Newcastle, Australia: John Wiley & Sons.

Michaelson, R. W. (2000). *User's guide for SPECTRA: Version 8.3 (No. NSWCCD-65-TR-2000/07)*. MD, USA: Naval Surface Warfare Center.

Minami, F., Brückner-Foit, A., Munz, D., & Trolldenier, B. (1992). Estimation procedure for the Weibull parameters used in the local approach. *International Journal of Fracture, 54*(3), 197-210.

Moan, T., & Ayala-Uraga, E. (2008). Reliability-based assessment of deteriorating ship structures operating in multiple sea loading climates. *Reliability Engineering and System Safety, 93*(3), 433-446.

Murthy, A. R. C., Palani, G. S., & Iyer, N. R. (2007). Remaining life prediction of cracked stiffened panels under constant and variable amplitude loading. *International journal of fatigue, 29*(6), 1125-1139.

Newman, J. C., Phillips, E. P., & Swain, M. (1999). Fatigue-life prediction methodology using small-crack theory. *International Journal of Fatigue, 21(2),* 109-119.

Nicholls, R. J., Dawson, R. J., & Day, S. A. (2015). *Broad Scale Coastal Simulation*. Dordrecht, Netherlands: Springer.

Nussbaumer, A. C. (1994). *Propagation of long fatigue cracks in multi-cellular box beams*. Doctoral dissertation, Lehigh University, Bethlehem, PA, USA.

Nussbaumer, A. C., Fisher, J. W., & Dexter, R. J. (1999). Behavior of long fatigue cracks in cellular box beam. *Journal of Structural Engineering*, *125*(11), 1232-1238.

Ochi, M. (2003). *Hurricane generated seas*. Gainesville, FL, USA: Elsevier

Ohata, M., & Minami, F. (2012). Equivalent CTOD ratio β for engineering assessment of CTOD correction for constraint loss. *Journal of Pressure Vessel Technology*, *134*(5).

Opgenoord, M. M., Allaire, D. L., & Willcox, K. E. (2016). Variance-based sensitivity analysis to support simulation-based design under uncertainty. *Journal of Mechanical Design*, *138*(11), 111410.

Paris, P., & Erdogan, F. (1963). A critical analysis of crack propagation laws. *Journal of Basic Engineering*, *85*(1), 528-533.

Pierson Jr, W. J., & Moskowitz, L. (1964). A proposed spectral form for fully developed wind seas based on the similarity theory of SA Kitaigorodskii. *Journal of geophysical research*, *69*(24), 5181-5190.

Podgórski, K., Rychlik, I., & Machado, U. E. (2000). Exact distributions for apparent waves in irregular seas. *Ocean Engineering*, *27*(9), 979-1016.

Poe Jr, C. C. (1969). The effect of riveted and uniformly spaced stringers on the stress intensity factor of a cracked sheet. *Fatigue and Fracture of Aircraft Structure and Materials Conference*, Miami Beach, FL, USA.

Poe Jr, C. C. (1971). Fatigue crack propagation in stiffened panels. In *Damage tolerance in aircraft structures* (pp. 79-97). PA, USA: American Society for Testing and Materials (ASTM).

Prakash, S. K. (2009). *Modeling the constraint effects on fracture toughness of materials.* Akron, OH, USA: Doctoral Dissertation, University of Akron.

Qian, G., & Mahdi, A. (2020). Sensitivity analysis methods in the biomedical sciences. *Mathematical biosciences*, *323*, 108306.

Rahman, M., Okui, Y., Komuro, M., Anwer, M. A., & Numata, A. (2020). Probabilistic compressive strength of stiffened steel plates exhibiting column-like behavior: Ultimate and serviceability limit states. *Journal of Structural Engineering*, *146*(9), 04020166.

Reguero, B. G., Losada, I. J., & Méndez, F. J. (2019). A recent increase in global wave power as a consequence of oceanic warming. *Nature communications*, *10*(1), 1-14.

Rice, J. R. (1968). A path independent integral and the approximate analysis of strain concentration by notches and cracks. *Journal of Applied Mechanics*, *35*, 379-386.

Ritchie, R. (1983). Why ductile fracture mechanics?. *Journal of Engineering Materials and Technology, Transactions of the ASME, 105*(1), 1-7.

Rodrigue, J.-P., Comtois, C., & Slack, B. (2016). *The geography of transport systems*. London, UK: Routledge.

Saltelli, A., Annoni, P., Azzini, I., Campolongo, F., Ratto, M., & Tarantola, S. (2010). Variance based sensitivity analysis of model output. Design and estimate or for the total sensitivity index. *Computer physics communications, 181*(2), 259-270.

Sankararaman, S., Ling, Y., & Mahadevan, S. (2011). Uncertainty quantification and model validation of fatigue crack growth prediction. *Engineering Fracture Mechanics*, *78*(7), 1487-1504.

Sarzosa, D. F., Savioli, R., Ruggieri, C., Jivkov, A., & Beswick, J. (2018). A local approach to assess effects of specimen geometry on cleavage fracture toughness in reactor pressure vessel steels. In *Pressure Vessels and Piping Conference*, Prague, Czech Republic.

Shahani, A. R., Shakeri, I., & Rans, C. D. (2020). Two engineering models for predicting the retardation of fatigue crack growth caused by mixed mode overload. *International Journal of Fatigue*, *132*, 105378.

Shakeri, I., Shahani, A. R., & Rans, C. D. (2021). Fatigue crack growth of butt welded joints subjected to mixed mode loading and overloading. *Engineering Fracture Mechanics*, *241*, 107376.

Shi, H., Cao, X., Li, Q., Li, D., Sun, J., You, Z., & Sun, Q. (2021). Evaluating the accuracy of ERA5 wave reanalysis in the water around China. *Journal of Ocean University of China*, *20*(1), 1-9.

Shi, Y. J., Wang, L., Wang, Y. Q., Ma, J. S., & Bai, R. S. (2011). Proposed design method of combined connections with bolts and longitudinal welds. *Applied Mechanics and Materials*, *94*, 923-928.

Shittu, A. A., Kolios, A., & Mehmanparast, A. (2020). A systematic review of structural reliability methods for deformation and fatigue analysis of offshore jacket structures. *Metals*, *11*(1), 50.

Sikora, J. P. (1998). Cumulative lifetime loadings for naval ships. In *Proceedings from the* 1998 International Mechanical Engineering Congress & Exposition, Anaheim, CA, USA.

Sikora, J. P. (1998). *Cumulative lifetime loadings for naval ships*. Anaheim, CA, USA: American Society of Mechanical Engineers, International Mechanical Engineering Congress and Exposition.

Simulia. (2018). *ABAQUS 6.14: ABAQUS/CAE user's guide*. RI, USA: Dassault Systèmes Simulia Corp.

Sobol, I. M. (2001). Global sensitivity indices for nonlinear mathematical models and their Monte Carlo estimates. *Mathematics and Computers in Simulation, 55*(1-3), 271-280.

Sobol, I., & Levitan, Y. L. (1999). A pseudo-random number generator for personal computers. *Computers and Mathematics with Applications, 37*(4-5), 33-40.

Soliman, M., Frangopol, D. M., & Mondoro, A. (2016). A probabilistic approach for optimizing inspection, monitoring, and maintenance actions against fatigue of critical ship details. *Structural Safety, 60*, 91-101.

Soliman, M., Russell, B., Waite, C., Shen, L., & Stringer., E. (2021). *Understanding the behavior of steel connections with bolts and welds in combination*. Chicago, IL, USA: American Institute of Steel Construction (AISC).

Solomon, S., Manning, M., Marquis, M., & Qin, D. (2007). *Climate change 2007-the physical science basis: Working group I contribution to the fourth assessment report of the IPCC* (Vol. 4). NY, USA: Cambridge university press.

Somodi, B., Kövesdi, B., & Hornyák, T. (2021). Partial factor for local buckling of welded box sections. *Structures, (30),* 440-454.

Stenseng, A. (1996). Cracks and structural redundancy. *Marine Technology and SNAME News, 33*(4), 290-298.

Stocker, T. (2014). *Climate change 2013: the physical science basis: Working Group I contribution to the Fifth assessment report of the Intergovernmental Panel on Climate Change*. NY, USA: Cambridge university press.

Stopa, J. E., & Cheung, K. F. (2014). Intercomparison of wind and wave data from the ECMWF Reanalysis Interim and the NCEP Climate Forecast System Reanalysis. *Ocean Modelling, 75*, 65-83.

Stott, P. (2016). How climate change affects extreme weather events. *Science, 352*(6293), 1517-1518.

Sudret, B. (2008). Global sensitivity analysis using polynomial chaos expansions. *Reliability Engineering and System Safety, 93*(7), 964-979.

Tada, H., Paris, P., & Irwin, G. (2000). The analysis of cracks handbook. *ASME Press, 2*, 1.

Taheri, F., Trask, D., & Pegg, N. (2003). Experimental and analytical investigation of fatigue characteristics of 350WT steel under constant and variable amplitude loadings. *Marine Structures*, *16*(1), 69-91.

Tamimi, M. F., Khandel, O., & Soliman, M. (2022). A framework for quantifying fatigue deterioration of ship structures under changing climate conditions. *Ships and Offshore Structures*, 1-16.

Taylor, K. E., Stouffer, R. J., & Meehl, G. A. (2012). An overview of CMIP5 and the experiment design. *Bulletin of the American meteorological Society*, *93*(4), 485-498.

Tharian, M. G., & CG, N. (2013). Hat stiffened plates for shipbuilding. *International Journal of Applied Engineering*, *3*(1), 1-10.

Tomita, Y., Hashimoto, K., Osawa, N., Terai, K., & Wang, Y. (2004). Study on fatigue design loads for ships based on crack growth analysis. *Journal of ASTM International*, *1*(9), 1-15.

Tomita, Y., Matobat, M., & Kawabel, H. (1995). Fatigue crack growth behavior under random loading model simulating real encountered wave condition. *Marine Structures*, *8*(4), 407-422.

Tupper, E. C. (2013). *Introduction to naval architecture*. Oxford, UK: Butterworth-Heinemann.

Vanem, E., Bitner-Gregersen, E. M., & Wikle, C. K. (2013). *Bayesian hierarchical space-time models with application to significant wave height*. Høvik, Norway: Ocean Engineering and Oceanography: Springer.

Veen, D., & Gourlay, T. (2012). A combined strip theory and Smoothed Particle Hydrodynamics approach for estimating slamming loads on a ship in head seas. *Ocean Engineering*, *43*, 64-71.

Velarde, J., Kramhøft, C., & Sørensen, J. D. (2019). Global sensitivity analysis of offshore wind turbine foundation fatigue loads. *Renewable Energy*, *140*, 177-189.

Vettor, R., & Guedes Soares, C. (2015). Detection and analysis of the main routes of voluntary observing ships in the North Atlantic. *The Journal of Navigation*, *68*(2), 397-410.

Waite, C. D., Shen, L., Soliman, M., & Russell, B. W. (2022). Experimental investigation into the capacity of concentrically loaded steel connections with pretensioned high-strength bolts and longitudinal fillet welds in combination. *AISC Engineering Journal*, *59*(3), 159-180.

Wang, Z. (2000). *Hydroelectricity of high speed ships*. Kgs. Lyngby, Denmark: Technical University of Denmark,.

Wheeler, O. (1972). Spectrum loading and crack growth. *Journal of Basic Engineering, Trans. of ASCE, 94*(1), 181-186.

Willenborg, J., Engle, R., & Wood, H. (1971). *A crack growth retardation model using an effective stress concept*. OH, USA: Air Force Flight Dynamics Lab.

Williams, P. D., Cullen, M. J., Davey, M. K., & Huthnance, J. M. (2013). Mathematics applied to the climate system: Outstanding challenges and recent progress. *Philosophical Transactions. Series A, Mathematical, Physical, and Engineering Sciences, 371*(1991), 20120518-20120518.

Yuen, B., & Taheri, F. (2006). Proposed modifications to the Wheeler retardation model for multiple overloading fatigue life prediction. *International Journal of Fatigue, 28*(12), 1803-1819.

Yusuke, I., Yasuhito, T., & Fumiyoshi, M. (2017). Strength mismatch effects on Charpy absorbed energy and CTOD fracture toughness. *Japan Welding Society, 35*(2), 61-65.

Zacharioudaki, A., Pan, S., Simmonds, D., Magar, V., & Reeve, D. E. (2011). Future wave climate over the west-European shelf seas. *Ocean Dynamics, 61*(6), 807-815.

Zhang, Y. F., & Zhang, Y. L. (2021). Reliability sensitivity analysis method for mechanical components. *Mathematical Problems in Engineering*, 2021.

VITA

Mohammad Firas Tamimi

Candidate for the Degree of

Doctor of Philosophy

Dissertation: RELIABILITY AND SENSITIVITY ANALYSIS OF CIVIL AND MARINE STRUCTURES USING MACHINE-LEARNING-ASSISTED SIMULATION

Major Field: Civil Engineering

Biographical:

Education:

Completed the requirements for the Doctor of Philosophy in Civil Engineering at Oklahoma State University, Stillwater, Oklahoma in December 2022.

Completed the requirements for the Master of Science in Civil Engineering at Jordan University of Science and Technology, Irbid, Jordan in 2018.

Completed the requirements for the Bachelor of Science in Civil Engineering at Yarmouk University, Irbid, Jordan in 2016.